Ph.D. Program in Bioengineering and Robotics

Curriculum: Bionanotechnology

Thesis Title:

Design and Fabrication of Polyvinylpyrrolidone-based Intelligent Materials Suitable for Controlled Release and Wound Treatment

Student: Marco Contardi

Cycle: XXXI

Tutor: Athanassia Athanassiou

Dedication Page

"…hai visto amici andarsene prima del tempo
e sei sicuro che dall'alto ti proteggano…"

Articolo 31, *Non è un film*

To my parents and my sister, for their unconditional love.

To my friends Salvo Bonello and Luca Giacoletti, for reminding me every day that the time is not infinite, and for being my angels in this difficult route called life.

Acknowledgements

Firstly, special thanks to Dr. Athanassia Athanassiou, Dr. Ilker S. Bayer and Dr. José A. Heredia-Guerrero for proving me the opportunity to work in an international and interdisciplinary group like Smart Materials and for being the scaffold of my scientific and personal growth during these years.

I would like to thank Dr. Rosalia Bertorelli, Dr. Maria Summa, Dr. Giulia Suarato, Dr. Raffaele Spanò, Dr. Debora Russo, Dr. Ilaria Penna and Dr. Pasquale Picone for our fruitful collaborations and for their helpful support and availability.

I would like to thank Dr. Luca Goldoni for his patience, his friendship and his valuable support. Thanks to all my collaborators, especially Dr. Susana Guzman-Puyol Dr. Giovanni Perotto and Dr. Luca Ceseracciu. I cannot forget the technicians Lara Marini, Riccardo Carzino and Marco Scotto for their support and availability.

Thanks to Fiorenza Rancan and Christoph Schaudinn for giving me the possibility to have an amazing and exciting experience in their laboratories in Berlin.

Thanks to my friends Giorgio Mancini, Vincenzo Aglieri, Francesco Colaci, Francesco Asta, Alessandro Soloperto and Julien Merigeon for our unforgettable time together.

Thanks to Adalberto Camisasca and Emanuele Lago, who started this pathway with me and even if life brought us to different paths, I will never forget the time that I spent with you.

Thanks to Despoina Kossyvaki for being the sun in this cloudy city.

Finally, a great thanks to Dr. Marta Di Carlo, who was the first one to believe in me.

Table of Contents

Abstract **1**

Chapter 1 : Introduction **3**

1.1 History, synthesis, and applications of Polyvinylpyrrolidone **4**

1.2 Polyvinylpyrrolidone and drug delivery systems **6**

1.3 Evolution and design parameters for smart wound dressings **7**

1.4 Films and nanofibers dressings **10**

1.5 Wound repair: a complex mechanism with a major financial burden **11**

1.6 Design and Fabrication of PVP-based Materials as New Wound Dressings **16**

Chapter 2 : Transparent films and nanofibers mats dressings **17**

2.1 Ciprofloxacin and vinegar: a synergic recipe for antibacterial transparent films and nanofibers **18**

2.2 Materials and Methods **20**

2.2.1 Materials 20

2.2.2 Fabrication of the films 20

2.2.3 Preparation of the electrospun mats 21

2.2.4 Sample Notation 21

2.2.5 Morphological analyses 22

2.2.6 ATR FT-IR characterization 22

2.2.7 Nuclear magnetic resonance spectroscopy (NMR) 22

2.2.8 Thermal analysis 23

2.2.9 Water uptake 23

2.2.10 Mechanical properties 23

2.2.11 Drug release analyses 24

2.2.12 Antibacterial tests 24

2.2.13 In vivo full-thickness excisional skin wound healing mice model 25

2.3 Results and Discussion **26**

2.3.1 Preparation and morphological analyses of films and nanofibers 26

2.3.2 Chemical characterization 30

2.3.4 TGA and Water adsorption properties 34

2.3.5 Mechanical properties 37

2.3.6 Ciprofloxacin release studies 39
2.3.7 Antibacterial assays 42
2.3.7 In vivo full-thickness excisional skin wound healing mice model 44
2.4 Conclusions 47
Chapter 3 : Multifunctional bilayer wound dressing 49
3.1 Bilayer design as suitable strategy for multifunctional dressings 50
3.2 Materials and Methods 52
3.2.1 Materials 52
3.2.2 Methods for the bilayer preparation 53
3.2.3 Morphological Analyses 55
3.2.4 Variable-angle ATR-FTIR analysis 56
3.2.5 Adhesion and mechanical properties 57
3.2.6 Water absorption 58
3.2.7 Drug release studies 58
3.2.8 Biocompatibility assay 59
3.2.9 Hemolysis assay 60
3.2.10 ELISA tests 61
3.2.11 Antibacterial studies 61
3.2.12 In vivo full-thickness excisional skin wound healing mice model 63
3.3 Results and discussion 64
3.3.1 Morphological attributes 65
3.3.2 Chemical characterization and adhesive properties 66
3.3.3 Study of drug release of Eosin and Ciprofloxacin 71
3.3.4 In vitro biocompatibility assay on HFF-1 cells 74
3.3.5 Hemocompatibility assay 74
3.3.6 In vitro anti-inflammatory properties 75
3.3.7 Antibacterial properties of the designed bilayer 76
3.3.8 In vivo resorption, anti-inflammatory response and wound closure of bilayer 78
3.4 Conclusions 82
Chapter 4 : Testing of PVP Cipro wound dressings on an infected-wound model based on *ex-vivo* human skin 83
4.1 Biofilms and 3D infected wound human skin model 84
4.2 Material and Methods 85
4.2.1 Preparation of ciprofloxacin-loaded PVP foils and nanofiber mats 85

4.2.2 Skin samples and application of superficial wounds 86
4.2.3 Drug penetration kinetics 87
4.2.4 Toxicity of ciprofloxacin-loaded PVP foil on ex vivo skin wounds 87
4.2.5 Bacteria inoculation and characterization of the PAO1 wound infection 88
4.2.6 Antimicrobial activity of ciprofloxacin-loaded foils and nanofiber mats 89
4.3 Results and Discussion 91
4.3.1 Preparation and characterization of foils and nanofibers 91
4.3.2 Different drug penetration kinetics were measured after topical application of ciprofloxacin-loaded foils and nanofiber mats on ex vivo wounds 92
4.3.3 Ciprofloxacin-loaded foils and nanofiber mats are not toxic toward cells of the ex vivo skin model 94
4.3.4 Efficacy of ciprofloxacin-loaded foils and nanofiber mats against PAO1 infections in the 3D wound model 96
4.4 Conclusions 101
Chapter 5 : Transparent biopolymer films based on the dietary phenolic *p*-coumaric acid and PVP for controlled release 103
5.1 Discovering *p*-coumaric acid and its biological properties 104
5.2 Materials and Methods 106
5.2.1 Materials 106
5.2.2 Preparation of the films 106
5.2.3 Scanning Electron Microscopy (SEM) 108
5.2.4 X-ray diffraction 108
5.2.5 ATR-FTIR spectroscopy 108
5.2.6 NMR spectroscopy 108
5.2.7 Thermal characterization 109
5.2.8 Water absorption 109
5.2.9 Water contact angle 109
5.2.10 ABTS free radical cation scavenging assay 110
5.2.11 Mechanical tests 110
5.2.12 Drug release studies 111
5.2.13 Antibacterial tests 111
5.2.14 Full-thickness skin wound model 111
5.2.14 MMP-9 measurement by Western blot 112
5.3 Results and Discussion 113
5.3.1 Morphological characterization 113

5.3.2 Chemical and structural characterization 113
5.3.3 TGA and DSC analysis 118
5.3.4 Mechanical characterization 121
5.3.5 Water uptake, water contact angle, and antioxidant capacity 122
5.3.6 Study of drug release of PCA, MB and CA 124
5.3.7 Antibacterial assay 128
5.3.8. Mice tests 129
5.4 Conclusions 132
Chapter 6 : Conclusions 135
6.1 Contributions of this thesis 136
6.2 List of conferences, summer schools and publications 137
6.3 Recommendations for future work 139
References 141

List of Figures

Figure 1.1 Schematic representation of the advantages in the healing process of an antibacterial wound dressing 8

Figure 1.2 Schematic representation of the main phases of the wound healing process: inflammation 14

Figure 2.1 Zwitterionic structure of Ciprofloxacin 19

Figure 2.2 Crystals of Ciprofloxacin, Photograph and morphological characterization of PVP/Cipro/aceti acid films 27

Figure 2.3 A, Photograph and SEM images of nanofibers. 29

Figure 2.4 ATR-FTIR analysis of the PVP/Cipro/acetic acid materials 32

Figure 2.5 Quantification of residual content of acetic acid in the final PVP/Cipro/acetic acid materials 34

Figure 2.6 Thermal and water uptake characterization and schematic representation of the chemical interaction of PVP/Cipro/acetic acid materials. 36

Figure 2.7 Mechanical characterization of PVP/Cipro/acetic acid films. 38

Figure 2.8 Drug release results of PVP/Cipro/acetic acid films and nanofibers 41

Figure 2.9 Inhibition-zone assay against *Escherichia coli* 43

Figure 2.10 Inhibition-zone assay against *Bacillus subtilis* 43

Figure 2.11 *I In vivo* characterization of PVP/Cipro/acetic acid films and nanofibers 46

Figure 3.1 Schematic representation of the bilayer fabrication 54

Figure 3.2 Two-photon microscope, optical and SEM images of the bilayer 66

Figure 3.3 ATR-FTIR spectra of bilayer 68

Figure 3.4 Mechanical and adhesion results for the bilayer construct 70

Figure 3.5 Drug release studies and schematic representation of the mechanism of release 73

Figure 3.6 Biocompatibility of the bilayer 74

Figure 3.7 Hemocompatibility of the bilayer 75

Figure 3.8 *In vitro* anti-inflammatory characterization 76

Figure 3.9 *In vitro* evaluation of antimicrobial activity 77

Figure 3.10 *In vivo* reabsorption properties of the bilayer. 79

Figure 3.11 *In vivo* anti-inflammatory response of the bilayer. 80

Figure 3.12 Photographs and results of wound closure experiment 81

Figure 4.1 Schematic representation of the human skin *ex-vivo* infected wound model. 90
Figure 4.2 Schematic representation of the films and nanofibers fabrication. 91
Figure 4.3 Penetration of Ciprofloxacin into wound after topical application of PVP/Cipro/acetic acid films and nanofibers 93
Figure 4.4 Toxicity of PVP/Cipro/acetic acid films towards skin tissue 95
Figure 4.5 Wound infection model with *Pseudomonas aeruginosa* 98
Figure 4.6 Antimicrobial efficacy of PVP/Cipro/acetic acid films on an infected wound model. 100
Figure 5.1 Photographs and SEM images of PVP/PCA samples. 114
Figure 5.2 XRD and ATR-FTIR spectra of PVP/PCA samples 116
Figure 5.3 ^{1}H NMR spectra of PVP/PCA films 117
Figure 5.4 ^{1}H NMR and 1D-CPMG of the PVP/PCA 10:1 sample 118
Figure 5.5 TGA and DSC analysis of PVP/PCA films 120
Figure 5.6 Mechanical properties of PVP/PCA films 122
Figure 5.7 Water uptake, water contact angle and antioxidant properties of PVP/PCA films 124
Figure 5.8 Drug release of PCA, MB and CA from PVP/PCA samples 126
Figure 5.9 Kinetics data of the release of PCA 127
Figure 5.10 Antibacterial properties of PVP/PCA films 128
Figure 5.11 Photographs and graphs of reabsorption properties of PVP/PCA films 131
Figure 5.12 Evaluation of the level of MMP-9 after the application of PVP/PCA films in a wound mice model 132

List of Tables

Table 2.1 Diameter distributions of fibers in electrospun mats as a function of acetic acid concentration. 30

Table 2.2 Mechanical properties (Young's modulus, tensile stress at maximum load and elongation at break) of films. Data are expressed as mean ± s.d. (n ≥ 5). 39

Table 3.1 Composition of the fabricated samples. All the reported values represent percentages of material weight in the solution volume (w/v), while for the acetic acid (AcOH) the value designates a volume ratio (v/v). 55

Table 3.2 Calculated effective angles and analyzed depths for the different set angles used. 57

Table 3.3 Film characterization for *in vitro* studies. 59

Table 5.1 Sample labeling, molar ratio between PVP and PCA, molar fraction of PCA, weight percentage of both components, and concentration of drugs used. 107

Table 5.2 Results of antibacterial assays for the PVP/PCA 1:0, 10:1, 5:1, 2:1 samples expressed as radius of bacteria-free zone 129

Abstract

Polyvinylpyrrolidone (PVP) is probably one of the most utilized pharmaceutical polymers with applications ranging from blood plasma substitute to nanoparticle drug delivery since its synthesis in 1938. It is a highly biocompatible, non-toxic and transparent film-forming polymer. Although high solubility of PVP in an aqueous environment is advantageous, it still poses several problems for some applications in which sustained targeting and release are needed, or hydrophobic drug inclusion and delivery systems are to be designed. For this reason, in the field of controlled drug release, it is often used as an additive and not as a protagonist. On the other hand, in case of wound treatment, PVP can be a suitable biopolymer for the design of wound dressings due to its capacity to inhibit the crystallinity of several drugs, opening to their topical application, and its adhesive properties to the skin.

Therefore, the main goal of this Ph.D. was to demonstrate that this underestimated synthetic polymer can be a proper based material for the design, the fabrication and the formulation of new smart wound dressings for the delivery of antibiotic and antioxidant compounds.

In the first part of this Ph.D. study, PVP and acetic acid (AcOH) were used to inhibit the crystallization of the antibiotic Ciprofloxacin (Cipro) and to prepare transparent PVP foils as well as nanofiber mats. The presence of the antibiotic and the acid inside of the PVP matrix caused a plasticizer effect of these ingredients in the final mechanical properties of the films. Both films and nanofibers were able to release the Cipro, and an antibacterial synergism between acetic acid and the antibiotic were highlighted *in vitro* antibacterial assay. The PVP/Cipro/AcOH materials showed biocompatibility and a different rate of resorption in an *in vivo* wound mice model. In the second part of the Ph.D., a multifunctional polyvinylpyrrolidone/hyaluronic acid-based bilayer construct for sequential delivery of cutaneous antiseptic and antibiotic was designed and fabricated by using two scalable methodologies.

The bilayer material showed strong adhesion to skin, effective antibacterial activity against three strains, biocompatibility, hemocompatibility, anti-inflammatory properties both *in vitro* and *in vivo*, resorption by the skin and accelerate the wound closure in mice model. Then, the PVP/Cipro/AcOH films and nanofibers were further characterized on an infected wound model based on ex-vivo human skin. The materials resulted non-toxic and with suitable profiles of the release of Cipro inside of the skin. Moreover, they highlighted a strong antibacterial activity against biofilms infection of *Pseudomonas aeruginosa* and, especially, in case of the films they were able to eradicate completely the biofilms from the skin.

Finally, PVP was combined with the dietary phenolic compounds, *p*-coumaric acid (PCA). The introduction of the PCA in transparent films led to an increase of the hydrophobicity of the PVP-based matrix. Indeed, changes in water contact angles, water uptake and the rate of dissolution in water were found. Furthermore, the new biocomposites were investigated as drug delivery system of two model drugs and their antioxidant and anti-inflammatory activity were analyzed *in vitro* and *in vivo*, respectively.

In conclusions, several PVP-based wound dressings were designed and fabricated, demonstrating their potential efficacy for the treatment of infected wounds, burns, and chronic wounds.

Chapter 1 : Introduction

1.1 History, synthesis, and applications of Polyvinylpyrrolidone

Poly(vinylpyrrolidone) (PVP), also known as polyvidone or povidone, was synthesized for the first time in 1938 by the chemist Walter Reppe. The first step of the fabrication of the PVP was to synthesize its monomer N-vinylpyrrolidone starting from the main component acetylene and formaldehyde in the presence of ammonia. Then, the monomer was polymerized via radical reaction using hydrogen peroxide as catalyst [1].

Nowadays, this synthetic polymer is employed in numerous medical and nonmedical fields such as pharmaceutical industry and medicine [2-4], optical and electrical applications [5-7], membranes [8], adhesives [9], ceramics [10], paper [11], coatings and inks [12], lithography and photography [13], fibers and textiles [14, 15], and environmental applications [16, 17]. By the way, pharmaceutical and biomedical are the first and probably the most recognized fields of application of PVP due to its excellent biocompatibility, the capability to form stable association compounds and complexes with many active compounds, chemical stability, solubility in water and many organic solvents as well as low cost and accessibility [18].

Historically, PVP was the first polymer used during World War II as a blood plasma substitute and expander for trauma victims [3, 19]. In the present, it is mostly used as a binder in the table manufacturing for oral administration due to its high solubility in an aqueous environment. Binder has the role in holding all ingredients together till the tablet reaches the stomach and then it quickly dissolves to release the drug [2]. Moreover, several studies demonstrated how oral administration of PVP is completely safe for the body due to its particles sizes 1-100 nm that can dissolve rapidly and completely through the kidney [18]. Furthermore, PVP at the low molecular weight is considered safe also if administrated by intraperitoneal, intramuscular, and intravenous routes [20]. The synthetic polymer has also been proved to be non- irritating for eyes or skin, for this reason, it is also broadly applied for the fabrication of contact lens and cosmetic products [21-23].

In the formulation field, PVP has been appreciated for its capacity to enhance the solubility and the dispersion of low soluble hydrophobic drugs in water such as ketoconazole, flunarizine, and curcumin [24-26]. Moreover, as Mora-Huertas *et al.* reported in their review, PVP can be used as additive and stabilizer for emulsions and nanocapsules [27].

Due to its chemical structure, PVP can establish interactions of different nature and form stable complexes with several small molecules as well as with many polymers [28, 29]. For instance, in 1995 H.A. Shelanski and M. V. Shelanski, two researchers of the Industrial Toxicology Laboratories in Philadelphia discovered the most famous complex of PVP that is the topical disinfectant povidone-iodine (PVP-I) [30]. This product is currently on the market with the name of Betadine, Pyodine or Wokadine and has been demonstrated efficacy against several common infective skin bacterial strains such as *Staphylococcus aureus*, *Escherichia coli* and *Pseudomonas aeruginosa* [31]. PVPI can further be processed as beads [32], incorporated in alginate-based films [33], or combined with gelatin to form bilayer cryogels [34].

Numerous drugs present a high level of crystallinity, and this can negatively affect their administration, delivery, and absorption [35]. Jain and Banga [36] studied various additives to inhibit crystallization of two model drugs, and PVP was found to be the most effective allowing the incorporation of both drugs in amounts higher than their respective saturation solubility in transdermal drug delivery systems. Furthermore, Taylor and Zografi [37] imputed PVP capacity to break the crystallinity of indomethacin due to its amide group that can establish strong H-bonds with the carboxylic group of the drug.

PVP can also form dried films that result fully transparent but highly fragile and rigid and, for this reason, required the addition of a plasticizer [38, 39]. Finally, it is also used in the field of the electrospinning as enhancer agent of the process due to its capacity to adjust the viscosity and the surface tension of the solution [40].

1.2 Polyvinylpyrrolidone and drug delivery systems

In these years, research moved toward the fabrication of effective devices for delivering and controlling the release of drugs. For instance, several scaffolds, implants, stents, nanoparticles, nanocapsules, tablets, nanofibers, hydrogels, and films were designed and functionalized to resist inside of the body for many years and ensuring a slower and controlled release of the loaded-drug [41]. Among this jungle of systems, PVP often played the role of simple additive, dispersive or stabilizer, due mainly to its high solubility in water and, consequentially, fast dissolution in the internal body fluids [2, 3]. Pure PVP-based systems are rare and often underestimated in literature.

Therefore, to obtain the role of the main character in the great theater of the delivery and control of drugs release, and to overcome the drawback of the fast solubilization in water, PVP has been crosslinked or copolymerized with other macromolecules. The crosslinking of the pure polymer can be achieved by radical or thermal reaction leading to the formation of strong hydrogels [42-45]. In addition, PVP has been introduced in different copolymer chains reacting with various synthetic and natural polymers such as polyvinyl alcohol, polycaprolactone, silk, *k*-carrageenan, and chitosan [46-53].

Although systems that are able to remain insoluble in the human body for a long time are often a desirable feature in order to obtain a slow release of drug and avoid the peak of the drug in the blood, in some biomedical applications, instead, a burst release can be the best choice.

For instance, the new formulation Okitask® is composed of granules, and it was designed for the treatment of an occasional headache to have an immediate release and absorption of anti-inflammatory by sublingual route. Thus, the anti-inflammatory drug can reach faster the brain and minimizing the collateral effect of these drugs into the gastrointestinal tract [54].

Instead, in the case of wounds or burns, the delivery times are more complicated. Indeed, if the system is not easily resorbed by the skin, it can hinder the repair process and create intense discomfort in the

patient but, at the same time, the polymeric system should be able to swell and release a high quantity of drug *in situ*, especially in case of bacterial/biofilms infection [55, 56]. Therefore, a suitable drug delivery system for wound treatment should have a timescale of its life in the wound bed of some days. As described before, PVP showed high biocompatibility, miscibility with several solvents, polymers, and drugs as well as the possibility of forming transparent films and electrospun nanofibers. Its high sensitivity to interact with small molecules through H-bonds or complexation could be used to regulate the degradation rate in an aqueous medium. In addition, several drugs present a high level of crystallinity preventing their topical application and forcing an oral administration. Consequently, PVP could help to deliver drugs directly into the wounds due to its capacity to inhibit the crystallization of drugs. Finally, PVP has also been used as an adhesive agent to different surface including the skin[57]. Therefore, PVP looks like an underestimated but suitable candidate for the fabrication of new wound dressing materials.

1.3 Evolution and design parameters for smart wound dressings

Wound dressings have been evolving steadily in close conjunction with recent trends and advances in bio-based polymer synthesis, and processing micro/nanotechnologies [58, 59]. Dressings grew from materials or tapes that simply covered and concealed the wound, to materials that can interact with wounds so that important wound healing factors such as moisture management, active ingredient delivery and interaction with cells or proteins can be tuned or enhanced *in situ*. For chronic non-healing wounds or burns, for instance, one of the most important aspects is to prevent infection, as discussed above. As such, dressings should act as a shield protecting the wound area and, at the same time, provide a continuous or sustained release of an antiseptic agent at the wound surface to ensure a long-lasting antimicrobial action in combination with the maintenance of a physiologically moist environment for healing (Figure 1.1) [60, 61]. Moreover, in case of bacterial infections, the application

of antimicrobial wound dressing is a suitable strategy to avoid massive and prolonged oral administration of antibiotic that can create collateral effects on the patients and resistance by the bacteria.

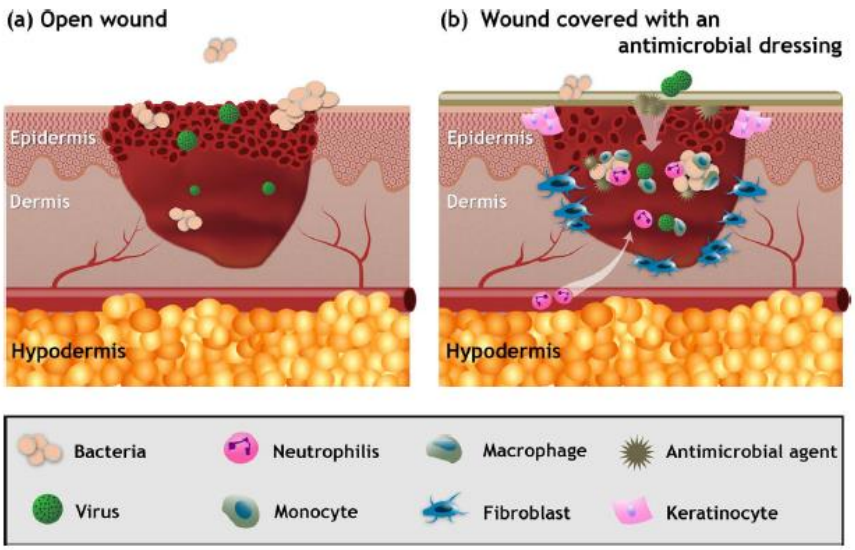

Figure 1.1 Schematic representation of the advantages in the healing process of an antibacterial wound dressing is applied to the top of a wound. (Figure adapted from *Simões et al. 2018* [61]).

Regardless of the choice of the adequate strategy to treat an injured skin is also affected by several wound features, such as type (acute, chronical, burn, excision), depth (superficial, full-thickness), the quantity of exudate, color, shape, and location within the body [62, 63]. Likewise, the selection of the right formulation regarding polymers and bioactive agents as well as the solvent of production can affect the final quality and cost of the wound dressing.

Considering the different strategies nowadays proposed, wound dressing devices can be divided into traditional, modern, bioactive, and skin substitutes [62]. Among the traditional dressings, soaked gauzes [64, 65], bandages or cotton wool [66] can be counted, which are relatively cost-effective and can serve as a primary treatment to cover the injured skin. However, the excessive absorption of exudate does not provide the necessary moisture onto the wound bed, ultimately crucial for the

restoration of the physiological conditions [60]. Hydrogels, films, nanofibers, and foams based on synthetic polymers, such as polyvinyl alcohol, polyethylene glycol, and PVP, are categorized as modern dressings [49, 67-69]. Wound dressings in the form of hydrogels tend to be transparent with many advantages such as flexibility, deterioration resistance as the wound fluids are absorbed permitting clean and neat removal of the wound dressing upon healing or during replacement, among others. Researchers are continuously developing new hydrogel wound dressings in order to address a number of gel related shortcomings, such as the need for a secondary dressing, dehydration in time, securing on the wound properly, and initiation of peri-wound maceration [70]. Flexible, water vapor permeable, self-adhering and polymeric thin film wound dressings are equally popular and generally classified as interactive and bioactive dressings [71, 72] compared to traditional passive dressings like gauze and tulle products that account for the largest market segment today [73]. Nanofibers produced by means of electrospinning methods are another interesting technology for wound dressing fabrication. The main advantages of this system are associated with their 3D structure and porosity, useful to accelerate the healing process. On the other hand, the manufacture of nanofibers often requires the use of organic and toxic additives and not all polymers can be easily electrospun. Bioactive dressings are composed of naturally-derived, biocompatible and biodegradable materials, such as collagen [65, 74], hyaluronic acid [75, 76], chitosan [77, 78], silk fibroin [79, 80], bovine serum albumin [81, 82], and alginate [83, 84]. As structural molecules of the extracellular matrix (ECM), collagen and hyaluronic acid can exploit active functions during the healing process [85]. Finally, artificial skin substitutes, such as Integra® [86], Biobrane® [87] and TransCyte® [88], have been accounted for their high efficacy, especially in the case of burns or chronic wounds. However, those constructs may present severe limitations, related to poor adhesion onto the wound bed, difficult removal of the artificial extracellular matrix, and lack of active agents against bacteria, which makes them prone to infections [63, 86, 87, 89, 90].

As such, an intelligent wound dressing should minimize the aforementioned negative environmental effects but also help accelerate the healing process without causing discomfort or needing frequent replacement [59].

Therefore, development of new, inexpensive and intelligent polymeric wound dressings from biodegradable polymers that can ensure effective protection and elimination of bacterial colonizing the wound, as well as sustaining the regeneration of new tissue is a relevant multidisciplinary challenge for medicine, pharmacology, microbiology, chemistry, and material science.

1.4 Films and nanofibers dressings

This challenge can be partially addressed by choice of the fabrication method of the dressing material and its properties, such as porosity, transparency, flexibility and 3D structure [91-94].

Polymeric films constitute one of the most appropriate therapeutic approaches for the topical administration of drugs. They can help in overcoming low solubility drawbacks of drugs in water, allowing delivery *in situ* of high concentration of drugs, and generating more prolonged effects [95]. The topical application minimizes the systemic adverse effects caused by drug absorption or the use of high levels of drug concentration dispersed throughout the body. Films can be prepared by various methods such as film solvent casting or evaporation, compression moldings, roll milling, and spin coating. These methods can exhibit and ensure differences in reproducibility of thickness, uniformity, and cost of the film.

Nanofibers mats are another interesting type of dressing that can ensure good-performance for wounds application. They are produced by using the electrospinning process. An ordinary electrospinning setup is composed of a polymer solution, a syringe, a power source, a collector or target, and a syringe pump. The main forces behind the generation of nanofibers are electrostatic forces [96]. Indeed, a high electrical potential is applied between the needle and the collector creating a ions migration in the

solution. First, the polymer solution remains at the tip of the needle due to surface tension. As the electrical potential increases, the hemispherical surface of the polymer solution elongates to form a conical shape, called Taylor cone, at the needle tip [97]. A further enhancement of the electrical field pushes the system towards a critical value, leading to the formation of a polymer jet when the repulsive electrostatic force overcomes the surface tension. At this point, a polymer jet is ejected from the tip of the Taylor cone, and it moves straight towards the metal collector. The jet undergoes a series of electrically driven bending instabilities, develops into a series of loops expanding and gradually thins in the air due to elongation before reaching the collector. During the jet movement, the solvent evaporates, and the charged jet is accumulated on a collector and becomes nanofibers [98].

The final material is characterized by nanometric size, high porosity, and surface area and a random 3D structure.

Electrospun nanofibers are mainly used for the design of scaffolds due to their 3D structure similar to the 3D structure of ECM in the skin. Indeed, this morphology represents a useful stimulus for the proliferation and the attachment of cells, improving the healing rate. Moreover, The final porosity and high surface-area allow also obtaining a material with good breathability, an important parameter to achieve a successful repair process [99]. Finally, electrospinning can be considered a good method for entrapping in polymeric matrices drugs, with low solubility in water solvent and tuning the release rate [100].

1.5 Wound repair: a complex mechanism with a major financial burden

Skin, our largest organ in the human body, constitutes the primary barrier against the environment and bacterial, fungal and viruses infection but also it plays a key role in the thermoregulation of the body

and can produce and secrete sebum and sweat. It is usually colonized by lactic acid bacteria (LAB), which contribute to keeping its partially acid pH [101]. On the other hand, skin can also release antibacterial compounds such as lysozyme and cationic antimicrobial peptides (CAMPs) [102, 103] useful for the self-cleaning of the organ. Skin is mainly composed of three regions called epidermis, dermis, and hypodermis, each one of them possessing specific biological and structural functions [104]. Cutaneous injuries are broadly diffused in our daily lives. They can either be in the form of simple scratches, cuts, and sunburns, or as large or deep wounds caused by various accidents as well as surgical interventions or radiation. In the case of skin lesion, every its single region can undergo damage and can partially or totally lose its functionalities, depending on the severity of the injury [105]. Consequently, after injuries, the body initiates a process of wound healing, which is a dynamic and complex cascade of highly integrated and overlapping events, such as hemostasis (0 h after the injury), inflammation (1-3 days), proliferation (4-21 days), and remodeling (21 days – 1 year) [106, 107].

Immediately after skin damage, components of the coagulation cascade, inflammatory pathways, and immune system are activated to prevent excessive fluid and blood losses and to clean the wound bed from the dead and devitalized tissues and bacteria [104]. Hemostasis is characterized by the formation of a platelet plug and then of a fibrin matrix, which has the role of scaffold for infiltrating cells [108]. Neutrophils appear first in the wound area due to their high concentration in the blood circulation and response to the activation of complement, the degranulation of platelets and the products of bacterial degradation [105, 109] (Figure 1.2A). Neutrophils have three main tasks: generates free radicals to kill bacteria; releases proteases, such as matrix metalloproteinase (MMP)-2 and -9 and serine proteases, to digest the collagen; phagocytize bacteria and matrix debris [110, 111]. Monocytes arrive after 2–3 day, and undergo differentiation into macrophages. Macrophages can produce and secrete some growth factors, such as interleukin 1 (IL-1) and transforming growth factors alfa and beta (TGF-α and TGF-β),

and can play a crucial role for coordinating later events in response to injury [112]. On the other hand, it has been reported in different studies that an excess of the immune response is not always a benefit for the repair, and even that healing can be faster with less inflammatory cells, especially if the bacterial infection is prevented [113, 114]. Moreover, it has been also demonstrated that the repair process can still occur also in case of absence of neutrophils and macrophages [113, 115].

The proliferation phase of wound repair occurs 4–21 days after injury and is characterized by cellular proliferation and migration of different cell types. The first event is the migration of keratinocytes over the injured dermis. They can proliferate, mature and restore the barrier function of the epithelium (Figure 1.2B). At the same time, the formation of new blood vessels, called angiogenesis, is triggered and regulated by different mediators such as the vascular endothelial growth factor A (VEGFA) and the fibroblast growth factor 2 (FGF2; also known as bFGF) [116, 117]. In the later part of this phase, fibroblasts appear and stimulated by macrophages, can differentiate into myofibroblasts. Myofibroblasts are contractile cells with the function to bring the edges of a wound together. Then, these two types of cell are involved together in the production of the extracellular matrix (ECM). This latter is mainly composed of collagen and forms the final bulk of the mature scar [118]. The remodeling phase of wound repair begins 2–3 weeks after injury and lasts for a year or more. During this stage, all of the processes activated after injury wind down and ceased. For instance, the endothelial cells, macrophages, and myofibroblasts undergo apoptosis or exit from the wound, leaving a mass that contains few cells and consists mostly of collagen and other extracellular-matrix proteins (Figure 1.2C). During this long period the collagen is remodeled but, anyway, the tissue never regains the same functionality of uninjured skin [119, 120].

The skin healing ability can be deeply altered under the presence of certain conditions, such as infections, hypoxia, poor blood supply, medications, diabetes mellitus, and vast skin loss [121, 122]. In addition, healing remains a gradual process, that extends for several days before new tissue formation

is completed (21 days). In case of burns and chronic wounds, this time can be prolonged, increasing, even more, the possibility of bacterial infections. Indeed, during this period, the total absence of skin coverage and exudate production represent a perfect medium for bacterial growth, leading to a high risk of infections for the patients [123].

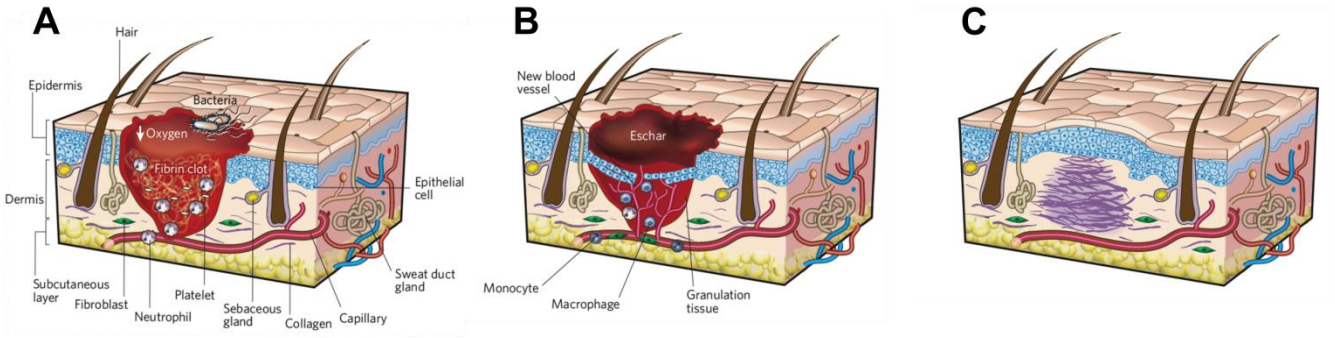

Figure 1.2 Schematic representation of the main phases of the wound healing process: inflammation (**A**), proliferation (**B**), remodeling (**C**). (Figure adapted from *Gurtner et al. 2008* [107]).

Chronic wounds formation are rare in healthy individuals. Instead, they are generally associated with underlying pathological alteration, for instance, diabetes and obesity that lead to non-healing permanent status. In this particular condition, the repair process is not able to advance from the inflammatory to the proliferation phase. Therefore, the wound bed environment is characterized by high level of pro-inflammatory agents and destructive enzymes like MMPs, interleukins, tumor necrosis factor-α (TNF-α), and free radicals due to an abundant neutrophil infiltration [124]. Moreover, alteration of the immune response and impaired levels of growth and angiogenetic factors, such as vascular endothelial growth factor (VEGF) and platelet-derived growth factor (PDGF) contribute to holding on the wound in the non-healing status.

At the same time, bacterial infections can support and heighten the chronic process [125]. Indeed, *Staphylococcus aureus* can secrete a protein able to inhibit neutrophil and monocyte chemotaxis [126, 127]. Similarly, the Gram-negative *Pseudomonas aeruginosa* can release both extracellular protease,

which can digest the collagen and use it as a source of nutrients, and serine protease, which can degrade cytokines, leading to an alteration of the patient inflammatory response [128-130]. Furthermore, several pathogens can create huge colonies and stick together, forming biofilms, which are microbial masses surrounded by a polymeric matrix. This matrix has the function to protect the bacteria by the killing activity of antibiotics and patient effectors. Therefore, biofilms can be considered as a physical and a biochemical obstruction to wound healing [131].

Consequently, the treatment of acute and chronic wounds results still a great and required challenge for science and researchers.

Moreover, taking into account this complex scenario should not upset if the management of wound repairing can be considered an immense social and financial burden for society. Indeed, in the UK, the actual burden related to wound care management has been estimated to reach £5.3 billion only throughout two years (2012/2013). This impressive result arises from the annual cost to manage both healed (£2.1 billion) and unhealed (£3.2 billion) wounds. Moreover, as revealed by Chandan *et al.* in 2010, in the US 6.5 million patients were affected by chronic wounds with an annual cost of US$25 billion. While in the Scandinavian countries the cost associated with the wound treatment is around 2-4% of the total health care expenses.

These studies strikingly pointed out how, in order to reduce the high costs associated with wound managing, a great effort needs to be put towards the implementation of new technologies, aiming to facilitate medical procedures and increase the wound treatment success rate [132].

Science and researchers are still spending time and funding on the design and fabrication of new effective medical treatments, such as wound dressings, driven by the fact that this silent and hidden illness affects the quality of the life of over 20 million people worldwide [133].

1.6 Design and Fabrication of PVP-based Materials as New Wound Dressings

For the design and the fabrication of a wound dressing several considerations has to be taken into account, including choice of materials and solvents, their 3D structure, biodegradability, bioactivity, bio-resorption and mechanical properties as well as the cost of production. Indeed, this Ph.D. project intended to demonstrate that materials based on the synthetic polymer polyvinylpyrrolidone can be a suitable and economical choice for the production of new smart wound dressings. Furthermore, PVP allows incorporation of hydrophilic and hydrophobic molecules, and it can be easily mixed with another biopolymer, starting from eco-friendly solvents.

Therefore, the main goal of this Ph.D. thesis was to design low-cost and innovative multifunctional bioactive PVP-based materials exploiting the film and electrospun nanofibers methods for wound healing application.

Specifically, in chapter 2 of this Ph.D. study will be discussed how to formulate and fabricate fully-transparent and flexible films and nanofibers mats with antimicrobial activity based on PVP. In chapter 3 will be presented the scalable fabrication of a multifunctional bilayer construct and its bioactive features *in-vitro* and *in-vivo*. In the chapter 4 will be examined the toxicity, the drug release and diffusion into the skin and the efficacy against *Pseudomonas aeruginosa* of the films and the nanofibers on an infected-wound model based on *ex-vivo* human skin. Finally, in chapter 5 will be debated the production of a new class of bio-composites, based on PVP and a phenolic compound, and their potential application for drug delivery and chronic wounds.

Chapter 2 : Transparent films and nanofibers mats dressings

2.1 Ciprofloxacin and vinegar: a synergic recipe for antibacterial transparent films and nanofibers

Most commercially available wound dressings are frequently opaque. Visual observation of the healing process is therefore prevented. Infection or other complications cannot be easily detected with opaque coverings. During the inspection, dressing removal generally causes discomfort but also healing disruption, bleeding and granuloma formation. Therefore, transparent wound dressings would be highly appropriate. Particularly, antiseptic loaded and adhesive free transparent wound dressings that can be easily absorbed by the wound are highly desirable in the sense that instead of removal and replacement, an identical self-adhering transparent dressing can be immediately applied after the absorption of the previous one [134].

Ciprofloxacin (Cipro) is an antibiotic that belongs to the family of fluoroquinolones [135]. It is considered to be one of the most important medications for basic health care [136]. Its spectrum of activity includes most strains of bacterial pathogens responsible for respiratory, urinary tract, gastrointestinal, and abdominal infections, including gram-negative and gram-positive bacterial pathogens [135, 137, 138]. It functions by inhibiting DNA gyrase and topoisomerase IV (type II topoisomerases), necessary to separate bacterial DNA, thereby inhibiting cell division. The main drawback of monohydrochloride monohydrate-free Cipro is its insolubility in water at physiological pH levels of 7.4 [139]. This is due to its molecular structure in dry powder form [140]. As illustrated in Figure 2.1, the stable molecular structure of Cipro is a zwitterionic state, in which a positive charge on secondary amine of the piperazine ring and a negative charge on the carboxylic group are present [141, 142]. Strong intermolecular interactions between these charges cause insolubility when dispersed in water. To solubilize Cipro in water, it is necessary to reduce the pH disrupting the charge balance of the zwitterionic state [139].

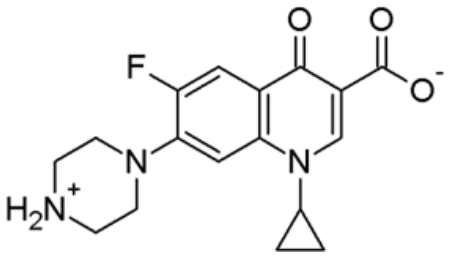

Figure 2.1 Zwitterionic structure of Ciprofloxacin.

Although frequently referred to as Cipro, the most common form of Ciprofloxacin is monohydrochloride monohydrate salt tablets (CiproHCl). Both Cipro and CiproHCl are not film-forming molecules. Upon solution casting from suitable aqueous solvents both tend to crystallize into large needle-like shapes (see Figure 2.2A) during solvent evaporation [140, 141, 143-146]. This is regarded as one of the main limitations of producing transparent polymeric films loaded with Cipro or CiproHCl suitable for biomedical applications [147, 148].

AcOH was chosen because it is a weak digestible acid (up to 20% in vinegar) and it is commonly used in the wound healing field. Usually, it is directly applied to infected burns and wounds, in the form of 1-5% (v/v) solution in water [149, 150]. Its antibacterial effect is not only due to its acidity but mostly due to its capacity to cross the bacterial membrane and change the pH of the cytoplasm [151, 152], altering the cellular proton gradients, unfolding protein and causing DNA damages [151]. Furthermore, acetic acid is capable of preventing the formation of biofilms and affecting the viability of grown ones [153] in addition to its effectiveness against various bacteria including *Escherichia coli*, *Staphylococcus aureus*, *Acinetobacter baumannii* [153]. The most significant target of acetic acid is *Pseudomonas aeruginosa* [150] bacterium that generally infects burns [154] and can become resistant against fluoroquinolones antibiotics like Cipro [155, 156]. Therefore, the combination of these two active agents can result in a good strategy against cutaneous bacterial infections.

In this chapter, a facile water-based process to incorporate monohydrochloride monohydrate-free Cipro in PVP by using aqueous acetic acid (AcOH) as co-solvent will be demonstrated. Use of acetic acid not only enabled solubilization of Cipro along with povidone in water but also prevented post-crystallization and phase separation of it in dry polymeric films after solvent (water) evaporation enabling fabrication of completely transparent antibiotic PVP films. Moreover, in order to overcome the solubility issue, same solutions were used to electrospin nanofiber (non-transparent) mats for the first time.

2.2 Materials and Methods

2.2.1 Materials

Polyvinylpyrrolidone (PVP; MW = 360,000), monohydrochloride monohydrate free ciprofloxacin (≥98.0% HPLC; MW = 331.34), acetic acid (≥ 99.7%) were purchased from Sigma-Aldrich and used as received. Dimethylsulphone (DMS), heavy water (D_2O) and 3-(trimethylsilyl)propionic-2,2,3,3-d4 acid sodium salt (TSP) were obtained from Sigma Aldrich (Milan, Italy). Deionized water was obtained from Milli-Q Advantage A10 ultrapure water purification system. Phosphate buffered saline (PBS) solution (pH 7.4) was acquired from Sigma-Aldrich and used as received.

2.2.2 Fabrication of the films

Cipro/polymer solutions were prepared by dissolving Cipro powder and PVP in various water/acetic acid solutions containing 1, 5, 10 and 30% (v/v) AcOH in 10 mL of total volume. Cipro concentration in the solutions was maintained at 0.1% w/v while PVP concentration was 3% (w/v). Initially, Cipro powder was dispersed in vials containing water/AcOH solvents, and upon complete dissolution of Cipro, PVP polymer was added and dissolved under mild stirring. A control solution of PVP in water at 3% (w/v) was also prepared. The solutions were cast on circular plastic Petri-dishes (50×50 mm) and

dried for 3 days under an aspirated hood under ambient conditions (16 – 20°C and 40 – 50% R.H). Then, the films were placed in a vacuum desiccator for 3 more days for complete removal of excess acetic acid. Dry transparent films had a thickness of 130 –170 µm.

2.2.3 Preparation of the electrospun mats

For the fabrication of the electrospun mats, identical acetic acid solutions were prepared as above. A more concentrated PVP polymer solution was necessary to enable electrospinning. The optimum concentration of PVP was found to be 25% (w/v). Cipro powder was dispersed in these solutions a priori such that the final blend contained 0.4% Cipro with respect to PVP polymer by weight. Mats were produced by means of a vertical electrospinning setup. Syringes with a stainless-steel 18-gauge needle were filled with the different solutions and connected to a syringe pump (NE-1000, New Era Pump Systems, Inc.) working at a constant flow rate of 250 µL/hr. The needle was clamped to the positive electrode of a high-voltage power supply generating 30.5 kV, and an aluminum disk was used as a collector (needle-collector distance of 24 cm).

2.2.4 Sample Notation

Film and fiber mat samples were classified by using two different notations: Samples labeled as P0%, P1%, P5%, P10% and P30% represent Cipro free PVP films or mats, obtained from solutions containing acetic acid with concentrations ranging from 0% to 30% (v/v). Similarly, samples labeled as PC1%, PC5%, PC10% and PC30% represent Cipro containing PVP films or mats with identical acetic acid concentration range. For film casting, PVP concentration in solution was always maintained at 3% (w/v) and for electrospinning PVP concentration in solution was increased and always maintained at 25% (w/v). On a dry basis, Cipro concertation with respect to PVP in the films and mats was 3.3 wt.% and 0.4 wt.%, respectively.

2.2.5 Morphological analyses

Morphology of the films and the nanofibers was analyzed by Scanning Electron Microscopy (SEM), using a variable pressure JOEL JSM-649LA microscope equipped with a tungsten thermionic electron source working in high vacuum mode, with an acceleration voltage of 5 kV. The specimens were coated with a 10 nm thick film of gold using a Cressington Sputter Coater – 208 HR. The diameter of the fibers was analyzed and determined by using *ImageJ* software. Approximately 150 measurements were taken to obtain the diameter distribution of each type of fibers.

The transparency of all the films has been investigated by means of CARY 300 Scan UV-visible spectrophotometer. The absorbance values at 600 nm were followed and then divided for the thickness of each film.

2.2.6 ATR FT-IR characterization

Infrared spectra were obtained with an Attenuated Total Reflectance (ATR) accessory (MIRacle ATR, PIKE Technologies) coupled to a Fourier Transform Infrared (FTIR) spectrometer (Equinox 70 FT-IR, Bruker). All spectra were recorded in the range from 3800 to 600 cm^{-1} with a resolution of 4 cm^{-1}, accumulating 128 scans. For the subtraction of spectra, they were previously normalized to the most intense band (C=O stretching mode at 1647 cm^{-1} of PVP).

2.2.7 Nuclear magnetic resonance spectroscopy (NMR)

Residual acetic acid quantity in the transparent films and the electrospun nanofibers was determined using NMR spectroscopy. Typically ca. 70 mg of sample was dissolved in 1 ml of D_2O and transferred into 5mm tubes (Bruker). The ^1H NMR quantitative spectra (^1H *q*-NMR) were acquired on a Bruker AvanceIII 600 MHz spectrometer equipped with 5 mm QCI cryoprobe with *z* shielded pulsed-field gradient coil. Before each acquisition, the temperature was let equilibrate into the probe at 298.0K for 2 min., an automatic matching and tuning were run and the homogeneity automatically adjusted. The 90°

pulse was optimized on each sample-tube by an automatic pulse calculation routine [157]. 16 transients were accumulated, at a fixed receiver gain (4), using 128 K complex data points, over a spectral width of 20.6 ppm with an inter-pulses delay of 30 s. An exponential line-broadening (0.1 Hz) was applied to FIDs before the Fourier transformation. The spectra were manually phased and automatically baseline corrected.

2.2.8 Thermal analysis

The thermal degradation behavior of the films was investigated by a standard thermogravimetric analysis (TGA) method using a TGA Q500 from TA Instruments. Measurements were performed on 3-5 mg samples in an aluminum pan under inert N_2 atmosphere with a flow rate of 50 mL/min in a temperature range from 30 to 600°C with a heating rate of 5°C/min. The weight loss and its first derivative were recorded simultaneously as a function of time/temperature.

2.2.9 Water uptake

Water adsorption measurements were carried out as follows: dry samples were weighed (~30 mg) on a sensitive electronic balance and then they were placed in different chambers with increasing humidity. The humidity conditions were: 0%, 11%, 45%, 85% and 100%. Prior to humidity chamber tests, samples were dried in a desiccator until no change in sample weight was measured. After conditioning in different humidity chambers until equilibrium conditions, each film was weighed, and the amount of adsorbed water was calculated based on the initial dry weight as the difference.

2.2.10 Mechanical properties

The mechanical properties of the films were determined by uniaxial tension tests on a dual column universal testing machine (Instron 3365). Films were cut in prismatic specimen with a width of 4 mm and an effective length of 25 mm. Displacement was applied with the rate of 3 mm/min. From the resulting stress-strain curves, the elastic modulus, ultimate tensile strength (UTS), elongation at yield

and elongation at maximum load were extracted. Measurements were performed on 5 samples per each sample. All the stress-strain curves were recorded at 25°C and 44% relative humidity (RH).

2.2.11 Drug release analyses

The release of Cipro from the transparent films and nanofiber mats was measured by using a CARY 300 Scan UV-visible spectrophotometer. Cipro has a characteristic UV absorbance peak at 272 nm. Initially, a calibration curve was constructed by dissolving only Cipro. This was done by forming a stock solution of 10mL of water, with 10% (v/v) acetic acid and 0.1% (w/v) Cipro. The calibration curve was constructed by adding 75, 60, 50, 40, 30, 25, 20, 10, 5 and 2,5 µL of stock solutions in UV-vis cuvettes and diluting to a final volume of 3 mL. Then, the absorbance value from each cuvette was recorded. The molar extinction coefficient calculated according to the Beer-Lambert law was 37900 cm^{-1} M^{-1}. For drug release measurements, films and mats were gently placed in 2.5 mL cuvettes containing PBS solution under constant stirring (200 rpm) and the temporal increase in absorbance at 272 nm was monitored. After a few preliminary experiments, the optimum film weight was adjusted to 1 mg (containing ~ 34 µg of Cipro) and the optimum electrospun mat was 6 mg (containing ~ 34 µg of Cipro).

2.2.12 Antibacterial tests

Antibacterial properties of transparent films and nanofiber mats were tested on the Gram-negative bacterium *Escherichia coli* (Thermo-Fisher Scientific), and on the Gram-positive *Bacillus subtilis* (ATCC). *E. coli* was cultured in LB-Broth (Sigma-Aldrich) at 37°C. *B. subtilis* was cultured in Difco Nutrient Broth (Becton Dickinson) at 30°C. 2.5 µL of each overnight bacterial culture were mixed with 100 µL of the respective broth and gently spread onto LB-Agar plates (for *E. coli*, purchased from Sigma-Aldrich) or Difco Nutrient Agar plates (for *B. subtilis*, purchased from Becton Dickinson). The inhibition-zone assay was carried out by gently depositing samples of films or fibers (1 mg and 6 mg, respectively) on the center of each agar plate. The plates were incubated O/N at the appropriate

temperature required by each bacterial strain (37 °C or 30 °C) The next day the plates were photographed, and the halo of bacterial growth inhibition was calculated by ImageJ software. The measurements were stated as a percentage of the total area of the agar plate.

2.2.13 In vivo full-thickness excisional skin wound healing mice model

Male C57BL/6J mice, 8-12 weeks old (Charles River, Calco, Italy), were used for *in vivo* studies. They were maintained under a 12-hour light/dark cycle (lights on at 8:00 am) under a controlled temperature of (21 ± 1°C) and relative humidity of (55 ± 10%) conditions. All experiments were carried out in accordance with the guidelines established by the European Communities Council Directive (Directive 2010/63/EU of 22 September 2010) and approved by the National Council on Animal Care of the Italian Ministry of Health. All efforts were made to minimize animal suffering and to use the minimal number of animals required to produce reliable results. Mice were anesthetized by intra-peritoneal injection of ketamine (10%), and xylazine (5%) mixture and the dorsal skin was shaved. One full-thickness skin wound was generated in the center of the back of each animal, by a sterile 6-mm biopsy punch. A photo of the wound was taken immediately afterward the biopsy generation, and then covered with fiber-PC1%; film-PC1%, fiber-PC30% and film-PC30%. To avoid removal of the dressings by mice, all treated wounds were covered with Tegaderm^{TM} just before the animals woke, until the end of the experiment. To evaluate bio-resorption over time, the condition of each dressing has been photographed at different time intervals (30 seconds, 1, 3, 5, 10, 20, 30, 60, 120, 180, 240 minutes) after dressing application. Each acquired photograph of the dressing on the wound was analyzed by *ImageJ* software, to calculate the percentage of the bio-resorbed membrane during the time [158]. Mice were housed individually during the experiments, with water and food *ad libitum*. All animals were sacrificed at the end of the experiment by carbon dioxide euthanasia.

2.3 Results and Discussion

2.3.1 Preparation and morphological analyses of films and nanofibers

Several films were produced from water solutions containing different concentration combinations of Cipro, AcOH and PVP polymer as preliminary experiments (see Figure 2.2A). A proper concentration range among Cipro, PVP, and AcOH that can completely eliminate crystallization induced phase separation of Cipro within the PVP matrix during aqueous solvent evaporation. Outside of this concentration range, large crystal needles of Cipro in PVP films form leading to poor transparency and poor mechanical properties (Figure 2.2A). The optimum condition that produced completely transparent films with no microscopic crystal phase separation was identified as dry films containing 3.3% by weight unmodified Cipro (see Figure 2.2B) with respect to PVP. Cipro/PVP films could be cast with the minimum required amount of acetic acid concentration in water corresponding to 1vol.%. Further verification of the absence of microcrystals of the antibiotic in the films can be found in Figures 2.2C and 2.2D in which SEM image of the films and optical transparency, respectively, are presented. A slight increase of Cipro concentration in the film to 4% by weight, while keeping the acetic acid concertation at 1vol.% in water, for instance, caused massive crystallization of Cipro in PVP as seen in Figure 2.2A. By changing the concentration of acetic acid to 2 vol.% in water, it was again possible to produce transparent PVP films containing 4 wt.% Cipro. Once the minimum amount of AcOH required was determined, identical films were cast from solutions containing 5, 10 and 30 vol.% AcOH in water. Antibiotic PVP films produced from solutions containing higher AcOH concertation were found to be softer and more flexible due to residual bound AcOH in the PVP network (after drying). As will be demonstrated later on, this means that AcOH is not only useful to dissolve Cipro in water but also enables tuning of the plasticity and flexibility of the films, moreover providing antiseptic activity.

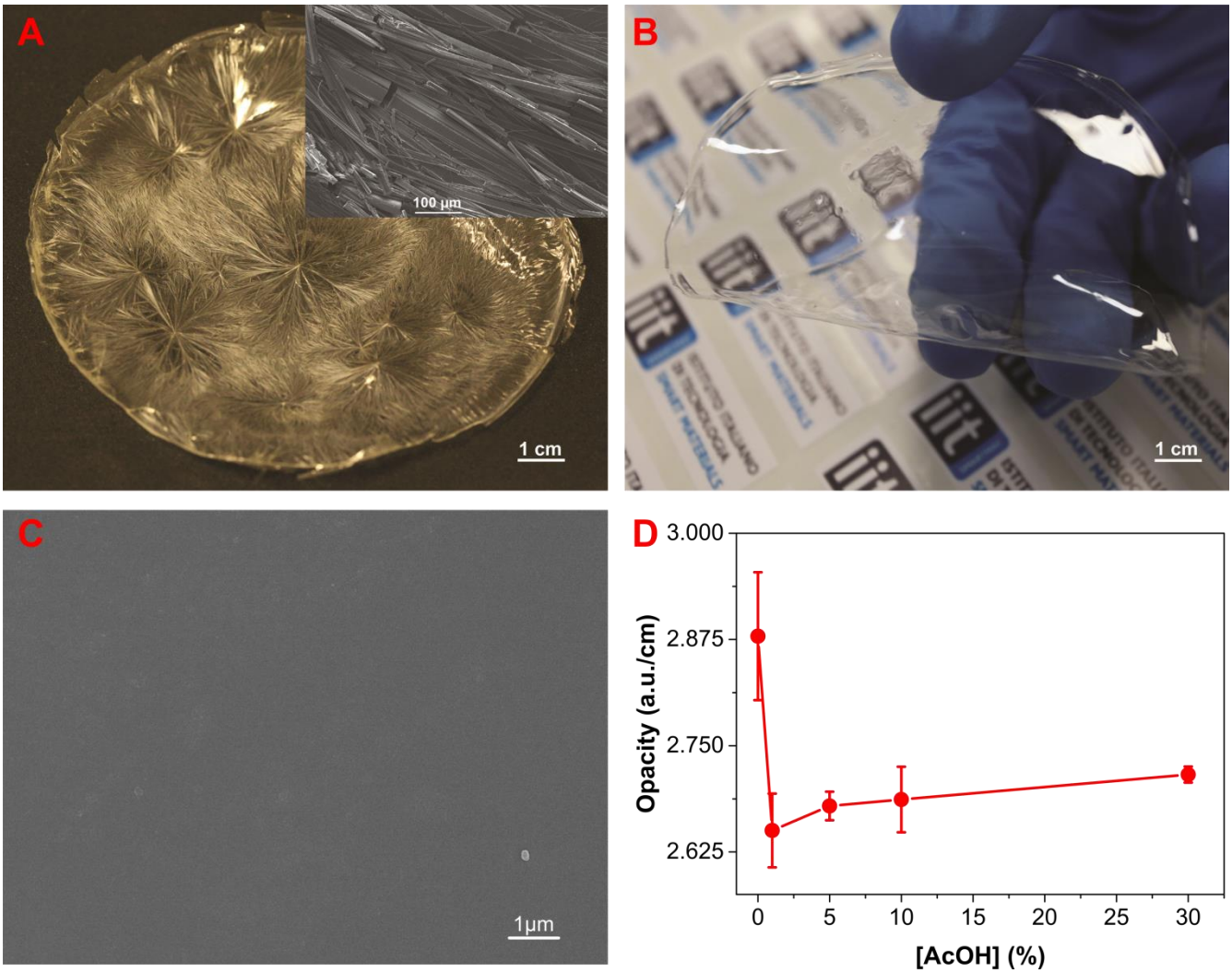

Figure 2.2 A, Crystallization/phase separation of 4 wt.% Cipro in PVP Film cast from 1 vol% acetic acid aqueous solution. **B**, Photograph of a transparent film 3.3 wt.% Cipro in PVP cast from 1 vol% acetic acid aqueous solution. **C**, SEM image of PC30% film. **D**, Opacity analysis of P0%, PC1%, PC5%, PC10%, PC30% films.

From the same solutions, it was also possible to produce antibiotic-loaded fiber mats as shown in Figure 2.3A. Microscopic morphology of the produced mats was investigated by using SEM. Detailed SEM images of all the samples studied are presented in Figures 2.3B-L. As can be seen, fibers were produced very uniformly without beads and defects. Table 2.1 summarizes the average fiber diameter

of PVP and PVP-Cipro fiber mats produced by using different concentrations of AcOH. On average, the fiber size ranged from 250 nm to 440 nm. The largest fiber diameter was obtained by electrospinning sample, P0% (pure PVP with no AcOH), where the formation of some beads was also detected. Adding only 1vol. % of acetic acid to the PVP water solution decreased the fiber diameter almost by half as seen in Table 2.1. Further increase in acetic acid concentration did not reduce the fiber diameter but rather comparatively increased it. Effect of acetic acid concentration on the fibers containing Cipro was somewhat similar, however on average, the increase in fiber diameter due to higher acetic acid concentration was limited to approximately 95 nm (from 315 to 410 nm) (from 1 vol.% to 30 vol.%) compared to 140 nm (from 250 to 390 nm) in PVP (from 1 vol.% to 30 vol.%). Nonetheless, the presence of acetic acid ensured that the fiber sizes remained well below 1 μm, which is very important in obtaining high surface to volume ratio materials with porosity [96]. All of these properties enhance the fluid absorption [159], the dissolution rate and the release properties, especially in comparison with the films cited above.

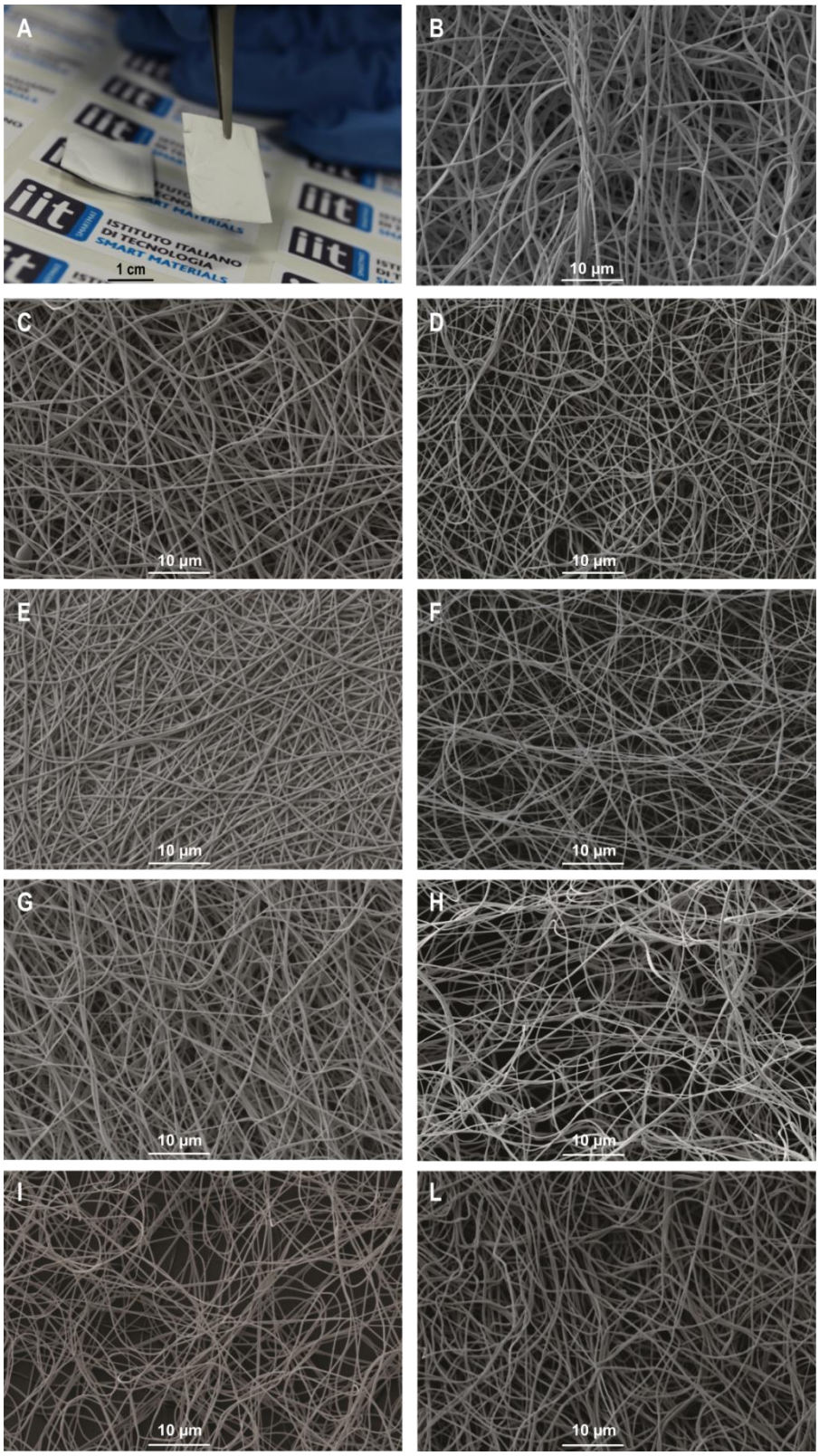

Figure 2.3 A, Photograph of PC30% nanofiber mat. **B-L**, SEM images of PC30%, P0%, P1%, P5%, P10%, P30%, PC1%, PC5%, and PC10% fibers, respectively.

Acetic Acid (vol %)	PVP (nm)	PVP + Cipro (nm)
0	440±55	n.a
1	250±30	315±30
5	270±30	330±35
10	310±30	350±30
30	90±40	410±40

Table 2.1 Diameter distributions of fibers in electrospun mats as a function of acetic acid concentration.

2.3.2 Chemical characterization

PVP and PVP-Cipro films were chemically characterized by ATR-FTIR (Figure 2.4). In Figure 2.4A the infrared spectra of P0%, P30%, and PC30% are shown. Bands associated with the chemical structure of the polyvinylpyrrolidone and water such as O-H stretching mode at 3408 cm^{-1}, asymmetric and symmetric CH_2 stretching mode at 2955 cm^{-1} and 2883 cm^{-1}, respectively, C=O stretching mode at 1647 cm^{-1}, C-N stretching mode at 1018 cm^{-1}, out-of-plane C-H bending mode at 843 cm^{-1}, and C-H rocking mode at 733 cm^{-1} were clearly observed [160]. However, some significant differences were detected in the spectral regions ascribed to C=O and O-H stretching vibrations. To better characterize these chemical differences, we subtracted the spectra of P30% and PC30% from one of the samples of PVP solved in pure water (P0%). The subtracted spectra, P30% - P0% and PC30% - P0%, together with the infrared spectra of pure ciprofloxacin and ciprofloxacin after solution in 30% acetic acid (v/v)

in water in the region between 1800 and 1500 cm^{-1}, are shown in Figure 2.4B. For the spectrum of P30% - P0% the presence of acetic acid was mainly revealed by a vibration at 1719 cm^{-1} (the stretching mode of C=O in carboxylic acids interacting by H-bonds) and, to a lesser extent, another one at 1760 cm^{-1} (the stretching mode of C=O in free carboxylic acids) [161]. These bands were also present in the spectrum of PC30% - P0% together with two additional absorptions at 1676 cm^{-1} (the stretching mode of C=O in carboxylic acids α,β-unsaturated) and 1624 cm^{-1} (the stretching mode of C=O in ketones) related to the ciprofloxacin after dissolution in 30% acetic acid (v/v) in water [162]. Interestingly, the infrared spectrum of pure ciprofloxacin was characterized by two bands at 1614 cm^{-1} (the stretching mode of C=O in ketones, note that it was shifted to lower wavenumbers) and 1587 cm^{-1} (the stretching mode of C=O in carboxylates α,β-unsaturated) [162], indicative of a zwitterionic structure. Hence, when acetic acid is added, ciprofloxacin changes its structure from zwitterion to a non-charged structure, as illustrated in the inset of Figure 2.4A. Finally, Figure 2.4C shows the subtracted spectra P30% - P0% and PC30% - P0% in the spectral region associated with the O-H stretching mode (3800-3000 cm^{-1}). In both cases, negative absorptions were observed. In PC30% - P0% this effect was higher than for P30% - P0%. This intensity loss can be related to the loss of water molecules inside the polymer matrix.

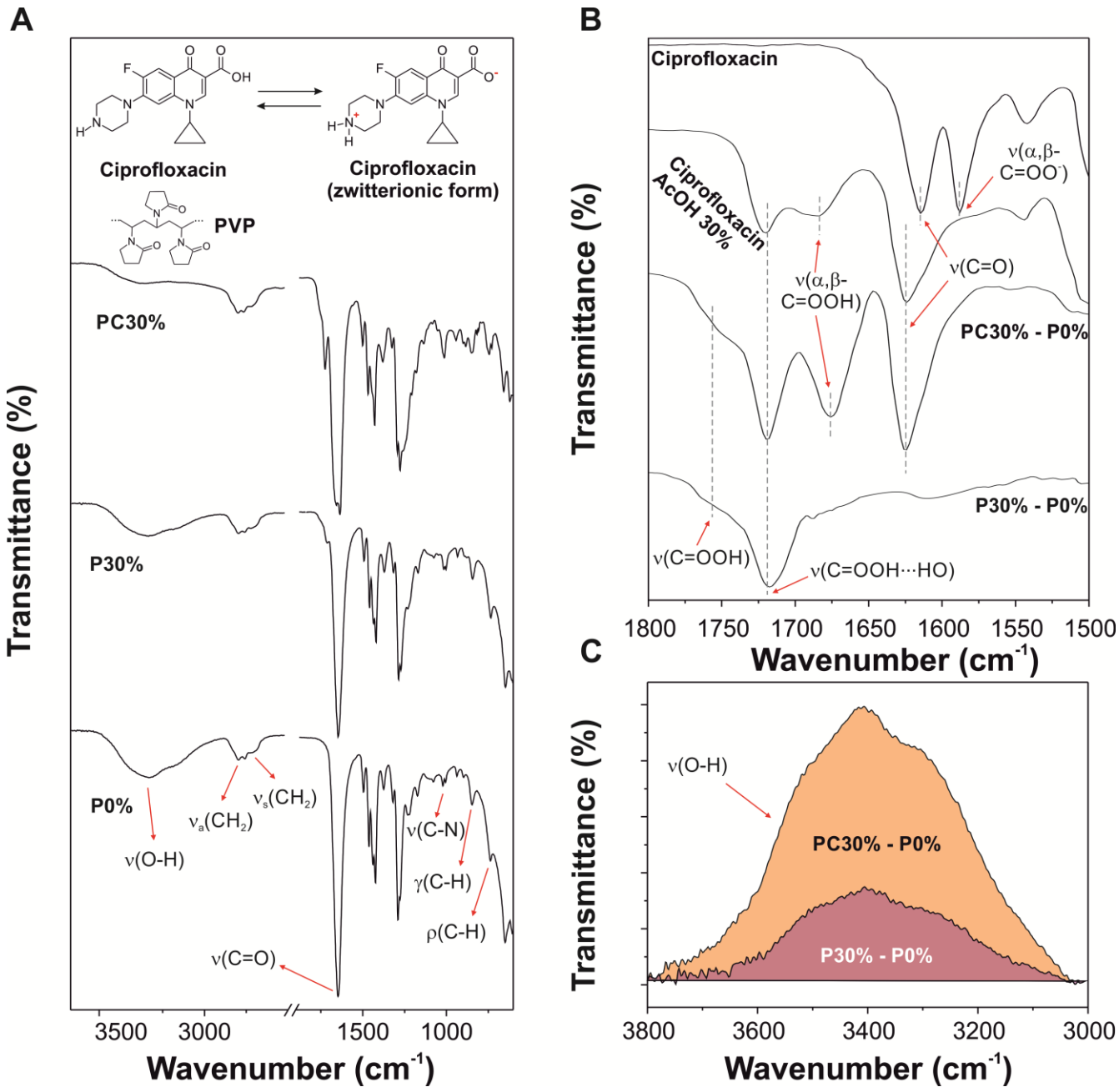

Figure 2.4 A, ATR-FTIR spectra of P0%, P30% and PC30% samples. Main assignations of PVP are shown. The chemical structures of ciprofloxacin and PVP are drawn in the top. **B**, comparison in the spectral region of the C=O stretching mode (1800-1500 cm^{-1}) of ciprofloxacin, ciprofloxacin after solution in acetic acid (30%, v:v) and the subtracted spectra PC30% - P0% and P30% - P0%. **C**, subtracted spectra PC30% - P0% and P30% - P0% in the spectral region of the O-H stretching mode (3800-3000 cm^{-1}).

2.3.3 Quantification of residual acetic acid

The acetic acid content in the samples was measured by PULCON (PUlse Length Based Concentration Determination) procedure [163], an external standard quantitative NMR method, that allows to measure the concentration of a component in a mixture, by comparing the integrated peak intensity of the signal of interest (e. g. the CH_3 singlet of acetic acid, at 2.07 ppm) and the integrated peak intensity of a reference signal. As an external reference, we used a 10 mM freshly prepared solution of dimethylsulphone (DMS) in D_2O. A deconvolution algorithm (the line fitting algorithm, MestReNova) was employed to separate the contribution of the acetic acid signal from the broad signals of the polymer [164]. The acetic acid concentration was then inferred by the ratio between the integrated intensity of the TSP signal (0.00 ppm), whose concentration was measured directly by using the PULCON method, and the integrated intensity of the acetic acid signal (at 2.07ppm). We reported the acetic acid content measured in each sample as a percentage in weight (Figure 2.5). Figure 2.5 demonstrates the amount of residual acetic acid (AcOH) in the solid materials as a function of AcOH concertation in the starting aqueous polymer solutions. Films contain much more residual acetic acid then the nanofibers. The maximum residual AcOH content in the fibers is approximately 0.1% with respect to the polymer matrix weight originating from 30% acetic acid aqueous solution. Moreover, as seen in Figure 2.5, the residual AcOH content in the fibers is much less sensitive to aqueous AcOH concentration. On the other hand, films contain approximately 1% AcOH with respect to the polymer matrix weight. Films originating from 30% acetic acid aqueous solutions contain 1.4% residual AcOH (Figure 2.5). Nonetheless, the amount of residual AcOH is not significant and remains somewhat advantageous considering two important contributions as a plasticizing effect and antiseptic functionality.

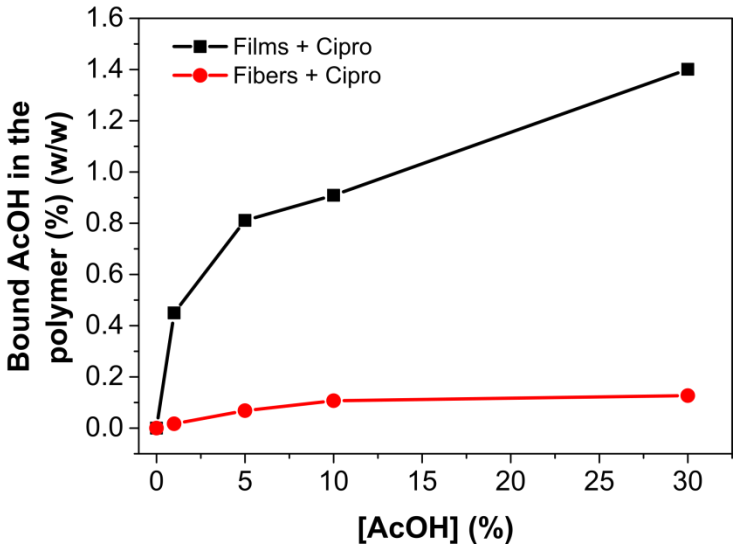

Figure 2.5 Residual content of acetic acid in the final materials as a percentage in weight.

2.3.4 TGA and Water adsorption properties

TGA and water adsorption experiments were carried out to investigate the interaction between polymeric chains and water, Cipro and acetic acid. The weight loss TGA curves of all the samples are shown in Figure 2.6A. Derivative weight loss curves for P0%, P30%, PC30% films are presented in Figure 2.6B. Three major weight loss peaks were identified in all the samples. The first step, T1, occurred below 100°C. The second step (T2) occurred at a higher temperature in the range from 200 to 300°C, and the third step (T3) was observed between 350 and 450°C. T1 can be attributed to the loss of water (environmental humidity) absorbed by the PVP matrix regardless of the acetic acid in solution. Main differences due to acetic acid in solution are registered in the weight loss corresponding to the T2 region as highlighted in Figure 2.6C. P0% films (no acetic acid) displayed a T2 peak at the highest temperature at around 260 °C. In the presence of acetic acid T2 shifted to lower temperatures. P30%, for instance, displayed a T2 peak at 244 °C. In contrast, samples with ciprofloxacin exhibited T2 peaks between 215 and 220 °C. A higher T3 peak indicated that degradation of the polymer and Cipro

occurred at the same time and also indirectly indicating no phase separation and good dispersion of the antibiotic within the polymer matrix.

Next, water uptake measurements of P0%, P30%, PC30% films are exemplified in Figure 2.6D. Interestingly, samples made with 30% v/v acetic acid in water solution were found to uptake less water under high humidity conditions. The film, P0%, had the highest water uptake under high humidity.

In view of these results, we propose the following model describing the interactions among PVP, water, acetic acid and ciprofloxacin molecules in the films (Figure 2.6E): In P0%, water molecules form H-bonds with the polar groups of PVP [165]. When acetic acid is added, it partially replaces the water molecules due to its higher affinity towards PVP chains. This could be related to the basicity of the C=O group near the nitrogen atom in the main chain of PVP [166]. When Cipro is added to the acetic acid solution, it can also substitute water molecules due to the fact that Cipro is rich in polar and acid/base functional groups and each of them are latent H-bond sites [167]. This is schematically shown in Figure 2.5E. As more and more water molecules are substituted by AcOH or Cipro, water uptake is naturally expected to be reduced. Similar results and conclusions were also obtained from nanofiber mats (not shown for brevity).

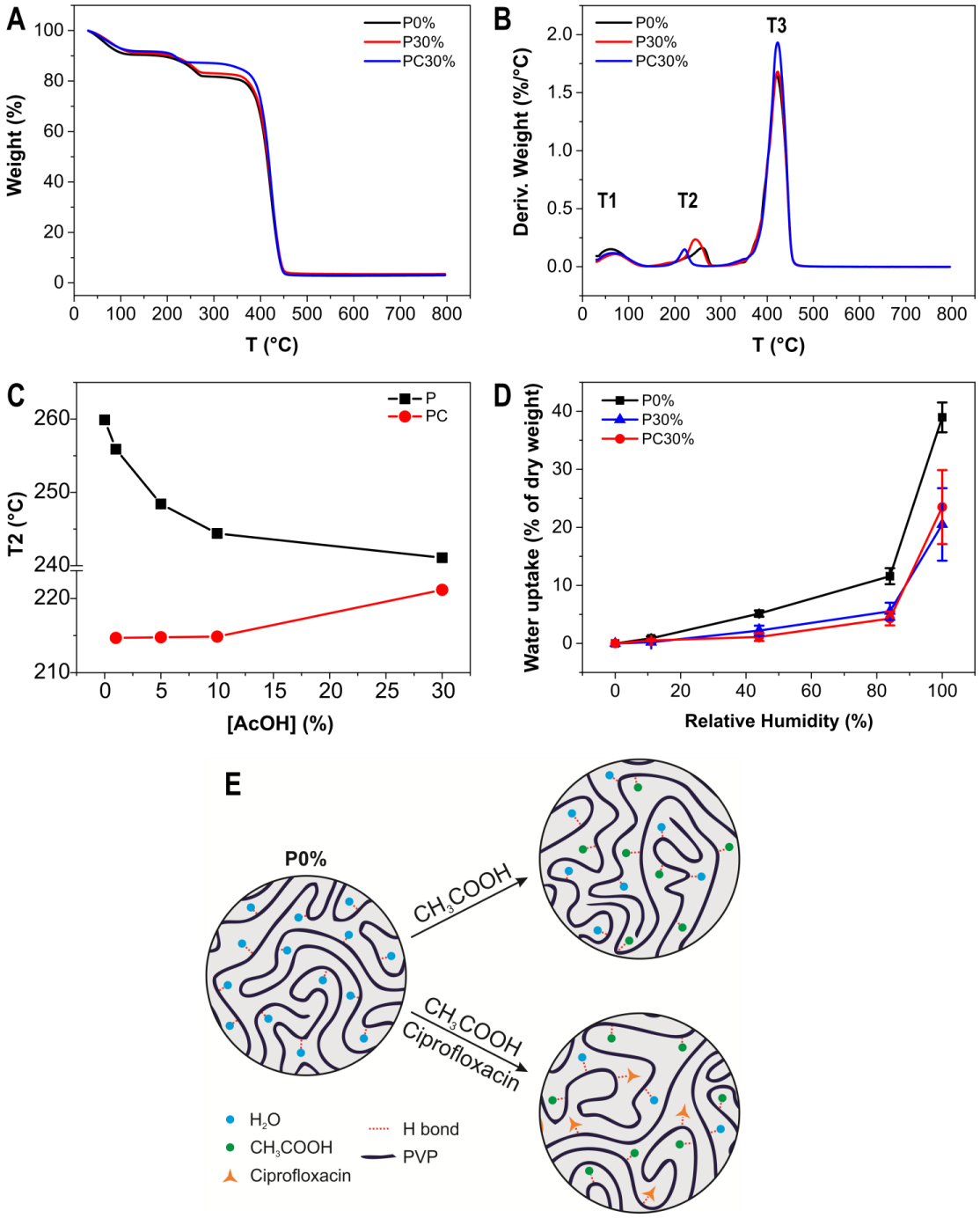

Figure 2.6 A, Thermogravimetric curve of weight loss of P0%, P30%, PC30% films **B**, Derivative of weight loss curves for pure PVP, P30% and PC30% films. **C**, The values of T2 for all films prepared are shown. **D**, Water uptake as a function of relative humidity of P0%, P30%, PC30% films. **E**, Schematic representation of the chemical interaction between PVP polymer chains and water, acetic acid and ciprofloxacin molecules.

2.3.5 Mechanical properties

PVP films cast from water solutions are highly rigid and brittle as opposed to nanofiber mats. Its mechanical properties are highly sensitive to ambient humidity. As shown in the previous section, acetic acid plasticized PVP is less prone to water uptake due to hydrogen bonding interaction between bound acetic acid and the polymer. Diffusion of single molecules in plasticized PVP polymer was shown to be more effective compared to rigid PVP, which is important for drug-loaded PVP applications [168]. Moreover, soft and flexible drug-loaded PVP films (see Figure 2.7B) are better suited for application on skin. Hence, stress-strain tests were performed to understand the effect of solution acetic acid concentration and Cipro loading on the mechanical properties of the PVP matrix. The summary of all the results is presented in Table 2.2. The stress-strain curves of P0%, P30%, PC1%, PC30% films are exemplified in Figure 2.7A. Pure PVP film cast from water solution, i.e., P0%, is a rigid plastic with an elastic modulus of about 1 GPa and cannot sustain strain rates more than 15%. Acetic acid concentration in solution drastically changed the stress-strain characteristics of both pure PVP and PVP-Cipro films. Pure PVP films, produced from 30% v/v aqueous acetic acid solution, for instance, display elastic modulus of approximately 525 MPa (see Figure 2.7B) with more than 150% elongation before the break (see Table 2.2). Ultimate tensile strength is also lowered as a function of increasing acetic acid concentration as seen in Figure 2.7C. This indicates that soft and highly stretchable films with very good transparency can be made by adjusting the acetic acid concentration in solution. Furthermore, the presence of Cipro in the films does not disrupt the acetic acid induced plasticity of the pure PVP films. The antibiotic inclusion seems to lower the elastic modulus further on average and somewhat enhances plasticization action on the films when aqueous acetic acid concentrations are above 5% v/v (see Figures 2.7B and 2.7D). For instance, elongation at break values of PVP-Cipro films produced from 30% v/v acetic acid aqueous solutions increased almost threefold (280 %) compared to pure PVP films.

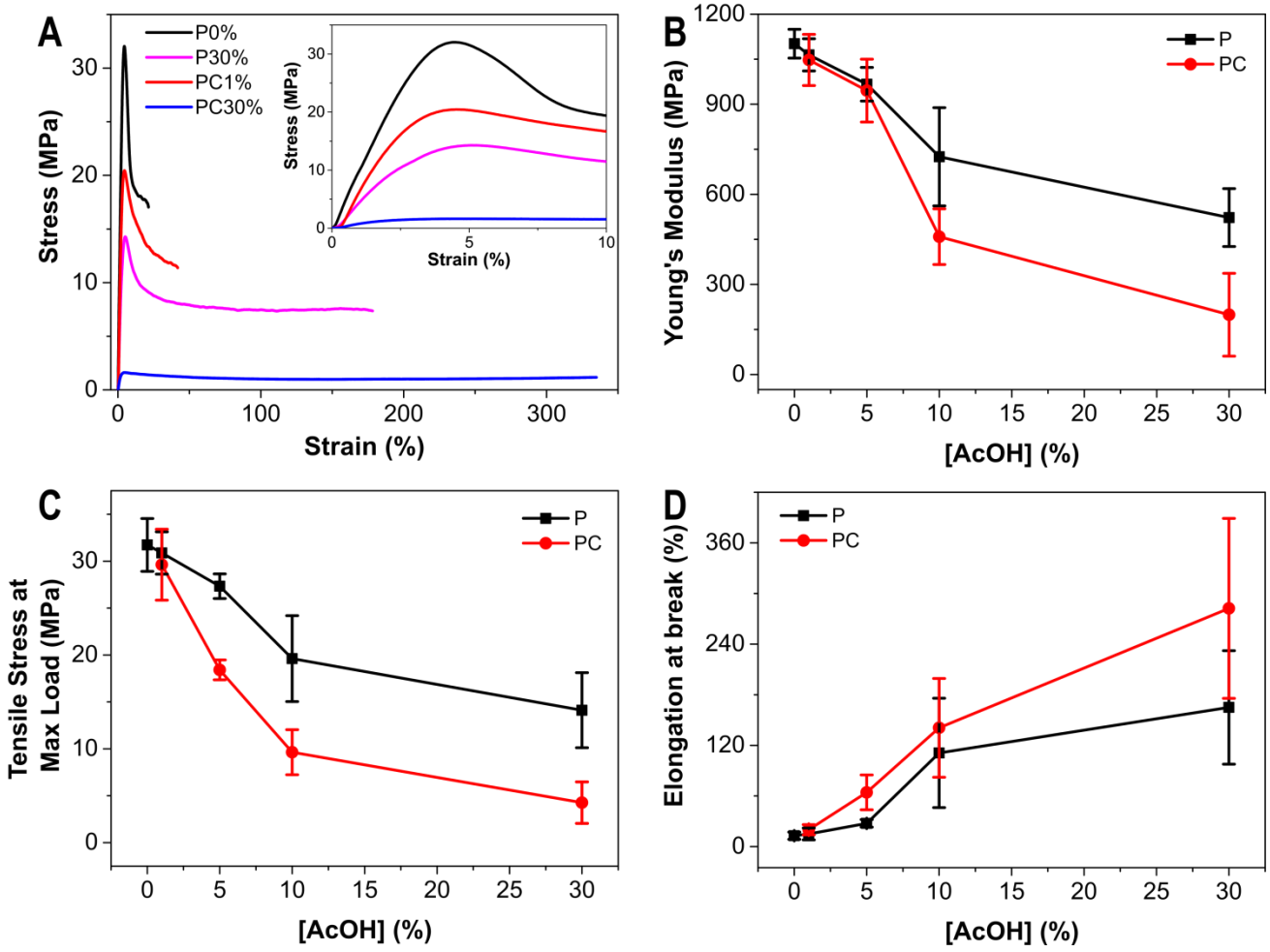

Figure 2.7 A, Stress–strain curves of P0%, PC1%, PC30% films. **B**, **C**, **D**, Young's modulus, tensile stress at maximum load and elongation at break of all films, respectively as a function of solution acetic acid concentration.

Films	Young's Modulus (MPa)		Tensile Stress at Max Load (MPa)		Elongation at break (%)	
[AcOH] (%)	*PVP*	*PVP Cipro*	*PVP*	*PVP Cipro*	*PVP*	*PVP Cipro*
0	1100±45	n.a.	32±2	n.a.	13±4	n.a.
1	1050±50	1050±85	30±2	29±3	15±7	20±6
5	970±50	950±100	27±1	18±1	27±4	64±20
10	725±150	450±100	19±4	9±2	111±64	140±50
30	525±100	200±125	14±4	4±2	165±67	280±100

Table 2.2 Mechanical properties (Young's modulus, tensile stress at maximum load and elongation at break) of films. Data are expressed as mean ± s.d. ($n \geq 5$).

2.3.6 Ciprofloxacin release studies

Although both the films and nanofiber mats developed in this study are envisioned as skin wound dressings, antibiotic release and film/mat dissolution characteristics in body fluid-like liquid media are also of pharmaceutical importance. The release data is plotted as the ratio of antibiotic concentration in the release medium (PBS solution) at a given time to the initial antibiotic concentration in the film (C/C_{tot}). Effect of aqueous acetic acid concertation on the release kinetics form transparent films is seen in Figure 2.8A. Approximately, within the first 150 seconds (2.5 minutes) upon immersion in PBS, in which about 20% of the initial antibiotic concentration is released, acetic acid concentration does not play a substantial role. Afterward, the transparent film produced by the minimum amount of required acetic acid in solution (1 vol.%) releases the antibiotic slower than the others reaching 100% release in about 10 minutes. Other transparent films with 5 wt. % and 10 wt.% acetic acid concentration reach 100% release condition in about half the time at 5 minutes. The film produced from aqueous solutions

with 30 vol.% acetic acid concentration is the fastest in releasing 100% of the antibiotic in about 4 minutes. In the case of nanofiber mats produced with the same acetic acid concentrations, however, no significant effect of acetic acid concentration on the release curves is present within the experimental statistics, see Figure 2.8B. This could possibly be attributed to the large surface area to volume ratio when the composites are produced as nanofiber mats instead of films. Complete antibiotic release from the mats occurs within 1.5 minutes. As such, it is encouraging to see that by simply changing the morphology of the polymer-Cipro composites into a nanostructured one instead of a bulky film, the release of the full antibiotic is accelerated by about fourfold.

Siepmann and Peppas [169] presented several detailed approaches to the use of semi-empirical mathematic equations for modeling drug release from hydrophilic water-soluble polymers such as hydroxypropyl methylcellulose. They concluded that the use of a simple empirical or semi-empirical model such as power laws is fully sufficient when the matrix is a hydrophilic polymer. The present release data from the films and the fibers were fitted with the Boltzmann equation:

$$y = \frac{A_1 - A_2}{1 + e^{(x - x_0)/dx}} + A_2 \qquad (1)$$

where x_0 is the center point; dx is the width; A_1 and A_2 initial and final y value, respectively.

Equation (1) allows calculation of the drug release half-life (C_{50}) corresponding to the time when half of the encapsulated drug is released into a perfect sink [169]. Figure 2.8C displays the half-life of both the transparent films and nanofiber mats produced by different acetic acid solutions in water. The trends in Figure 2.8C are striking in the sense that there exists a well-defined acetic acid concentration threshold for transparent films at around 5 wt.%. Before this threshold, increase in acetic acid concentration (between 0 wt.% to 5 wt.%) significantly reduces the half-life and afterward, the decline in the half-life is much less pronounced even if acetic acid is increased 6 fold to 30 vol.%. In contrast, the half-life of the nanofiber mats is an order of magnitude lower than the films, and they are much less sensitive to the increase in acetic acid concentration in water as seen in Figure 2.8C.

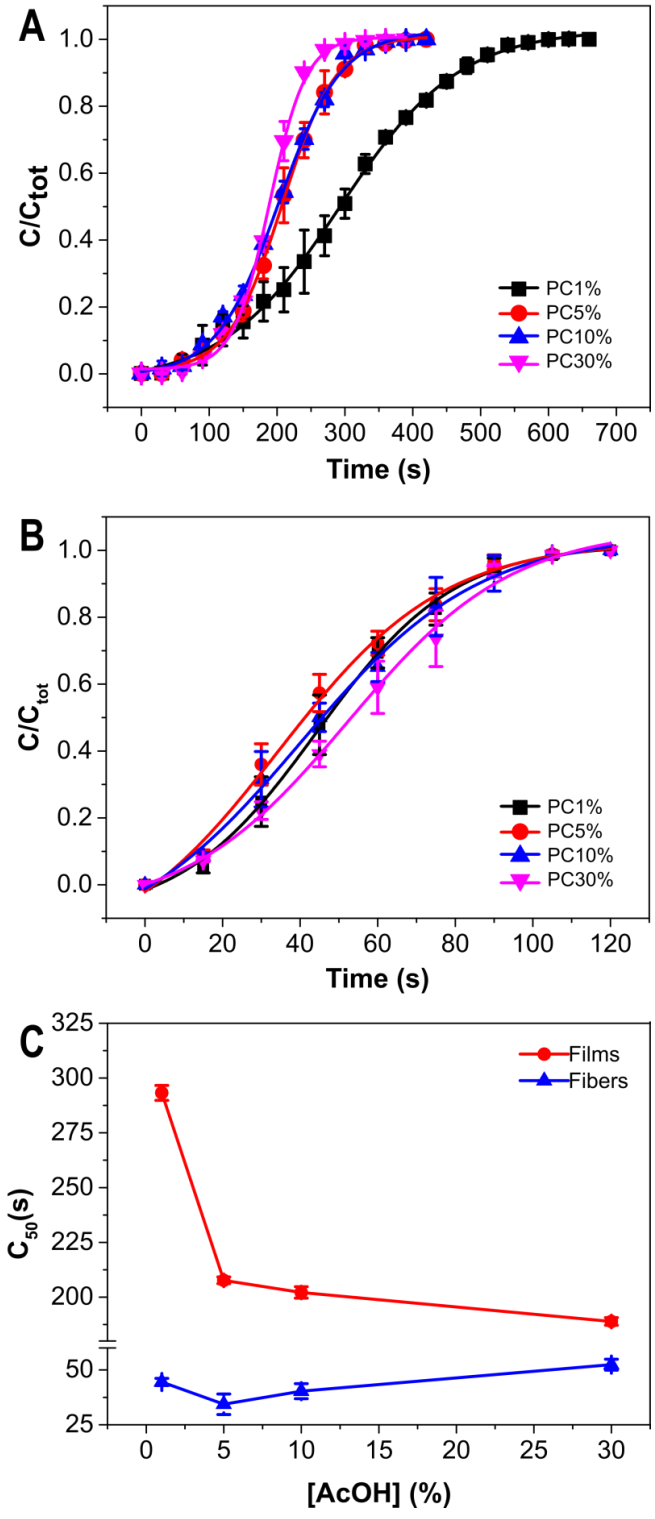

Figure 2.8 A,**B**, Release of Ciprofloxacin from films (A) and fibers (B), respectively. **C**, Time needs to release the 50% of the total quantity, C_{50}, of ciprofloxacin from films and fibers.

2.3.7 Antibacterial assays

Pure PVP samples (P0%) placed in the plates containing *E. coli* did not have any effect on the bacteria growth (Figure 2.9A). P1% and P30% films, instead, showed an inhibition zone under and around the films due to the effect of bound acetic acid (Figures 2.9B and 2.9C). Inhibition zone due to P1% films was 0.5% of the total bacteria covered area whereas the inhibition zone increased to 30% in the case of P30% films (Figures 2.9B and 2.9C). PC1% and PC30% films, on the other hand, showed a broader zone of inhibition, compared to P1% and P30% films due to Cipro (Figures 2.9D and 2.9E). Thus, PC1% and PC30%, showed an increased inhibitory effect against the growth of microorganisms, due to the synergic effect of Cipro and acetic acid. Calculated inhibition zone percentages as a function of acetic acid concentration for films and nanofibers are given in Figure 2.9F. When nanofiber mats were tested, the synergic inhibitory effect of Cipro and acetic acid was even more pronounced than the one observed with the films (Figure 2.9F). Contrary to *E. coli*, no antibacterial effect from acetic acid alone was observed with the bacteria strain of *B. subtilis*, even at the highest concentration tested (Figures 2.10B and 2.10C), identical to the control P0% samples (Figure 2.10A). This can be attributed to the high pH resistance of *B. subtilis* [170].

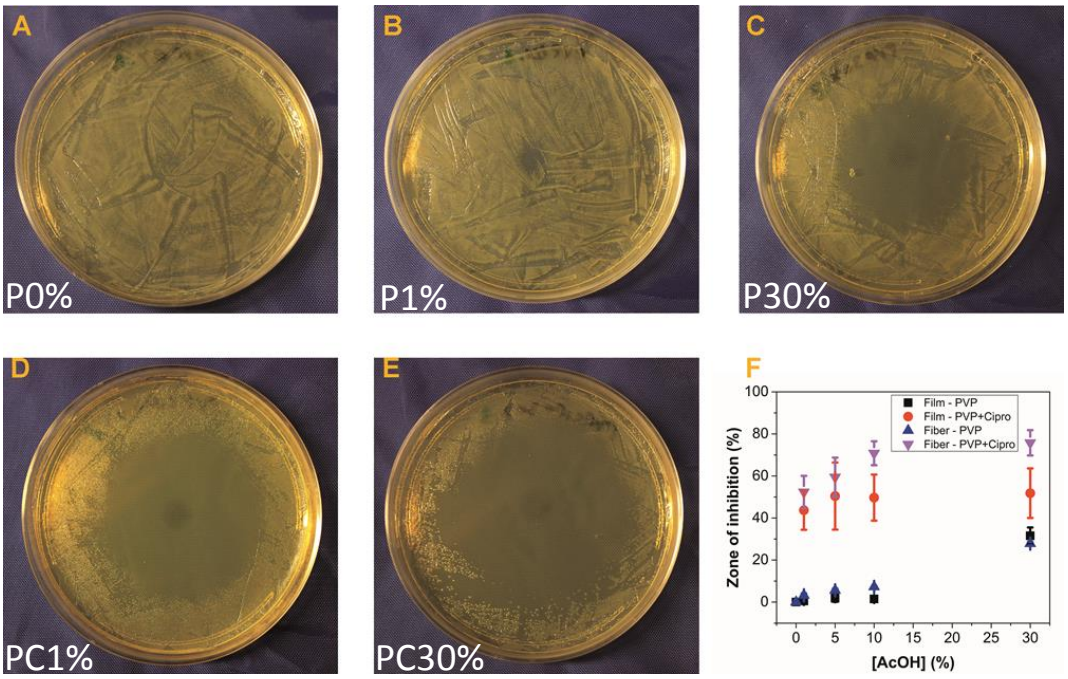

Figure 2.9 A-E, Photographs show the effect of P0%, P1%, P30%, PC1%, PC30% films, respectively, on *E. coli* colonies. **F**, Results of the inhibition-zone assay for all samples under analysis on *E. coli*.

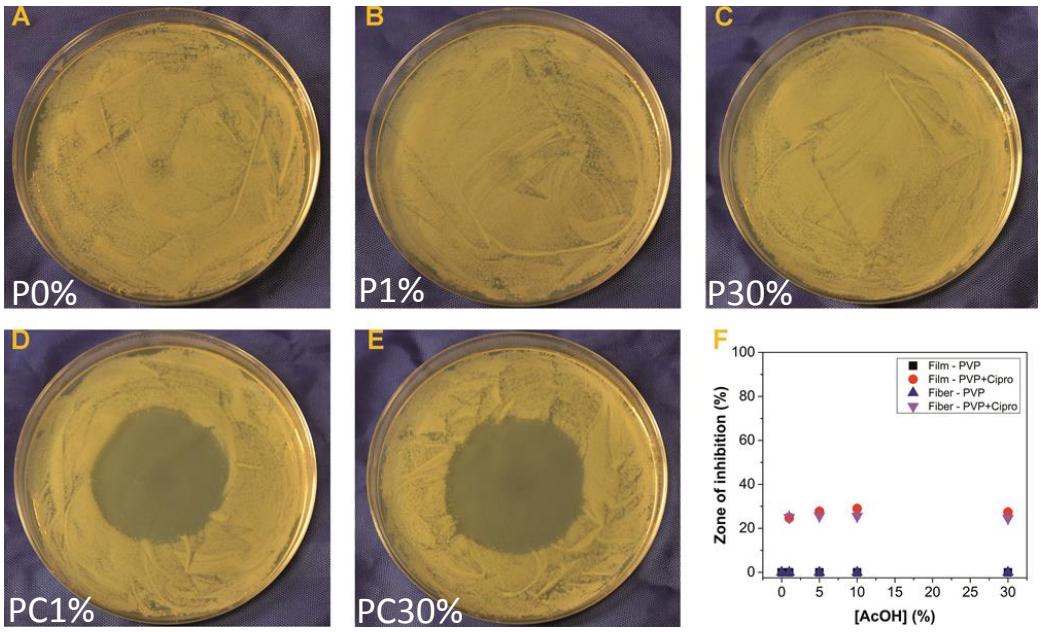

Figure 2.10 A-E, Photographs show the effect of P0%, P1%, P30%, PC1%, PC30% films, respectively, on *B. subtilis* colonies. **F**, Results of the inhibition-zone assay for all samples under analysis on *B. subtilis*.

Thus, the behavior of *B. subtilis* allows us to isolate the effect of Cipro alone, as acetic acid has no synergistic effect. In the plates containing *B. subtilis*, the antibacterial effect of the Cipro containing films and the nanofiber mats tested was again well visible as a broad zone of bacterial growth inhibition (Figures 2.10D and 2.10E). Notably, the size of the growth inhibition zone was identical in all the Cipro samples independent of solution acetic acid concentration (Figures 2.10D, 2.10E, and 2.10F). As such, both the transparent films and nanofiber mats functionalized with Cipro are effective against both Gram negative and Gram-positive bacteria.

2.3.7 In vivo full-thickness excisional skin wound healing mice model

To evaluate the *in vivo* bio-resorption and biocompatibility of antibiotic transparent films and nanofiber mats, they were tested in the skin full-thickness excisional mice model [171]. The biocompatibility and bio-resorption are key features to be monitored in the development of wound care, tissue repair and regenerative medicine dressings [172]. Furthermore, bio-resorption and drug release properties are interrelated, and resorption and rehydration characteristics should be optimum to maximize the therapeutic efficacy of the wound care products [173]. To evaluate the effect of acetic acid concentration on resorption, PC1% and PC30% samples (films and nanofibers) were tested. These materials were applied on fresh wounds and were monitored for a duration of 240 minutes (4 hours, Figure 2.11A). The application of both films and nanofibers was safe and biocompatible for the animal skin with no visible irritation effects. Resorption of the antibiotic films and nanofiber mats was quite diverse as illustrated in Figure 2.11. First of all, nanofiber mats degraded faster than transparent films. Even long after 240 minutes, transparent antibiotic films were not resorbed. In the case of nanofiber mats, for instance, at the end of 10 minutes twice as much PC1% nanofiber mat was resorbed compared to PC30% mat (see Figure 2.11B). At the end of one hour, however, percent resorption of both fiber mats were closer to each other. PC1% nanofiber mat was completely resorbed within 180 minutes after application on the wound, while PC30% nanofiber mat was completely resorbed within 240 minutes.

Moreover, as can be seen (comparing Figures 2.8 and 2.11), the rate of nanofiber mat degradation *in vivo* is much slower compared to *in vitro* PBS assay (2 minutes vs. 240 minutes). These preliminary observations on the animal models confirmed encouraging bio-resorption characteristics of the nanofiber mats.

On the other hand, nanofiber mats absorbed wound exudate faster than transparent films. Exudate absorption can be seen as a whitish color change in transparent films due to swelling induced by exudate liquids (Figure 2.11A). Both PC films started to absorb wound exudates a few minutes after the application, although more exudate adsorption was noticed in the PC1% film compared to the PC30% film 180 minutes after their application on the wound (Figure 2.11A). These results indicate that transparent antibiotic films could be sustained much longer on the wounds.

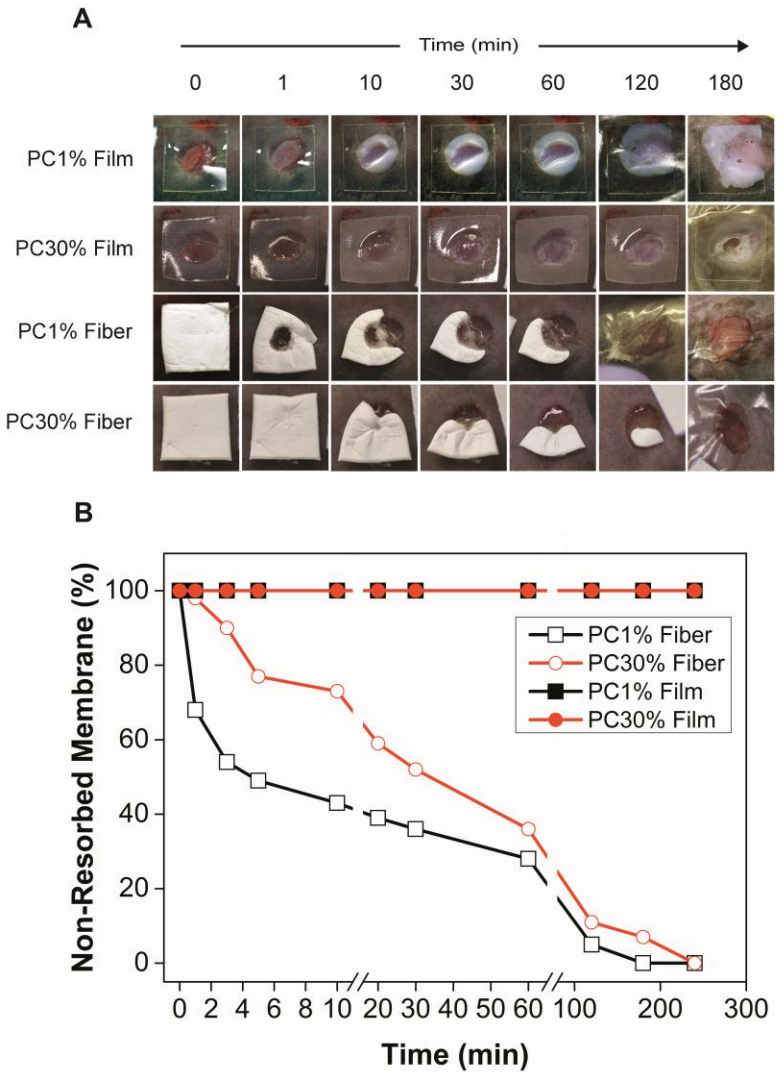

Figure 2.11 *In vivo* wound healing mice model. **A**, Sequence of photographs displaying films and nanofiber mats placed fixed on mice wound. Sterile Tegaderm film cover is visible on all wounds. **B**, Estimated percent resorbed membrane as a function of time based on digital image processing of the photographs.

2.4 Conclusions

A non-water soluble monohydrochloride monohydrate free ciprofloxacin (Cipro) antibiotic was introduced into a pharmaceutical polymer, polyvinylpyrrolidone (PVP), with the help of acetic acid as co-solvent in water. Upon casting from aqueous solutions fully transparent antimicrobial films were obtained. Acetic acid prevented *in situ* crystallization of the antibiotic causing the unexpected transparency. The solutions were also electrospun into nanofiber mats (non-transparent). Residual PVP-bound acetic acid in dry PVP films was around 1%, and it induced unprecedented levels of plasticity (stretching capacity) and softness to the films. Nanofiber mats contained much less bound acetic acid, namely, 0.1% with respect to the weight of the polymer matrix. It also functioned as an antiseptic. Antibacterial properties of the films and fiber mats were tested on *Escherichia coli* and *Bacillus subtilis* (growth and viability). Films and nanofiber mats had promising wound resorption characteristics confirmed by *in vivo* full-thickness excisional skin wound healing mice model. Nanofiber mats were resorbed much faster than transparent films. Wound exudate absorption in the films and resorption rate of the nanofiber mats were dependent on aqueous acetic acid concentrations. As such, these PVP/Cipro solutions in aqueous acetic acid can be used either to produce transparent soft films or nanofiber mats. The fabrication process is highly suitable for designing new-generation potential dressings for wound management and care.

Further characterization of these two promising antibacterial wound dressings will be shown in chapter 4.

Chapter 3 : Multifunctional bilayer wound dressing

3.1 Bilayer design as suitable strategy for multifunctional dressings

Wound healing is a complex succession of biological events, as described in the introduction of this thesis. For this reason, a wound dressing has to be designed as a smart multifunctional material able to be active in all the phases of the recovery. One of the potential winning strategies is to make use of multi-layers dressings that can regulate bioactive molecule release and boost regeneration and remodeling of derma epithelium in a sequential manner over time [174-177]. For instance, Yannas *et al.* [178-180] were the first to propose a bilayer dressing to treat skin wounds. The design involved functionalized layers in which a substratum with a porous structure was made to promote cell migration, while a silicon-based top cover was used to avoid bacterial infections and water loss. This concept and the material system are now commercialized under the name Integra®. However, this construct has limitations such as poor adhesion to the wound bed, difficult removal of the artificial extracellular matrix after the application on the wound, and lack of active agents against infectious bacteria [63, 86, 87, 89, 90]. Nevertheless, Yannas *et al.* [178-180] bilayer structure inspired numerous wound dressing constructs [89, 181] and, recently, new bilayer wound gauzes have emerged. For instance, Reyes-Ortega *et al.* [182] fabricated a non-porous bilayer with a first layer of crosslinked gelatin-hyaluronic acid (HA) and a second one based on polyurethane derivative as a drug controlled release system for the delivery of two bioactive agents, proadrenomedullin N-terminal 20 peptide (PAMP) and bemiparin, respectively for wound healing. Likewise, Thu *et al.* [183, 184] demonstrated the application of alginate-based bilayer wound dressings as controlled release device by simply casting a top active layer over a bottom supportive one. Zilberman *et al.* [185] produced a hybrid bilayer comprising of a porous top layer of poly(lactic-co-glycolic acid) loaded with an antibiotic, and a sponge-like sublayer of collagen. Similarly, Priya *et al.* [34] fabricated a porous bilayer based on Polyvinylpyrrolidone-iodine complex (PVP-I) and gelatin. Despite these recent advances, developing cost-effective multi-functional and transparent wound care dressings that feature good interactions with

the exudate, and conformal adhesion to the wound, while promoting healing and resisting bacterial biofilm formation and infection, is still an appealing and challenging task [132, 186, 187]. Moreover, achieving such constructs using energy efficient processes and ecofriendly materials and solvents (*i.e.* water) would constitute an important benefit.

Herein, I present a multi-functional bilayer wound dressing construct comprising polyvinylpyrrolidone (PVP) and hyaluronic acid (HA) as transparent matrices embedding a cutaneous antiseptic and an antibiotic, respectively, by using an ecofriendly water-based approach with easy scale-up potential. The bilayer structure consists of a top PVP layer loaded with the cutaneous antiseptic, Neomercurocromo® (Neo), and a bottom layer composite blend of HA and PVP loaded with the antibiotic Ciprofloxacin (Cipro). The latter layer was designed to serve two purposes, namely infection prevention/treatment, and potential enhancement tissue remodeling. This bilayer system is transparent, self-adhesive, flexible and it is capable of releasing the cutaneous antiseptic and the antibiotic in a controlled manner over a period of 5 days. Antibacterial tests were performed against three different strains, *Staphylococcus aureus* (*S. aureus*), *Escherichia coli* (*E. coli*) and *Pseudomonas aeruginosa* (*P. aeruginosa*).

Moreover, biocompatibility, hemocompatibility and anti-inflammatory properties of the bilayer were evaluated *in vitro*. A full-thickness excision *in vivo* model also revealed the construct's ability to be completely resorbed by the wound, most likely via integrating into the repaired tissue. Furthermore, both the levels of inflammatory mediators, such as IL-1β and TNF-α, and the rate of wound closure after the application of the bilayer were investigated. It is also demonstrated the possibility of fabricating the constructs using a pilot-scale rod coating technique to address the potential scale-up not only for production point of view but also for treating much larger skin wounds.

3.2 Materials and Methods

3.2.1 Materials

Polyvinylpyrrolidone (PVP; MW= 360,000), monohydrochloride monohydrate free ciprofloxacin (Cipro; ≥98.0% HPLC; MW= 331.34), acetic acid (AcOH; ≥99.7%), glycerol, and phosphate buffered saline (PBS) solution (pH 7.4) were purchased from Sigma-Aldrich (St. Louis, MO, USA). Hyaluronic acid sodium salt (HA; MW=350,000) was purchased from Abcr (Germany). All the purchased products were used as received. Deionized water was obtained from Milli-Q Advantage A10 ultrapure water purification system. The cutaneous antiseptic was a commercial product, Neomercurocromo® (Neo), produced by Laboratorio Farmaceutiche Specialità Igienico Terapeutiche S.I.T. s.r.l. (Pavia, Italy). Neo is a liquid mixture of 2.0 g of Eosin, 0.3 g of Chloroxylenol, and 30.0 g of propylene glycol dispersed in purified 100 mL of water with trace amounts of ethanol and sodium EDTA. According to the Italian drug regulatory agency (Agenzia Italiana del Farmaco, AIFA), Neo possesses high biocompatibility, it can be directly applied on a wound without causing discomfort or burning sensation, and it is able to accelerate the wound healing process.

In particular, the functional molecule Eosin is mildly bacteriostatic against gram-positive bacteria and antifungal. Moreover, it can reduce the levels of pro-inflammatory cytokines and promote injured skin re-epithelialization [171, 188]. Chloroxylenol is a mild disinfectant and is included in the World Health Organization model list of essential medicines [189]. Lastly, propylene glycol favors diffusion of active principles through the skin and the wound tissue. Dulbecco's modified Eagle's medium (DMEM), fetal bovine serum (FBS), L-glutamine and penicillin-streptomycin were purchased from Euroclone (Milan, Italy). PBS with Calcium and Magnesium (PBS with Ca^{2+}/Mg^{2+}) was obtained from Sigma Aldrich (St. Louis, MO, USA). CellTiter-Glo reagent was purchased from Promega (Madison,

WI, USA). Human foreskin fibroblasts (HFF-1) were purchased from American Type Culture Collection (ATCC®).

3.2.2 Methods for the bilayer preparation

The bottom layer was fabricated by dissolving HA, PVP, ciprofloxacin, and glycerol in acetic acid (AcOH)/water solution (1% v/v in AcOH). Glycerol was used as a plasticizer that amounts to a concentration of 10 wt. % with respect to total polymer dry film weight. Ciprofloxacin, 0.014% (w/v), was dissolved in the aqueous AcOH solution. Afterward, equal weights of PVP and HA (1:1, w/w) were dissolved in the same solution to reach a final concentration of 2% (w/v). The solution was cast into circular plastic Petri dishes with a diameter of 50 mm and dried for 3 days under an aspirated hood in ambient conditions (16-20 °C and 40-50% relative humidity (R.H.)). For the fabrication of the glycerol plasticized (10 wt. % dry basis) top PVP layer containing cutaneous antiseptic Neo, two methods were implemented: spin-coating (smaller samples) and a spread-rod-coating (larger samples). A Spin-coater (model WS-650S-6NPP/LITE/OND by Laurell Technologies Co.) and a Rod-coater system (model EZ coater EC-200; ChemInstruments) were used, respectively. In both cases, 10 mL of an aqueous solution of PVP 20% (w/v), containing glycerol (10 wt. % w.r.t. PVP) and 1 mL of Neo was prepared.

For the spin-coating approach (Figure 3.1A), the first layer was immobilized on a stage via air suction, and 4 mL of the second layer solution were added with a syringe. The spin coater was set up to run at 1000 rpm for 3 minutes. The obtained bilayer was dried under a hood for one day at ambient conditions (16-20 °C and 40-50% R.H.). In the rod-coating approach (Figure 3.1B), a rectangular sample of the dry bottom layer (15 × 30 cm) was laid down and fixed firmly with a snap action clip, and the rod position was adjusted at a distance of 100 µm from the surface of the dry film. Afterward, 5 mL of the aqueous top layer solution were spread in the vicinity of the rod and along the rod length; the rod was moved from one end of the film to the other spreading the liquid over the film. The coating was

allowed to dry for 24 hours. Figure 3.1C shows photographs of circular spin coated bilayer constructs and a larger rectangular specimen with the much larger size.

A number of reference or control samples were also prepared in order to better interpret both the drug release and the antibacterial efficiency of individual layers in comparison to the full construct. More specifically, the samples tested were full bilayer construct (BL), the bilayer construct with no Ciprofloxacin (BLN), the single bottom layer (SLHC), the single bottom layer only without HA (SLPC), and the single bottom layer without Ciprofloxacin (SLHP). The respective solution formulations corresponding to each sample are given in Table 3.1.

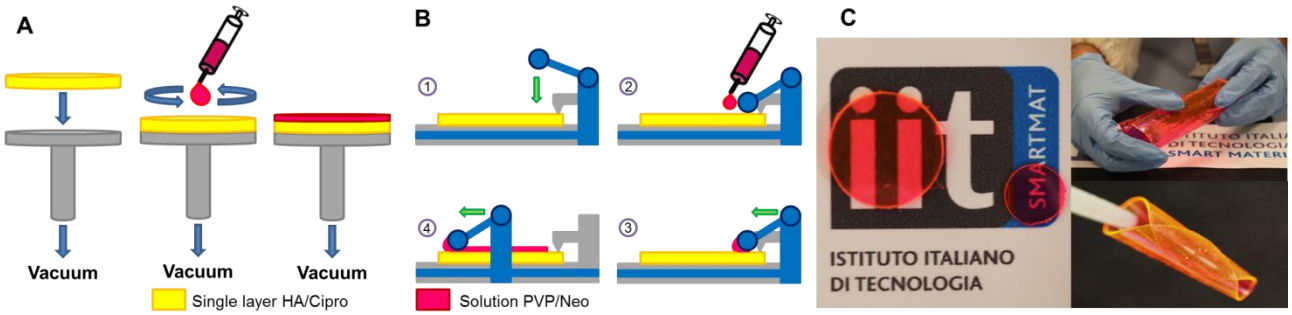

Figure 3.1 A, **B**, Schematic representation of the spin-coating and rod-coating fabrication processes. **C**, Photographs of bilayer constructs. Larger samples are made by rod coating. Transparency is evident as well as plasticization due to glycerol. PVP/Neo denotes the top layer (wound contact).

Labeling	Structure	Ingredients of starting solutions (w/v)					
		PVP	*HA*	*Neo*	*Cipro*	*AcOH*	*Glycerol*
BL	Top Layer	20%	-	10%	-	-	2%
	Bottom Layer	2%	2%	-	0.01%	1%	0.40%
BLN	Top Layer	20%	-	10%	-	-	2%
	Bottom Layer	2%	2%	-	-	-	0.40%
SLHC	Single Layer	2%	2%	-	0.01%	1%	0.40%
SLPC	Single Layer	3%	-	-	0.01%	1%	-
SLHP	Single Layer	3%	2%	-	-	1%	0.40%

Table 3.1 Composition of the fabricated samples. All the reported values represent percentages of material weight in the solution volume (w/v), while for the acetic acid (AcOH) the value designates a volume ratio (v/v).

3.2.3 Morphological Analyses

Morphology of the bilayer films was analyzed by scanning electron microscopy (SEM), optical microscopy (OM), and two-photon microscopy. Samples for light microscopy were obtained by cutting cross-section slices with Leica UCS ultramicrotome equipped with a glass knife: 1 μm thick sections were mounted on a glass microscope slide using Eukitt (quick hardening mounting medium – Sigma Aldrich). The flat cross-section of the bilayer obtained after ultramicrotome cutting was used for SEM analysis, after sputter coating the surface with a thin layer of gold. SEM imaging was performed using

SEM JEOL-JSM 6490 operating with an acceleration voltage of 10 kV. Optical images were acquired by a home-made microscope equipped with a 10x-0.4 NA objective (Olympus, Inc.), coupled with CMOS camera (Thorlabs, model DCC1645C). Two-photon microscopy characterization was carried out by using a NikonA1r Multiphoton coupled to a Coherent Chameleon Ti:Sapphire laser. Emission of Ciprofloxacin was acquired tuning the laser wavelength at 720 nm and collecting the photons with a 450/50 bandpass filter, while the emission of Eosin was acquired tuning the laser WL at 900 nm and collecting the photons with a 575/50 bandpass filter.

3.2.4 Variable-angle ATR-FTIR analysis

Variable-angle ATR-FTIR spectra of the samples were obtained with an ATR accessory (Veemax III, PIKE Technologies) coupled to a FTIR spectrometer (Equinox 70 FT-IR, Bruker). All spectra were recorded in the range from 3800 to 600 cm^{-1} with 4 cm^{-1} resolution, accumulating 128 scans. In a typical measurement, the films were gently deposited on the spot of the ATR accessory (ZnSe crystal) and slowly pressed. The analyzed depth, d_p, of ATR-FTIR spectroscopy depends on several factors such as the wavelength λ, the effective angle of incidence θ_e, the refractive index of the ATR crystal n_1, and the sample n_2, as indicated in the following equation:

$$d_p = \frac{\lambda}{2\pi n_1 \sqrt{\sin^2 \theta_e - (n_2/n_1)^2}} \qquad (1)$$

In our variable-angle ATR-FTIR spectrometer $n_1 = 2.4$, n_2 is assumed to be around 1.5 and θ_e may be calculated from the set angle θ_s, n_1, and the face angle of the crystal θ_f:

$$\theta_e = \theta_f + \sin^{-1}\left(\frac{\sin(\theta_s - \theta_f)}{n_1}\right) \qquad (2)$$

Table 3.2 shows the different θ_e and the d_p values at 1000 cm^{-1} for all the set angles used in this study. All spectra were normalized to the d_p at 1000 cm^{-1} using the "ATR correction" command provided for the software (Spectra Manager v2). All spectra showed were measured at 45°, unless otherwise indicated.

θ_s (°)	θ_f (°)	θ_e (°)	d_p at 1000 cm^{-1} (μm)
35	45	40.85	8.75
40	45	42.92	5.73
45	45	45	4.37
50	45	47.08	3.55
55	45	49.15	2.99
60	45	51.19	2.58
65	45	53.19	2.26
70	45	55.14	2.01
75	45	57.02	1.80

Table 3.2 Calculated effective angles and analyzed depths for the different set angles used.

3.2.5 Adhesion and mechanical properties

Peel adhesion tests were carried out on a dual column universal testing machine (Instron 3365) equipped with a custom setup based on ISO 8510 standard: a volunteer's human arm was placed on the horizontal moving table, the sample was gently applied to either dry or wet skin, and one end was clamped. The upper clamp was displaced upward with the constant rate of 50 mm/min; the table was moved horizontally by a pulley so that the peeling angle was constant (90°). The set-up is shown in Figure S2A (Supporting Information). The peeling force was measured throughout the test and normalized over the sample width. At least three repetitions were conducted for each sample. The mechanical properties of the full bilayer sample were determined by uniaxial tension tests using the same Instron 3365 dynamometer. Films were cut in dog bone specimens with a width of 4 mm and an effective length of 25 mm. Displacement was applied to the rate of 10 mm/min. From the resulting

stress-strain curves, the elastic modulus, ultimate tensile strength (UTS), elongation at yield and elongation at maximum load were extracted. The measurements were performed on at least 7 samples. All the stress-strain curves were recorded at 25 °C and 44 % R.H.

3.2.6 Water absorption

The water absorption capacity of the bilayer films was obtained as follows: seven dry samples were weighed (~ 100 mg) on a precision electronic balance and were placed in different chambers with controlled, increasing humidity. The humidity conditions were: 0%, 11%, 44%, 84%, 100%. Prior to humidity chamber tests, samples were dried in a desiccator until no change in sample weight was measured. After conditioning in different humidity chambers until equilibrium conditions (24 hours), each film was weighed, and the amount of absorbed water was calculated based on the initial dry weight.

3.2.7 Drug release studies

The release of Ciprofloxacin and Eosin (Neo) from the bilayer samples were measured using a CARY 300 Scan UV–visible spectrophotometer. Ciprofloxacin and Eosin (Neo) present characteristic UV absorbance peaks at 272 nm and 517 nm, respectively. To extrapolate the molar extinction coefficients, calibration curves for each drug were constructed, which led to ε = 37,900 cm^{-1} M^{-1} for Ciprofloxacin and ε = 86,700 cm^{-1} M^{-1} for Eosin (Neo). Bilayer samples were cut in round shapes with a diameter of 1.4 mm and placed in a 24-well plate, after carefully checking the correct positioning of the top and bottom layers by means of FT-IR measurements (bottom layer HA/Ciprofloxacin attached to the well, and top layer PVP/Neo facing up). Afterward, 2.5 mL of PBS were gently added into each well. At each time point, 300 µL of the solution were taken out and mixed with 700 µL of fresh PBS in a cuvette, for the UV analysis. Fresh PBS (300 µL) was added to each well, to maintain the sinking conditions. The experiments were carried out in an incubator at 37 °C, under controlled humidity and

CO_2 conditions. For each sample under analysis, triplicates were considered, and the experiment was repeated twice. Data were expressed as a cumulative percentage.

3.2.8 Biocompatibility assay

3.2.8.1 Sample preparation and extraction for in vitro assay

Samples preparation method was modified from ISO10993-12 and an extraction ratio of 1.5 cm^2/mL (surface area/volume) was used to prepare the samples. In order to standardize the treatments, we determined the weight of the main samples under analysis corresponding to the surface area chosen, as reported in Table 3.3, and a weight-to-volume ratio was utilized for the extraction process (as extensively described in the work of Summa *et al*. [190]). Extraction medium from each sample was prepared to adapt the procedure described in ISO10993-5 standard test. Briefly, samples were sterilized under a germicidal UV lamp for 30 min/side, and cut into small pieces, to reduce their dimension and improve the extraction process. Extraction was performed in cell culture medium for 24 h at 37 °C and the medium was used immediately after preparation.

Table 3.3 Film characterization for *in vitro* studies.

Samples	Weight average* (mg)	S.D. (mg)
SLHC	35.8	5.1
BL	38.8	6.5
BLN	40.5	5.2

*At least 7 samples were weighted to calculate weight average corresponding to 1.5 cm^2.

3.2.8.2 In vitro biocompatibility assay

HFF-1 cells were grown in DMEM supplemented with 10% FBS, 2 mM L-glutamine, 100 IU per ml penicillin and 0.1 mg/mL streptomycin, in a humidified incubator at 37 °C with 5% CO_2. The cytotoxicity assay was performed using a procedure previously described [83] with slight modifications. Briefly, HFF-1 cells were seeded in 96-well plates at a density of 8 x 10^3 cells and cultured for 24 h. Then, the culture medium was removed, and cells were treated with extraction medium (control samples were treated with medium processed as the extractions). After 24 hours of treatment, cells were rapidly rinsed with pre-warmed PBS with Ca^{2+}/Mg^{2+}, and the extraction medium was replaced with fresh one. Cell viability was determined to measure ATP levels by CellTiter-Glo assay, as indicated by the supplier. Cell viability was expressed as percentage survival relative to control cells.

3.2.8.3 Data analysis

One-way ANOVA was used to evaluate statistical significance, followed by Bonferroni's *post hoc* test. GraphPad Prism 5 was used for all statistical analysis (GraphPad Software Inc. San Diego, CA, USA). *p* values less than 0.05 were considered significant.

3.2.9 Hemolysis assay

Hemolysis assay was performed using a procedure previously described by Picone *et al.* [191]. Briefly, 5 mL of venous blood collected from a healthy donor was drawn directly into K2 EDTA coated Vacutainer tubes to prevent coagulation. After centrifugation at 500 g for 5 min, the hematocrit and plasma level was marked on the tube. Then, the plasma was eliminated and replaced with 150 mM NaCl, and the tube was centrifuged at 500 g for 5 min. This step was repeated three times, and at the end, the supernatant was replaced with PBS at pH 7.4. 200 μL of diluted (1:50 in PBS) erythrocytes were layering into a 96-well plate. After that, a bilayer of different weight (2, 4, 6 mg) or 10 μL of 20% Triton X-100, as a positive control, were added to the erythrocytes sample. The plate was incubated at

37°C for 3 h and then centrifuged for 5 min at 500 g to pellet whole erythrocytes. Then, 100 μL of the supernatant was transferred from each well into a clear, flat-bottomed 96-well plate and absorbance, due to free hemoglobin presence, was red at 490 nm by using a plate reader (Wallac Victor 2 1420 Multilabel Counter (PerkinElmer, Inc. Monza, Italy). After background subtraction, the average absorbance of the positive control was determined. All experimental data points were normalized with this mean absorbance value, which represents 100% hemolysis. The treated erythrocytes and the control were morphologically analyzed by microscopy inspection on an Axio Scope 2 microscope (Zeiss).

3.2.10 ELISA tests

Peripheral blood mononuclear cells (PBMc) were isolated from venous blood collected by young and healthy donors and achieved as described by Picone *et al.* [192]. PBMCs were incubated with lipopolysaccharide (LPS) (0.1 μg mL-1) as activators of the inflammatory response, in the presence or not of bilayer complete for 24 h. An enzyme-linked immunosorbent sandwich assay (ELISA) (Invitrogen) was performed for quantitative detection of Tumor Necrosis Factor α (TNFα) and interleukin 6 (IL-6) in cell culture supernatants.

3.2.11 Antibacterial studies

3.2.11.1 Bacteria strains and culture conditions

Three reference bacterial strains (the Gram-positive *Staphylococcus aureus* ATCC 29213 and the Gram-negative *Escherichia coli* ATCC 25404 and *Pseudomonas aeruginosa* ATCC 27853) were used for antimicrobial studies. Bacterial strains were obtained from the American Type Culture Collection (ATCC®). All the strains were cultured in Mueller Hinton Broth (MHB) and/or Agar (MHA) at 37°C.

3.2.11.2 Agar disk-diffusion method

Agar disk-diffusion assay was performed against *S. aureus*, *E. coli*, and *P. aeruginosa*. The protocol was based on the M02-A document of CLSI (Clinical and Laboratory Standards Institute) for bacteria testing[193].Overnight cultures were centrifuged at 4500 x *g*, rinsed with phosphate buffered saline (PBS, pH 7.4) two times and resuspended in PBS to approximately 10^9 CFU/mL. MHA plates were inoculated with 10^8 CFU (equivalent to 0.5 McFarland standard) spread onto the agar surface. Samples were cut in 1.4 cm diameter disks and sterilized under a germicidal UV lamp (30 min/side). Dressing disks were placed at the center of MHA plates and incubated overnight at 37 °C. The inhibition zone diameters (IZDs) surrounding the tested samples were then measured using a digital caliper. Triplicate determinations were made for each batch of films. Films containing no drug were used as a control in the study.

3.2.11.3 Time-kill kinetics test

Time-kill kinetics of BL, BLN, and SLHC were performed against *S. aureus*. Samples were cut in 1.4 cm diameter disks and sterilized as previously described. Disks were inserted in sterile 4 mL glass tubes and used to perform microbial incubations. The time-kill test has been performed according to the M26-A guideline of CLSI[194]. This guideline describes detailed procedures and analysis of results for bactericidal testing. Bacteria were subcultured until exponential phase in MHB, and 1 mL inoculum of approximately 5×10^5 CFU/mL was added to each sample to test. After incubation at 37°C, samples were taken out at 0, 1, 2, 3, 6, and 24 h. In particular, 100 µL of sample were withdrawn from each tube, and 10-fold dilutions in sterile saline solution (0.9% NaCl) were prepared. Bacterial growth was quantified by dropping 10 µL from each serial dilution (from 10^{-1} to 10^{-7}) on MHA plates. Using this method, 7 serial dilutions were seeded on a single plate. Colonies were counted after 15 - 24 hours of incubation at 37 °C, and the averaged means were then transformed and expressed as mean Log10 CFU/mL. Results were presented in the format of a “time-kill curve” by plotting the obtained viable

mean Log10 counts (CFU/mL) at each investigated time point for each sample and growing control against time (1, 2, 3, 6, 24 h). Following the approved guideline CLIS M-26A, bactericidal activity was defined as a 3 Log10 reduction in CFU/mL compared to the growing control [195]. One-way analysis of variance (ANOVA) was performed, with statistical significance defined as $p < 0.05$.

3.2.12 In vivo full-thickness excisional skin wound healing mice model

3.2.12.1 Animals

In-vivo experiments were carried out in accordance with the guidelines established by the European Communities Council Directive (Directive 2010/63/EU of 22 September 2010) and approved by the National Council on Animal Care of the Italian Ministry of Health. 8–12 week-old male C57BL/6J mice (Charles River, Calco, Italy) were used. All efforts were made to minimize animal suffering and to use the minimal number of animals required to produce reliable results, according to the 3Rs. They were maintained under a 12-hour light/dark cycle (lights on at 8:00 am) under a controlled temperature of (21 ± 1 °C) and relative humidity of (55 ± 10%) conditions.

3.2.12.2 Resorption test

Dorsal skin of mice was shaved after light anesthesia induced by intra-peritoneal injection of ketamine (10%) and xylazine (5%) mixture. One full-thickness skin wound was created in the center of the back of each animal, using a sterile 6-mm biopsy punch. The wounds were photographed and then covered with the bilayer complete films (n = 5 for each experimental group).

To avoid the removal of the dressings when the animals were awoken, all treated wounds were covered with Tegaderm™ just before the animals woke, until the end of the experiment. Photographs were acquired at different time intervals (1, 3, 5, 15, 30, 60, 120, 240, 360 minutes, and 24 and 48 hours), after the dressing application to evaluate bio-resorption over time. Each photograph of the dressing on the wound was analyzed by ImageJ software, to calculate the percentage of the bio-resorbed membrane

during the time [158]. Mice were housed individually during the experiments, with water and food *ad libitum*.

3.2.12.3 Cytokine expression measurements

Skin samples from naive, sham, and bilayer treated animals were collected 2 days post wound induction and snap-frozen in liquid nitrogen (n = 5 mice in each experimental group). Cytokines (IL-1β and TNF-α) expression were measured using ELISA quantikine kit (R & D system), according to the manufacturer's instructions [171]. The cytokines concentration was normalized against the total protein content for a given sample, as measured using the bicinchoninic acid (BCA) assay (Thermo Scientific, Rockford, IL, USA).

3.2.12.4 Wound closure investigation

For the evaluation of the wound closure, mice were prepared as described above in the resorption section. Therefore, mice were anesthetized, their dorsal surface was shaved, and a full-thickness excisional wound was induced (diameter 6 mm). A photo of the wound was taken immediately after the biopsy generation (day 0). The bilayer dressing was applied, and all the treated mice were covered with TegadermTM to evaluate and measure wound closure photos at day 0, 3, 5, 7, 9 and 12 were collected and analyzed by using ImageJ software, Figure 4.10A. The wound closure was calculated as a percentage based on wound size relative to the control group. During the experiments, mice were housed individually and fed with water and food *ad libitum*.

3.3 Results and discussion

Selection of components and the specific structure that constitute the bilayer films are based on a number of reasons. The first and foremost is to demonstrate the capability to produce multifunctional bilayer films using eco-friendly methods with scale-up potential. Secondly, to ensure that the drug-

loaded HA/PVP blend remains transparent. HA is a natural polysaccharide present in the human body. It is a component of the extracellular matrix (ECM) and synovial liquid. HA is actively involved in the wound healing process that promotes proliferation and migration of epithelial cells, such as keratinocytes, and in modulating the inflammatory response [196-202]. The synthetic polymer PVP is known to be a hydrogen-binding polymer, a suitable property to fabricate multi- / bi-layer systems with enhanced skin adhesion capability [175]. The broad-spectrum antibiotic Ciprofloxacin is also used for the fabrication of these materials, for more details see the previous chapter. Lastly, the cutaneous antiseptic Neo is a highly stable suspension that can be easily incorporated in various aqueous polymer solutions [171]. The reason for using 1 % acetic acid solution during the preparation of the bottom layer is to prevent re-crystallization of Ciprofloxacin during drying of the films to ensure transparency [203].

3.3.1 Morphological attributes

To investigate whether the two drugs remained separated and confined within their respective layers, measurements with single and two-photon optical microscopes were conducted. Figure 3.2A demonstrates the overlay of the two-photon microscopy images pertaining to the top and bottom layers containing Eosin (red) and Ciprofloxacin (blue), respectively. As can be seen, the top layer is about 60 microns thick and the bottom layer is thicker, being close to 200 microns. The existence of an interfacial purple zone of about 10 micron thickness indicates that a limited infusion of Neo into the HA-PVP composite layer occurs during the coating process. This is attributed to the partial swelling of the bottom layer during the application and drying phase of the of the PVP-Neo coating.

Confirmation of this observation is given by the optical microscope images of Figure 3.2B (rod coating) and 3.2C (spin coating). A light pink interfacial zone is also visible in both optical images. Further inspection of the cross section of both spin and rod coated films is conducted with SEM as shown in Figures 3.2D and 3.2E. The thickness of the bottom HA/Ciprofloxacin stratum was indeed

200 ± 20 µm, while the top PVP/Neo layer was measured to be 60 ± 20 µm thick by utilizing several different samples. This indicates that no significant thickness changes occur once the fabrication process is changed and both top and bottom layer thickness can be reproduced at different sizes regardless of the fabrication approach. Note that the arrows in Figure 3.2E indicate edge defects due to the ultramicrotome cutting during sample preparation.

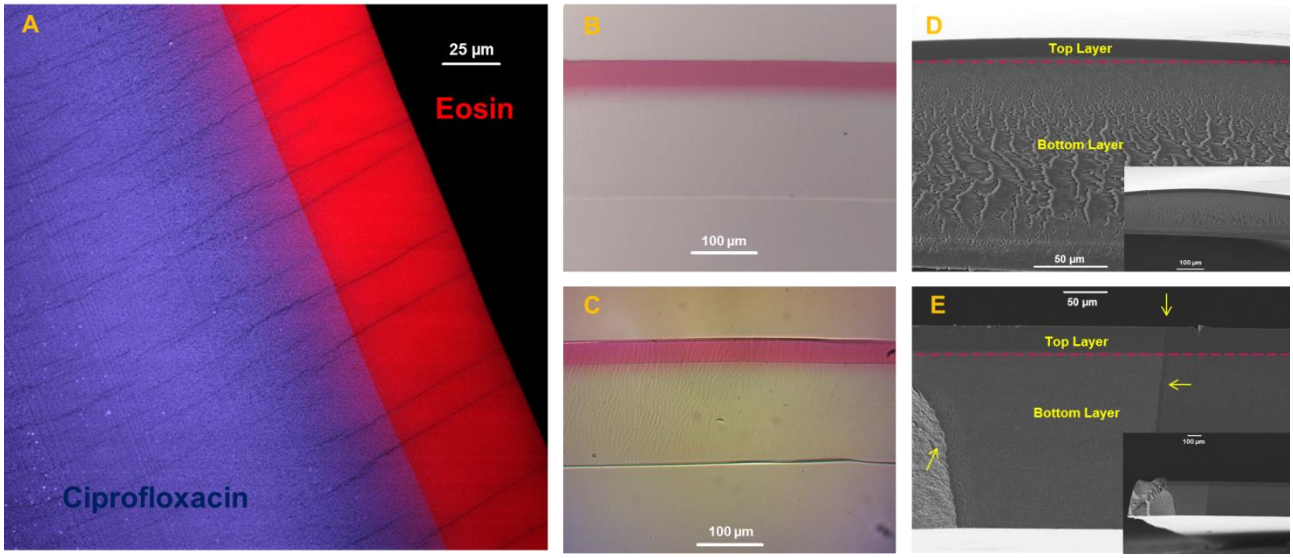

Figure 3.2 A, Two-photon microscope image of the bilayer fabricated by spin-coating. **B**, **C**, Optical microscope images of the materials obtained by rod and spin coating, respectively. **D**, **E**, SEM micrographs depicting the cross-section morphology of bilayer films fabricated by rod and spin coating, respectively. The insets show some deformations and edge effects during sample cross-section preparation but the samples are preserved well.

3.3.2 Chemical characterization and adhesive properties

The chemical composition of the top and bottom layers was analyzed by ATR-FTIR (Figure 3.3). Figure 3.3A displays the infrared spectra of both layers. Main bands of the top layer are associated with the functional groups present in the PVP polymer (O-H stretching mode at 3326 cm^{-1}, asymmetric and symmetric CH_2 stretching mode at 2955 cm^{-1} and 2883 cm^{-1}, respectively, C=O stretching mode at

1649 cm^{-1}, C-N stretching mode at 1018 cm^{-1}, out-of-plane C-H bending mode at 843 cm^{-1}, and C-H rocking mode at 731 cm^{-1}) [160]. Peaks related to Neo are not distinguishable since most of its peaks coincide with other peaks from the polymers but also because its concentration is much lower compared to the polymer matrix [204]. On the other hand, the bottom layer was mainly characterized by the presence of both PVP and HA polymer bonding signals such as N-H stretching mode/Fermi resonance at 3101 cm^{-1}, $C=OO^-$ stretching mode at 1606 cm^{-1}, amide II at 1558 cm^{-1}, asymmetric C-O-C stretching mode/glycosidic bond at 1150 cm^{-1}, and C-OH stretching mode at 1035 cm^{-1} bands[205]. Additionally, both layers were analyzed at different depths from the surface. For the top layer, the main differences were an enlargement and shifted to lower wavenumbers of the C=O stretching mode of the PVP polymer (Figure 3.3B). For instance, at 1.80 μm depth the full width at half maximum (FWHM) and wavenumber values of this band were ~49.8 and 1657 cm^{-1}, respectively, and at 8.75 μm depth ~94.2 and 1645 cm^{-1}, respectively. Such differences are indicative of changes in the molecular interactions of C=O functional groups [162]. Most likely, there is increasing interaction between the PVP matrix and the Neo molecules, suggesting that an increasing gradient of drug concertation could occur towards the interface of the two layers. On the other hand, the analysis at different depths of the bottom layer showed significant differences related to the relative proportion of both polymers (i.e., PVP/HA as the ratio between the intensities of the C=O stretching mode of PVP and C-OH stretching mode of HA) and a shift observed for the C-OH stretching mode of the hyaluronic acid (Figure 3.3C). The PVP/HA ratio exponentially decreased from a value of ~2.8 at 1.80 μm depth to ~1.3 at 8.75 μm depth, indicating that the relative HA concentration increases with the depth. Moreover, the wavenumber of the C-OH stretching mode attributed to the hyaluronic acid shifted by 36 cm^{-1} to lower wavenumbers from 1047 cm^{-1} at 1.80 μm depth to 1011 cm^{-1} at 8.75 μm. The position of this band depends on the hydrogen bonding network of polysaccharide OH groups [205]. Hence, this shift can be

related to the perturbation of the hydrogen bonding network due to PVP that also indicates the establishment of new hydrogen bonds between the two polymers.

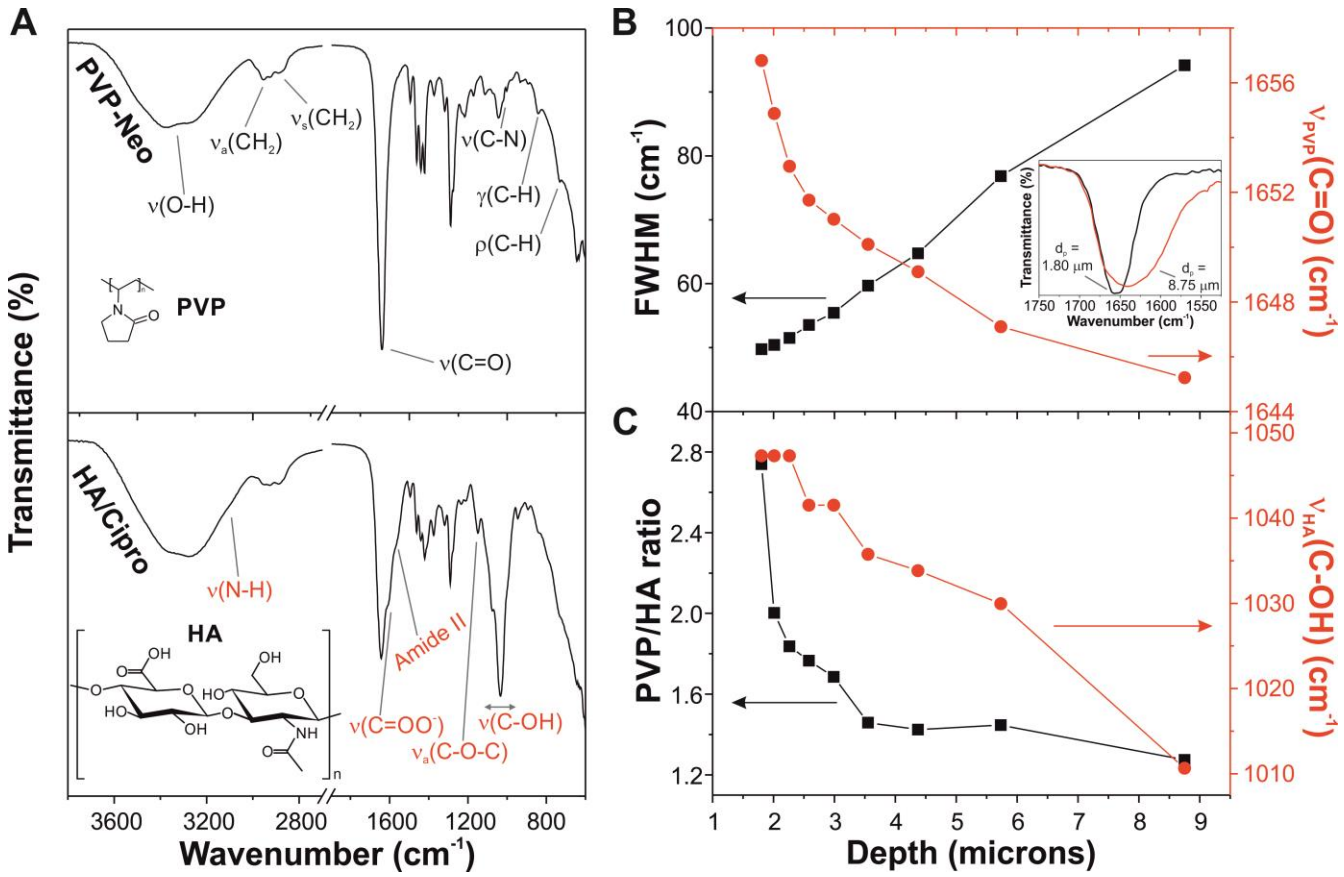

Figure 3.3 A, ATR-FTIR spectra of the bottom (wound contact) and top layers. Main peak assignments due to PVP (black) and HA (red) are shown, and their chemical structures are indicated. **B**, Enlargement (black squares) and shift (red circles) of the C=O stretching mode for the PVP/Neo layer with the depth of analysis. The inset shows a comparison of the C=O stretching mode (1750-1525 cm^{-1}) of PVP/Neo layer at different depths: 1.80 μm (black line) and 8.75 μm (red line). **C**, PVP/HA ratio (black squares) and shift (red circles) of the C-OH stretching mode for the HA/Cipro layer with the depth of analysis.

Adhesion to human skin of the bilayer films was measured with a peel test and compared to a commercial medical plaster patch with an acrylic adhesive. Photograph of the set-up for the adhesion test, described in the methods section, is reported in Figures 3.4A. Typical peel force versus displacement profiles are shown in Figure 3.4B. As seen in the figure, the adhesion force profile of the commercial patch displays a kind of tacky/non-tacky/tacky profile such that an average adhesion force of 30 N/m is needed in order to peel this section (adhesive containing section) away from the skin until the medicated section is reached. Here, the peel force falls to practically zero. Afterward, the rest of the adhesive containing patch is removed with an average force of 40 N/m. Our films, however, demonstrate an almost constant peel force profile as shown in Figure 3.4B. The whole film can be removed from the skin when an average peel force of 15 N/m is applied. Although not shown, from each adhesion profile curve, the peak adhesion strength and the average adhesion strength can be estimated [206]. Doing so, even though the adhesion strength values of the *self-adhering* bilayer films (peak 31.13±12.44 N/m, average 14.61±5.94) are about half the ones of the commercial dressing that had been modified with an acrylic adhesive (peak 58.55±7.68 N/m, average 39.96±13.55 N/m), they are of the same order of magnitude.

It should be noted that the above reported adhesion values are for moist skin and if very dry skin is used, the adhesion strength of the full bilayer film reduces to 2 N/m without the application of an adhesive. Literature data on similar 90^{o} peel tests performed with other adhesive patches on the skin, such as 3M Durapore® [206] and silicone-based transdermal matrix [207], showed values of adhesive strength between 20 and 120 N/m. Instead, hydrophilic polymer-based wound patches tested on skin models were shown to have an adhesive strength between 1 and 3 N/m [208, 209]. Therefore, the full bilayer films demonstrate satisfactory *self-adhesion* performance for both dry and moist human skin that might be associated with different levels of wound hydration/exudate. Figure 3.4C shows a photograph of the peel-tests conducted on a human arm for large bilayer film produced by the rod

coating method. Stress-strain mechanical test results of the bilayer films are shown in Figure 3.4D. The full bilayer is a ductile composite with an elastic modulus of 3.7 MPa, an elongation at maximum load of > 60%, and a tensile strength of 3.6 MPa, see the insert in Figure 3.4D. The elastic modulus is higher than that of human skin[210] but lower than most systems developed as wound dressings [211, 212].

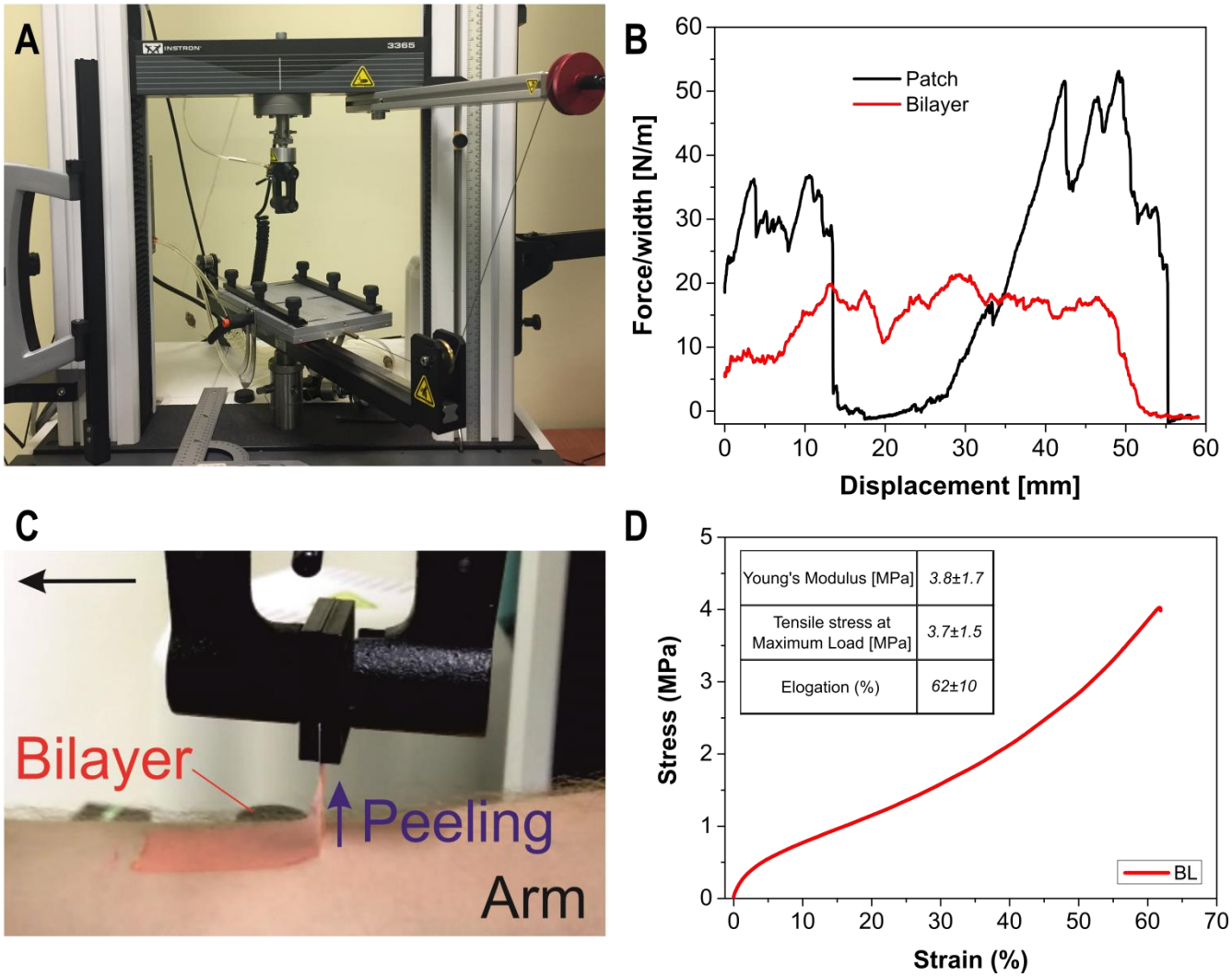

Figure 3.4 A, Photograph of the instrument used for the peel adhesion tests. **B**, Peel adhesion measurements (on a human arm) for the commercial patch adhesion (black line), and the full BL film (red line). The black arrow indicates the displacement direction. **C**, Photograph was taken during the

90^{o} peel test; the arrows indicate the displacement direction. **D**, Typical stress-strain curve of a full bilayer sample. In the insert, data of Young's modulus, tensile strength and elongation are reported.

The relatively low stiffness is expected to reduce the elastic mismatch and, therefore, improve the comfort of the dressing. The large elongation at fracture eliminates the risk of fracture of the dressing during normal body movements. Water uptake measurements revealed how the bilayer was able to absorb 40% of its weight of water at the highest level of humidity (100%). This value is in accordance with the water absorption values, between 10% and 50%, reported in the literature for several PVP and HA-based wound dressing [203, 213-215].

3.3.3 Study of drug release of Eosin and Ciprofloxacin

Drug release measurement results from the full bilayer constructs and the reference/control samples, shown in Table 3.1, are reported next. *In vitro* drug release measurements were collected from the following samples: release of Ciprofloxacin and Eosin from BL (full bilayer), release of eosin from BLN (bilayer with no Ciprofloxacin), release of Ciprofloxacin from SLHC (bottom layer only), and release of Ciprofloxacin from SLPC (bottom layer only with no HA). Figure 3.5 shows the cumulative release outcomes of the various systems analyzed over a period of 5 days. Eosin appears to have a burst-like release profile from the PVP matrix, reaching 100% of release within the first 24 hours, regardless of the presence of Ciprofloxacin in the bilayer constructs (see Figure 3.5A top panel). Inspection of Figure 3.5B (top panel) that shows the release during the first 6 hours indicates that even though a burst-like release occurs within the first 6 hours, the rate of Neo release from both BL and BLN films slows down after the first hour reaching 97% release at the end. The absence of HA (SLPC) also causes a similar burst-like Ciprofloxacin release from PVP matrix. Similar to Neo, Ciprofloxacin release from SLPC is faster within the first hour as shown in Figure 3.5B (bottom panel), and at the end of 1-hour and 6-hours periods, more Ciprofloxacin is released to the medium compared to Neo. Once

HA is introduced to the bottom layer or as it is present in the full bilayer (SLHC or BL), the release of the antibiotic slows down significantly spanning a 5-day period as shown in Figures 3.5A and 3.5B. Note that when the films are soaked in the release media, drug release rates from each layer (top or bottom) can be affected by the presence of the other.

It is acknowledged that in a more realistic application such as the release of the antiseptic from the top layer directly into a moist wound, no interference occurs due to the presence of the bottom layer. However, since the insertion of such drug loaded films in model release media is a well-accepted procedure, it is important to acknowledge such potential interferences if any. For instance, in the case of BL, additional thickness due to PVP top layer appears to slow down the antibiotic release, and this effect is more significant after the first 24 hours or so when one compares release curves in Figures 3.5A and 3.5B. From the single layer construct of SLHC, almost all the antibiotic is released after about 48 hours whereas an additional 3 days are needed to discharge the entire antibiotic from the full bilayer construct. This is somewhat surprising if one considers that the release of both drugs from a single PVP film is fast and completed after 6 hours.

Although further work and evidence may be needed, we argue that the delay in release from BL can be attributed to the interface between the top and bottom layer that might have additional interactions (i.e. hydrogen bonding) between the HA of the bottom layer and the PVP of the top layer. This can slow down erosive polymer loss of film dissolution, instead favoring diffusion based mechanism. Taken together, our results helped us define a schematic representation of the hypothetical release mechanism of Ciprofloxacin and Eosin from our bilayer constructs as depicted in Figure 3.5C. Note, however, that the herein proposed model considers the bilayer constructs placed onto a moist surface (such as a wound), with the PVP/HA layer not directly in contact with the moist zone. Initially, the Eosin in contact with the PBS is quickly released (24 hours if the zone is 100% humid) as the highly hydrophilic PVP matrix undergoes fast degradation or resorption. In the bottom layer, the Ciprofloxacin

incorporated within the PVP/HA matrix begins to diffuse outside, as a result of the PVP dissolution. Afterward, HA undergoes swelling and slower dissolution rate, hence regulating antibiotic release in a sustained manner. This model, of course, does not hold exactly if the film is fully immersed in a release medium since both layers contact the medium at once.

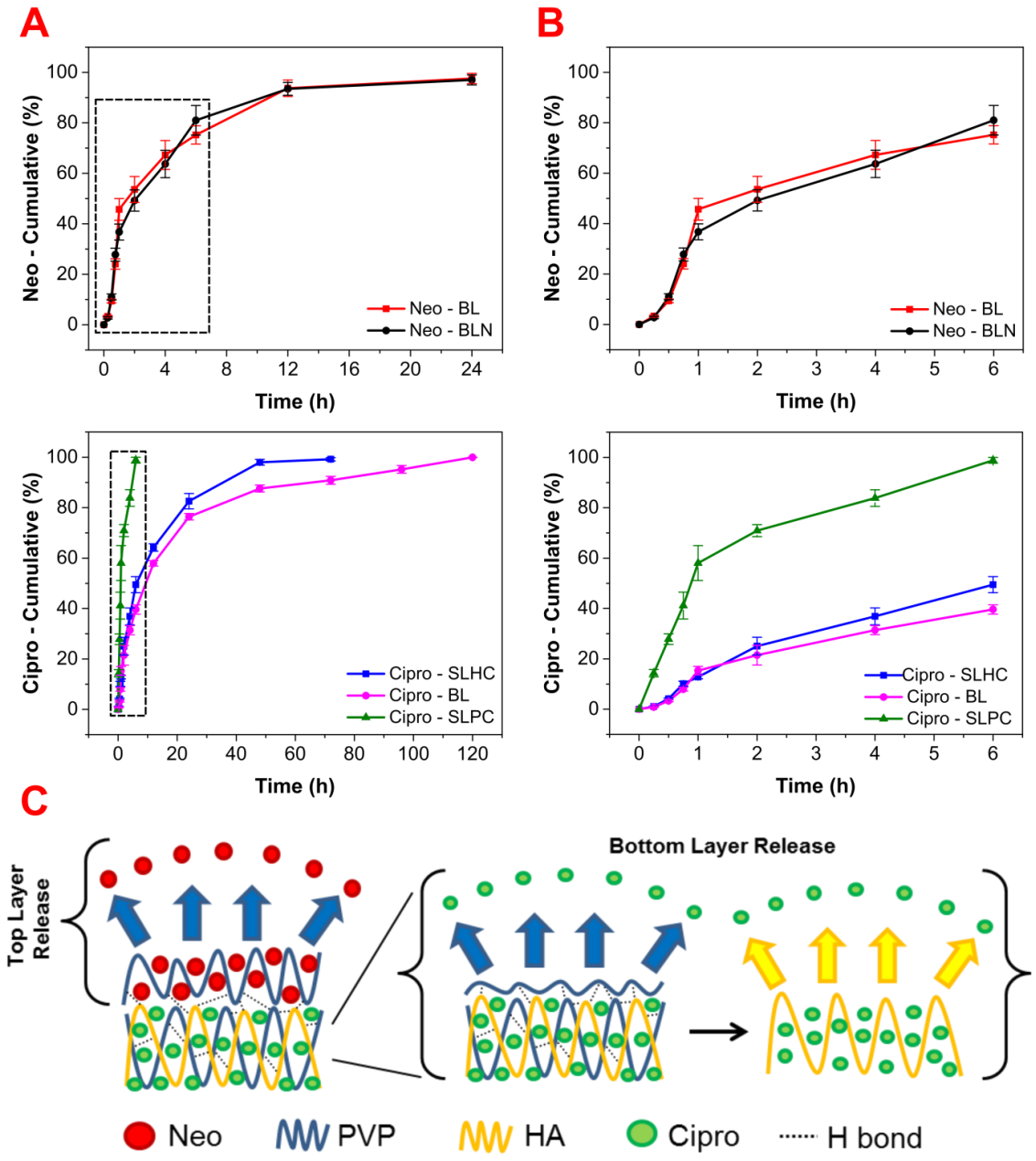

Figure 3.5 A, Release profiles of Eosin (top panels) and Ciprofloxacin (bottom panels) over a period of 24 and 120 hours, respectively. **B**, Release results of Eosin (top panels) and Ciprofloxacin (bottom

panels) for the first 6 hours. **C**, Schematic representation of the hypothetical drug release mechanism from the bilayer construct placed on a moist medium such as a wound. Potential establishment of hydrogen bonds within the top layer and at the interface between the top and bottom layers are shown as dashed lines

3.3.4 In vitro biocompatibility assay on HFF-1 cells

The biocompatibility of SLHC, BL, and BLN samples was assessed on HFF-1 cells. After 24 hours of exposure, no cytotoxic effects of the tested samples extracts were detected, as shown in Figure 4.6. No statistically significant differences ($p > 0.05$) were observed in cell survival in comparison to the control (given as 100%). According to ISO10993-5 guidelines, as the cell viability of the sample extracts were higher than 70% of the control group, all materials were considered biocompatible.

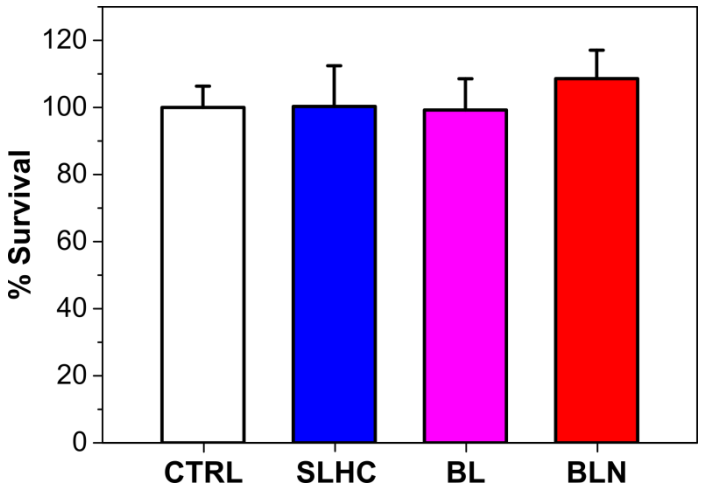

Figure 3.6 Viability of HFF-1 cells after 24 hours of exposure to the samples extraction media. Survival values are normalized with respect to the control (set to 100%). Average percentage values ± S.D. of three independent experiments, each performed in three technical replicates, are shown.

3.3.5 Hemocompatibility assay

Hemocompatibility is a necessary skill for considering biosafety a material. Blood was incubated with bilayer of different weights (4 and 6 mg) for 3 hours, and the hemolysis ratio was analyzed by

measuring the amount of free plasma hemoglobin (Hb). As shown in Figure 3.7A, the hemolysis percentage induced by the presence of the bilayer in the blood sample was comparable to the untreated control, whereas whole hemolysis was observable in the Triton-X control sample. The result was confirmed by the erythrocytes microscopic observation (Figure 3.7B).

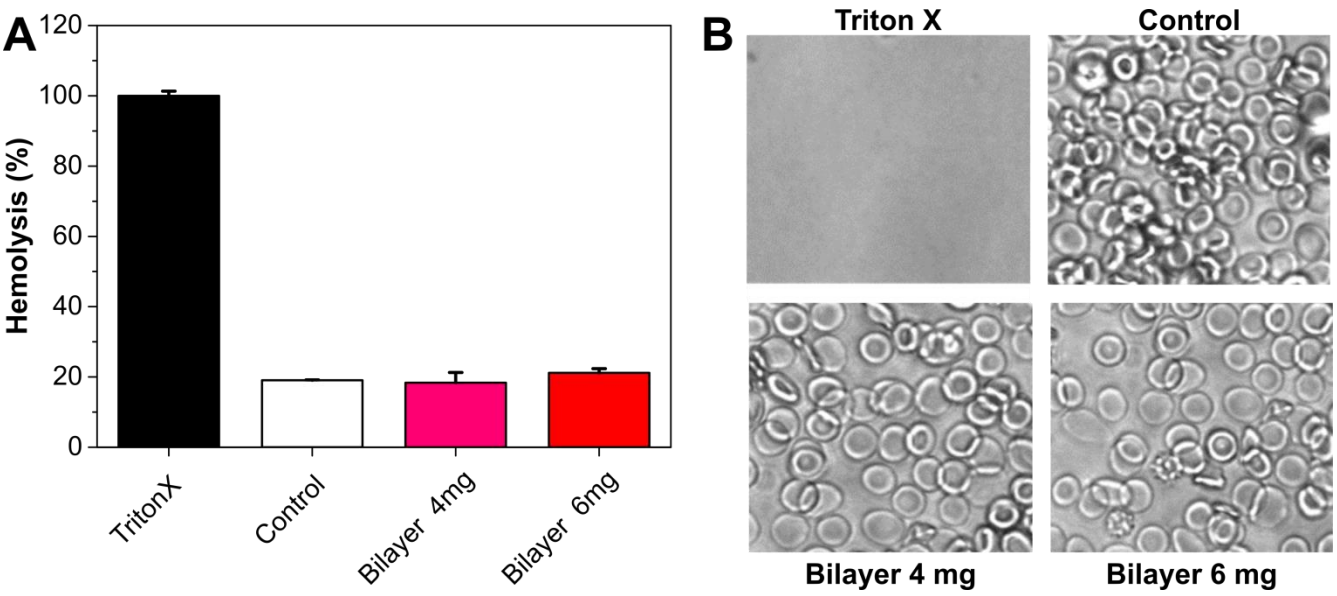

Figure 3.7 A, Histogram relative to the absorbance of released Hb after treatment with 4 and 6 mg of bilayer films. The values are expressed as % respect to the positive control (TritonX). **B**, Optical images of erythrocytes after the treatment with Triton X, medium, 4 mg and 6 mg of Bilayer, respectively.

3.3.6 In vitro anti-inflammatory properties

The inflammatory response was measured both by IL-6 and TNFα production, two anti-inflammation mediators. PBMCs were stimulated with LPS in the presence or not of the bilayer-drug, and the images are shown in Figure 3.8A. In particular, LPS activation caused the formation of cell clusters an effect inhibited by the presence of the bilayer-drug. In the agreement, the result obtained by ELISA test

indicated that after LPS stimulation, PBMCs increased both IL-6 and TNFα levels, whereas in presence of the bilayer-drug, a reduction of cytokines levels was detected (Figures 3.8B and C) indicating that the material has anti-inflammatory properties.

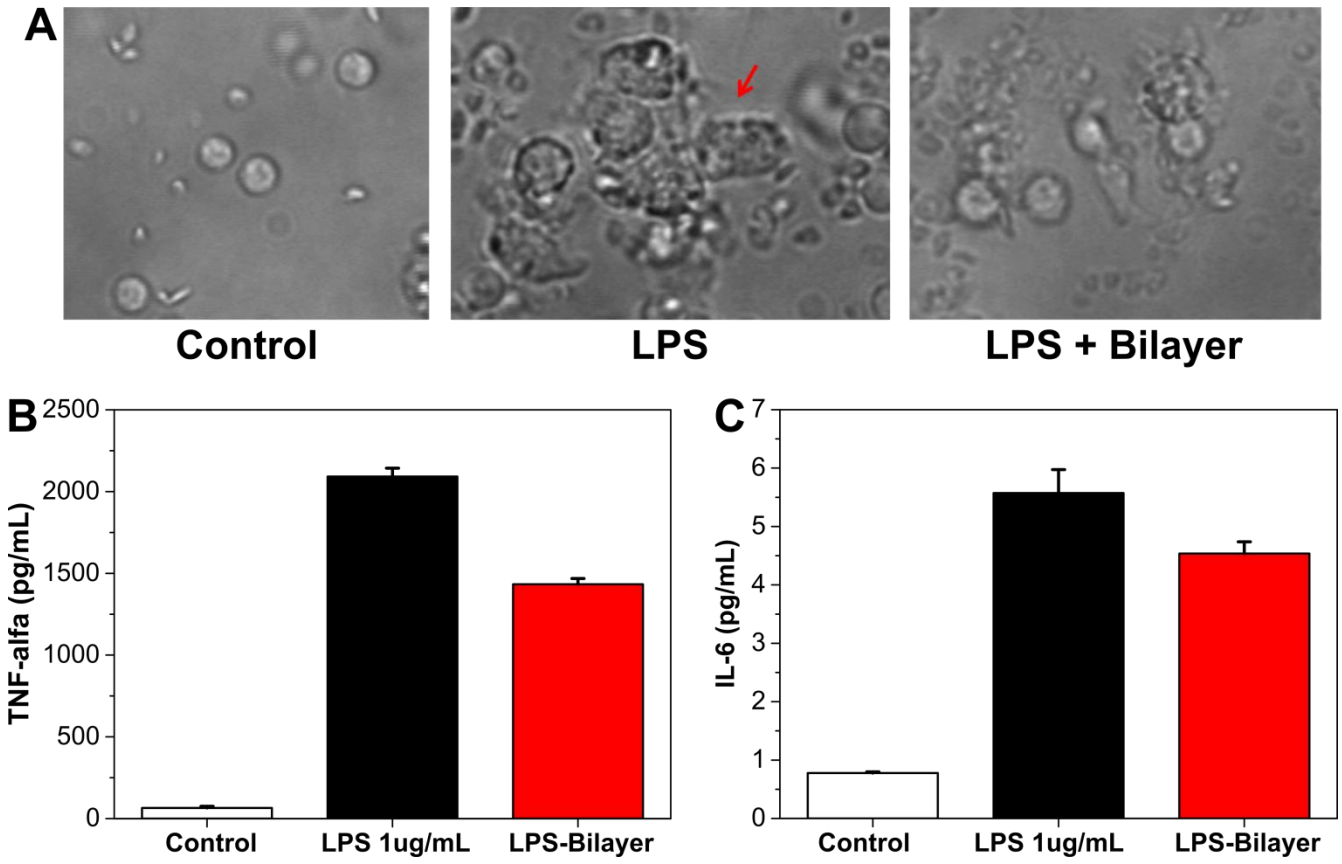

Figure 3.8 A, Optical images of control samples of PBMC cells, PBMCs and LPS, and PBMC, LPS and bilayer, respectively. The red arrow indicates the clusters caused by the LPS presence. **B**, **C**, Histogram of the level of TNF-α and IL-6 quantified by ELISA and expressed in the control samples of PBMC cells, PBMCs and LPS, and PBMC, LPS, and bilayer.

3.3.7 Antibacterial properties of the designed bilayer

The BL bactericidal activity, against the representative Gram-positive (*S. aureus)* and Gram-negative (*E. coli and P. aeruginosa*) microorganisms, was assessed by disk diffusion assay. BL produced a zone

of inhibition of 30.6 (± 1.9) mm in *S. aureus* and 42.9 (± 3.2) and 39.5 (± 2.0) mm in *E. coli* and *P. aeruginosa*, respectively, confirming its antibacterial properties (Figures 3.9 B, D, F).

On the contrary, the polymer dressing, used as negative control, showed no inhibition of the bacterial growth (Figures 3.9 A, C, E). In order to assess the pharmacodynamics of the antimicrobial agents present in the bilayer constructs, time-kill kinetics tests were performed against *S. aureus*, and results are shown in Figure 3.7G. The normal growth rate was represented by the growth control (CTRL) and SLHP dressing, which contained no antimicrobials. The kinetic profile of BLN was similar to the CTRL, while SLHC and BL displayed bactericidal activity, showing a ≥ 3 log10 reduction in viable cell count compared to the CTRL inoculum starting from 3 hour exposure. Interestingly, after 6 hour of treatment, BL induced significantly higher cell death compared to SLHC. This could be correlated to the drug release profile previously presented (Figure 3.5). Since at 6 hours a release of 75% Eosin and 39% Ciprofloxacin was observed, the simultaneous availability of such antimicrobials amount might account for the more effective bacterial killing (0.83 log10).

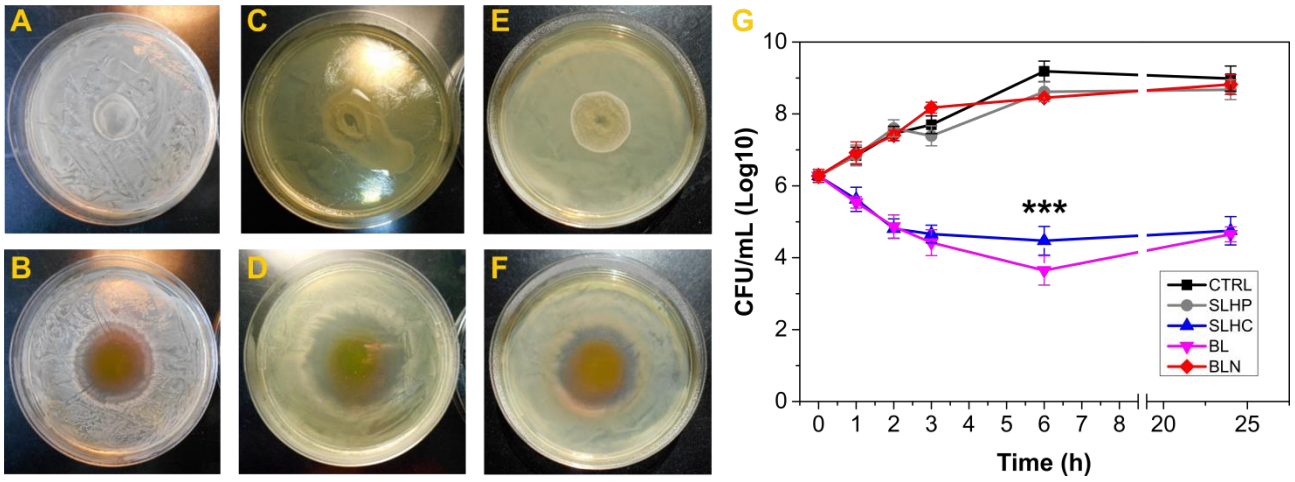

Figure 3.9 *In vitro* evaluation of antimicrobial activity. Agar disk diffusion method: BL was tested against *S. aureus* (**B**), *E. coli* (**D**) and *P. aeruginosa* (**F**). SLHP was used as negative control in both microorganisms (**A**, **C**, **E**, respectively). Time-kill kinetics is showing Log reduction against *S. aureus* (**G**). Data are the mean from two independent time-kill experiments. ($p < 0.0001$ vs SLHC).

3.3.8 In vivo resorption, anti-inflammatory response and wound closure of bilayer

The *in vivo* bio-resorption and biocompatibility of bilayer films were evaluated in a full-thickness excisional wound healing mice model [171]. The material was applied to fresh wounds and monitored for 48 hours (Figure 3.10A). After the patch application, no visible negative effects (e.g. no color change or wound erosion) were noticed. The full bilayer construct showed an initial slow, regular tendency in exudate absorption and film degradation. After 2 hours, the patches started to absorb a high quantity of exudate and were swollen. The swelling process led to a more intense and visible release of eosin, which continued for the following 6 hours. In the first 24 hours, more than 50% of the starting material was reabsorbed (Figure 3.10B). More importantly, the films appeared to have a regular and reproducible behavior in all 5 mice used for the experiment. It can be concluded that the developed bilayer constructs can be safely applied in model animal studies and do not produce any visible irritation effects.

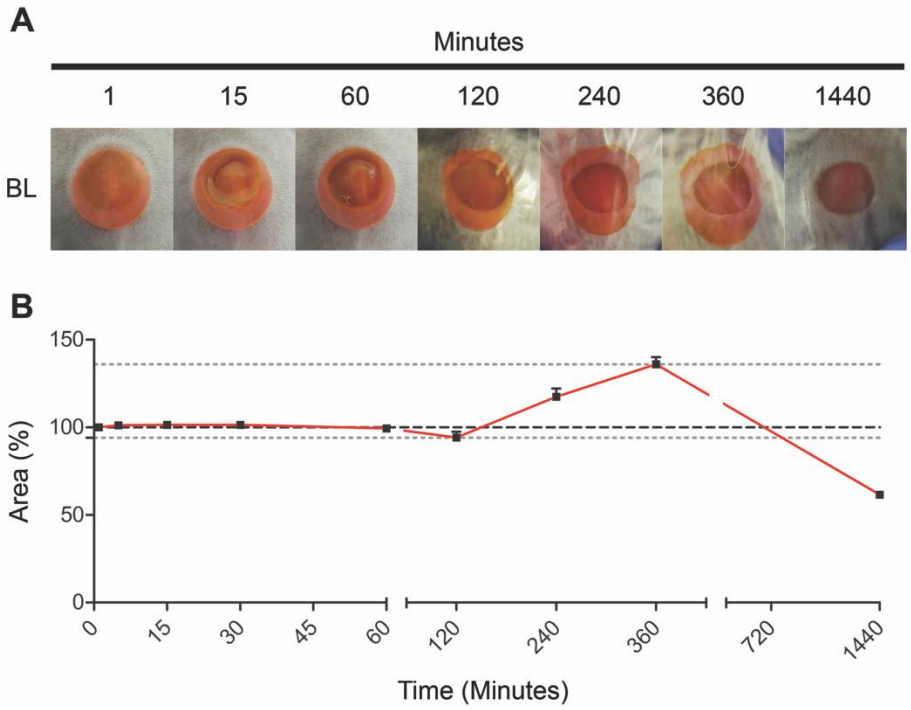

Figure 3.10 *In vivo* wound healing mice model. (**A**) The sequence of representative photographs displaying the wound treated with the bilayer film. (**B**) Profiles of the estimated resorbed membrane percentage as a function of time.

Cutaneous levels of TNF-α and IL-1β were analyzed after 48 h from wound induction and, as expected, naive animals expressed a low level of both cytokines, indicating that no inflammation was present. On the contrary, a significant increase of TNF-α and IL-1β was observed in wounded/sham animals. Instead, in the mice treated with the bilayer dressing a reduction of 70% for TNF-α and 74% for IL-1β respect to the wounded/sham levels was observed, Figures 3.11A and B. These results highlighted and confirmed an important role of Bilayer in the modulation and reduction of the inflammatory response.

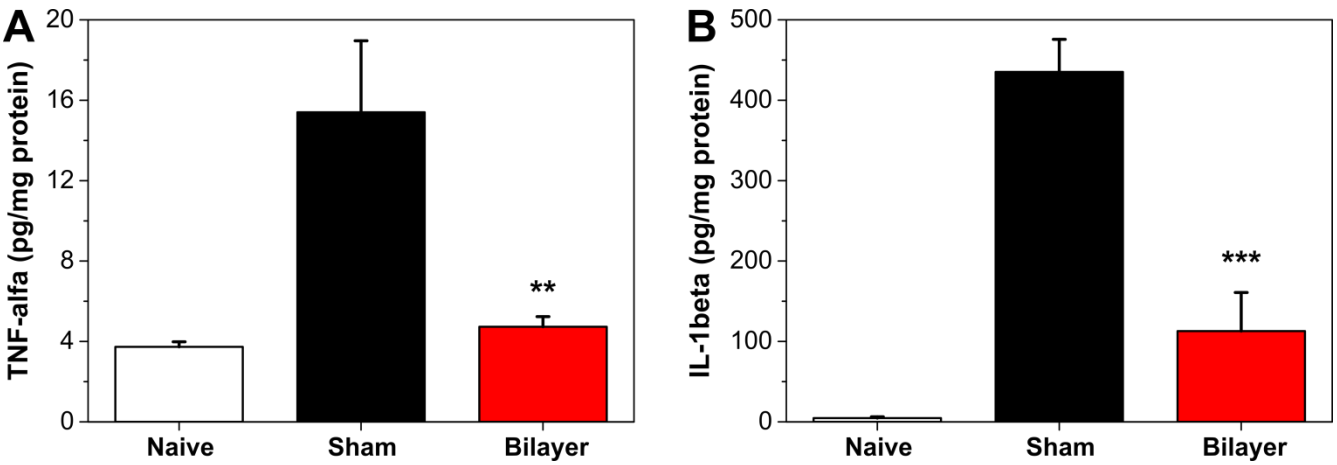

Figure 3.11 *In vivo* evaluation of TNF-α (**A**) and IL-1β (**B**) after 48 hours from wound induction. ***p < 0.01* vs to the wound untreated group; *** *p < 0.001* vs to the wound untreated group.

Finally, the capacity of the bilayer construct to accelerate the healing process was investigated in a full-thickness excisional wound healing mice model, and the main results are reported in Figures 3.12A and B. As can be noticed in the graph, Figure 3.12B, bilayer materials were able to reduce statistically ($p < 0.05$) the wound area respect to the control starting from day 5. Furthermore, the wound closure was obtained in only 12 days for mice treated with the bilayer, suggesting faster and more effective healing in these animals.

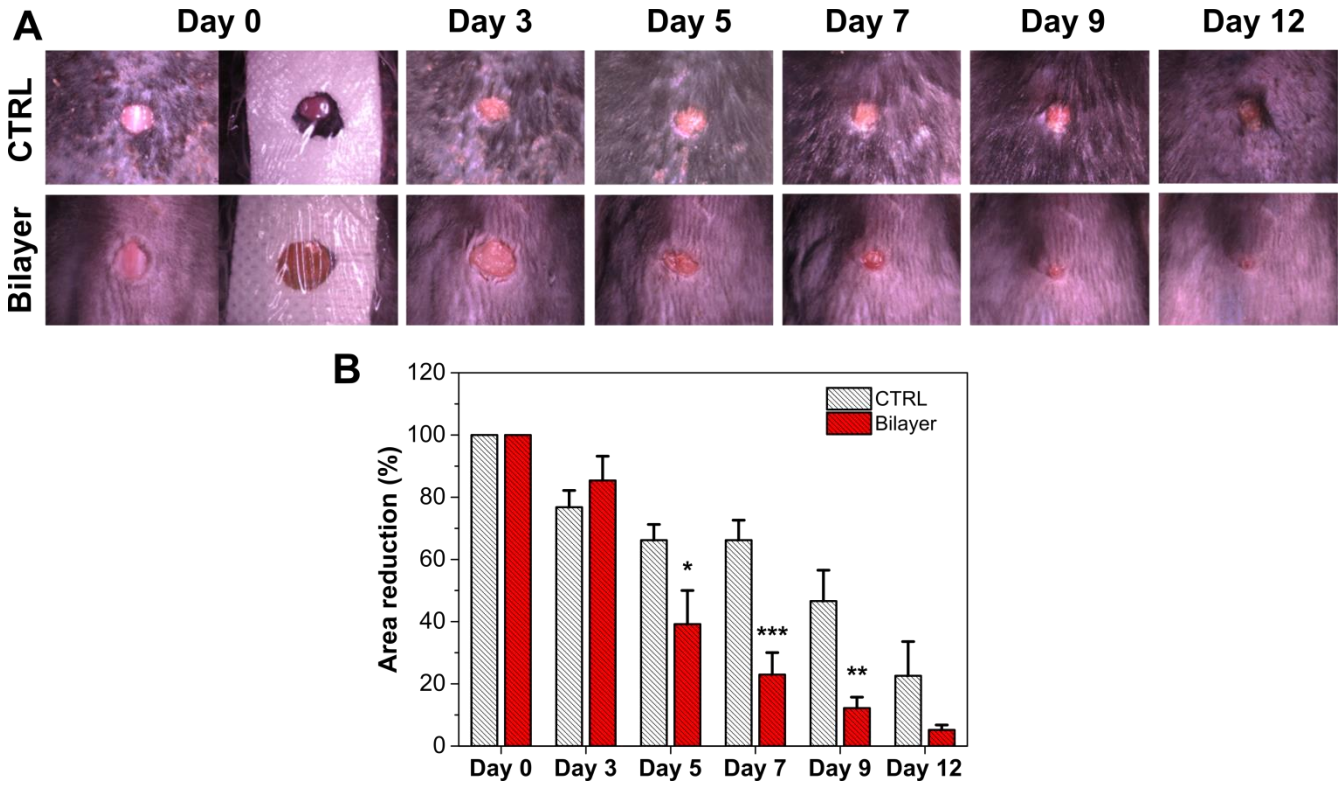

Figure 3.12 A, Representative photographs of the skin of wound healing mice at different time points (day 0, day 3, day 7, day 9, and day 12): untreated (no dressing) and bilayer dressing treated wounds are shown. **B**, Time-course (days) of wound healing in mice untreated (white bars), and treated with the Bilayer (red bars). *$p < .05$, **$p < 0.01$ and ***$p < .001$, compared to untreated mice.

3.4 Conclusions

In this chapter, facile processes to design transparent bilayer drug releasing constructs that can be suitable for skin wound treatment were demonstrated. Two eco-friendly waterborne fabrication processes, namely, rod coating for large size samples and spin coating for smaller samples depending on the targeted wound size were used. The top PVP stratum is able to ensure a good initial adhesion to the skin and fast release of the cutaneous antiseptic Neo. In the top layer, HA in tandem with PVP ensured a more sustained release of the antibiotic, Cipro, which could potentially help in keeping an aseptic wound bed during the later stages of the healing process. PVP acted as an excellent transparent matrix for HA. In both layers, glycerol was used as a plasticizer. Peel adhesion tests revealed self-adhering behavior to both moist and the dry human arm skin surface. Drug release experiments revealed that HA controls the release of Ciprofloxacin from the PVP matrix. Bilayer resulted biocompatibility, hemocompatibility, and capable to reduce the level of inflammatory mediators *in vitro*. The antibacterial properties of the bilayer were demonstrated against *S. aureus*, *E. coli*, and *P. aeruginosa*. The preliminary *in vivo* mice full-thickness wound model experiment confirmed the efficient resorption of our bilayer construct, while no complications or toxic effects on the wound was observed. Finally, the reduction of the pro-inflammatory mediators TNF-α and IL-1β and acceleration of wound healing process were highlighted in the mice treated with our promise bilayer wound dressing.

Chapter 4 : Testing of PVP Cipro wound dressings on an infected-wound model based on *ex-vivo* human skin

4.1 Biofilms and 3D infected wound human skin model

Infections of the post-operative and chronic wound are becoming a concern, considering the increasing median age of the population and age-associated immune deficiency [216]. Related associated diseases, like diabetes mellitus or venous insufficiency, and immobility are the major conditions leading to chronic wounds. Moreover, in immune suppressed patients, wounds are particularly prone to infections, which in turn can favor and maintain the chronic inflammatory status of the wound. It is now recognized that chronic wounds are often associated with microbial biofilms, i.e. organized communities of one or several microorganism species encased and shielded by extracellular polymeric substances (EPS) [217, 218]. It has been demonstrated that bacteria in the biofilm are more resistant than planktonic bacteria and that significantly higher concentrations of antibiotics are needed to treat biofilm infections [55, 56]. Thus, to prevent or treat biofilm infections it is very important to realize high and sustained concentrations of antimicrobials at the site of infection. This is often a significant limitation for new potential antimicrobial drugs and is due to unfavorable drug properties like stability, solubility, biodistribution. Different innovative pharmaceutical formulations, like nanoparticles, microneedles, nanofibers, have been developed to improve systemic as well as local drug delivery and targeting [61, 125, 219].

Equally important is to define the right model to simulate and test these new pharmaceutical devices. In literature, there are different *in vitro* and *in vivo* models to investigate antimicrobial formulations. Whereas *in vitro* mono and multicellular set-ups are limited to their 2D structure, *in vivo* animal models offers diverse advantages including three-dimensional tissue scaffold and systemic compartment. Nevertheless, besides the fact that the results of animal studies are not always reproducible in humans, the animal number in research should be limited. As an alternative to *in vivo* animal models, *ex vivo* models have been proposed. *Ex vivo* skin has been used for years to test skin penetration of chemicals and drugs [220].

In the last years, several groups have developed 3D infection models based on *ex vivo* porcine or human skin [130, 221-225]. Even if it is easier to obtain *ex vivo* animal skin than retrieve *ex vivo* human skin, animal skin has different cell biology, histology, and immunology than human skin. Human full-thickness skin explants represent not only 3D scaffolds where bacteria can grow up but also represent a complex environment with extracellular enzymatic activity, antimicrobial peptides, and several different cell populations including active immune cells. Thus, 3D human skin models of wound infections are ideal animal-free systems to investigate both antimicrobial activity and the interaction between bacteria and skin immune system [225].

Wound dressings loaded with Cipro could be characterized by this kind of *ex vivo* infected human skin model. Indeed, Cipro is an interesting model compound to test not only because it is poorly water-soluble, and it can be detected by fluorescence spectroscopy but also because it was reported to inhibit quorum sensing in *P. aeruginosa* at sub-MIC concentrations leading to inhibition of the virulence of these bacteria even though they cannot inhibit their growth at concentrations obtainable *in vivo* [226].

In this chapter, the drug delivery property, toxicity, and efficacy of PVP-Cipro films and nanofibers were further investigated by using a wound model based on human *ex vivo* skin.

4.2 Material and Methods

4.2.1 Preparation of ciprofloxacin-loaded PVP foils and nanofiber mats

Transparent films and nanofibers mats were prepared as described by Contardi *et al.* Briefly, films were produced by using the solvent casting method starting from aqueous solutions of PVP 3% (w/v), Cipro and acetic acid 30% (v/v). In this study, three different initial quantity of Cipro 1.2, 30 and 60 mg, were combined with the polymer and the acid in water solutions with a final volume of 30 mL. The solutions were cast on Petri dishes (diameter 8.75 cm) for 3 days under an aspirated hood under

ambient conditions (16–20 °C and 40–50% R.H.). Then, the films were placed in a vacuum desiccator for 3 more days for complete removal of excess acetic acid.

The nanofibers mats were fabricated by using a vertical electrospinning set-up. Starting solutions of PVP, acetic acid 30% (v/v) and Cipro with a final volume of 6.2 mL were produced. A higher concentration of 25% (w/v) of the polymer was used to allow the electrospinning process. Similarly to the films, three different concentration of Cipro (2.2, 44 and 88 mM) were taken into account. Syringes with a stainless-steel 18-gauge needle were stuffed with the three different solutions and connected to a syringe pump (NE-1000, New Era Pump Systems, Inc.) working at a constant flow rate of 500 μL/h. The needle was clamped to the positive electrode of a high-voltage power supply generating 25/26 kV, and at 24 cm of distance from an aluminum disk was used as a collector (diameter of 8.75 cm). from each solution only 2 mL were electrospun in order to obtain the same quantity of Cipro in a circular area of ~201 mm^2 (diameter 8 mm) both for films and nanofibers.

4.2.2 Skin samples and application of superficial wounds

Abdominal skin was obtained after informed consent from healthy donors undergoing plastic surgery, see Figure 4.1 point 1. The study was conducted according to the declaration of the Helsinki guidelines and after approval by the Ethics Committee of the Charité – Universitätsmedizin Berlin (approval EA1/135/06, renewed on January 2017). Subcutaneous fat tissue was partially removed keeping a layer of approximately 5 mm and skin pieces (1.5 x 1.5 cm) were stretched and fixed on a Styrofoam block using needles (Figure 4.1 point 2-3). The surface of the *ex vivo* skin (free of injuries or redness) was cleaned with double distilled water (ddH_20). The epidermis was then removed with a rotating ball-shaped milling cutter of 6 mm (No. 28725, Proxxon, Föhren, Germany) at 16,000 rpm, which was mounted on a dental micro motor handpiece (Marathon N7, TPC Advanced Technology, Inc. Diamond Bar, CA, USA) to induce a superficial wound of approximately 5 mm in diameter (Figure 3.1 point 4) [130].

4.2.3 Drug penetration kinetics

Using a punch biopsy cutter, discs of 8 mm in diameter of foils as well as nanofiber mats were cut out and applied on the top of the wounds. Both foils and nanofiber mats were loaded with approximately 250 µg of ciprofloxacin. Samples were incubated at 37°C in a humidity chamber for different time points, after that non-penetrated material was removed with a paper towel, and the treated wound was removed from the rest of the tissue by means of an 8 mm punch biopsy tool. The tissue was chopped in small pieces and placed in 2 mL-tubes filled with 1.5 mL of 0.1 N HCl to extract ciprofloxacin. The samples were gently mixed on a shaker for 24 h at room temperature. Then, samples were centrifuged for 2 min at 300 x g, 3 x 100 µL of supernatant were removed and placed in three wells of a 96-well plate. Ciprofloxacin fluorescence (excitation wavelength: 275 nm, emission wavelength: 480 nm) was measured with an EnSpire® Multimode plate reader (Perkin Elmer, Ohio, USA). A standard curve was prepared by dissolving ciprofloxacin in 0.1 N HCl and preparing dilutions in the range between 0.5 and 10 µg/mL. The amount of penetrated drug was calculated on the basis of the standard curve. Results are presented as the means and standard deviations of three independent experiments.

4.2.4 Toxicity of ciprofloxacin-loaded PVP foil on ex vivo skin wounds

PVP foils, controls and 50 µg/cm^2 of silver nanoparticles (AgNP), as a positive control, were applied on the top of the wound. Samples and controls were incubated in 6-well pates for 20h in 2 mL RPMI-1640 medium without phenol red supplemented with 10% FCS, 100 µg/ml streptomycin, and 100 I.E./ml penicillin. After that, the old medium was replaced with fresh medium added with XTT (Roche, Germany). After 4h, 3 x 100 µl from each sample and control were removed, placed in a 96-well microplate and optical density at 450 nm and 650 nm was read with the plate reader. Absorption at 650 nm was subtracted, and the averages of the three values were calculated. Results are presented as a percentage with respect to the values of control wounds where 20 µL of a 0.9 % NaCl solution was added. Averages and standard deviation of values from three independent experiments are reported.

4.2.5 Bacteria inoculation and characterization of the PAO1 wound infection

An overnight culture of the *P. aeruginosa* strain PAO1 (ATCC 15692) was diluted with tryptic soy broth. A total volume of 5 µL (containing $1x10^7$ bacteria) of this suspension was injected with a 10 µL syringe (26 gauge) with tapered tip (#002000, SGE Analytical Science, Ringwood Victoria, Australia) from the edge of the wound into the dermis (Figure 4.1 point 5). As a control, 5 µL sterile saline (0.9% NaCl) was injected in an uninfected control wound. Wound samples were incubated in a humidified chamber at 37°C for 20 h (Figure 4.1 point 6). 8 mm biopsies were taken and fixed in a solution of 4% formaldehyde and 0.5% glutaraldehyde (in 50 mM HEPES) for 48 hours at room temperature. Skin samples were then washed in 50 mM HEPES, and dehydrated in 30, 50, 70, 90, 95, 100, and 100% ethanol. For light microscopy (and transmission electron microscopy, not shown) samples were infiltrated first with a LR White/ethanol solution (1:1, 10 min.) and then with pure LR White (2 x 15 min). Successively, samples were transferred to polyallomer centrifuge tubes (5 x 20 mm, No.342630, Beckman Coulter, Inc. Brea, CA, USA), containing LR White with the accelerator (5 µL/mL monomer). The centrifugation tubes were capped with gelatin capsule, and sample was let polymerize for 1 hour on ice and then at 60°C overnight. Five hundred nanometer sections were cut at the ultramicrotome ((EM UC7, Leica, Wetzlar, Germany), mounted on poly-L-lysine slides and incubated for 10 min on a 80°C thermo-plate. Sections were stained for 4 min with Richardson's stain, then washed with ddH2O, and imaged in the microscope (Axiophot, Carl Zeiss Microscopy GmbH, Germany). For SEM, after fixation one of the sample duplicates was cut with a scalpel in order to reveal the skin profile. The samples were then dehydrated as described above, critical point dried, mounted on aluminum stubs, sputter-coated with a 12 nm layer of gold-palladium and finally examined with a SEM (ZEISS 1530 Gemini, Carl Zeiss Microscopy GmbH, Germany) operating at 3 kV using the in-lens electron detector. Images have been cropped, adjusted for optimal brightness and contrast using Photoshop Lightroom (Adobe Systems, San Jose, CA, USA).

4.2.6 Antimicrobial activity of ciprofloxacin-loaded foils and nanofiber mats

Each tested setting was done in triplicates with a total of at least three runs. The treatments with PVP foils and nanofiber mats were started either 1 h or 20 h after bacterial inoculation. An 8 mm punch biopsy was used to collect the wound tissue including some of the surrounding intact skin (Figure 3.1 point 7). The tissue was placed in a 1.5 mL microcentrifuge tube containing 0.2 mL saline and homogenized for 3 min with a sterile steel pistil at 150 rpm mounted on a digital overhead stirrer (DSL, VELP Scientifica Srl, Usmate, MB, Italy) (Figure 4.1 point 8). After that, samples were sonicated for 10 min in an ultrasonic bath (BactoSonic1, Bandelin, Berlin, Germany) at 40 kHz using 200 Weff to detach the bacteria. 100 µL of each sample were transferred to the wells of 96 well microplates, and diluted in 1:10 steps (20 µL sample + 180 µL saline) by using a multichannel pipette (Figure 4.1 points 9-10). 5 µL of each well was plated on square tryptic soy agar plates. After incubation overnight at 37 °C, spotting areas with 5 to 50 CFU were counted (Figure 4.1 points 11-12). Mean values of the triplicate were calculated, and the bacteria number per wound was calculated according to the used dilutions. In the diagrams bacteria, counts per wound are presented as the mean and standard deviation of three independent experiments.

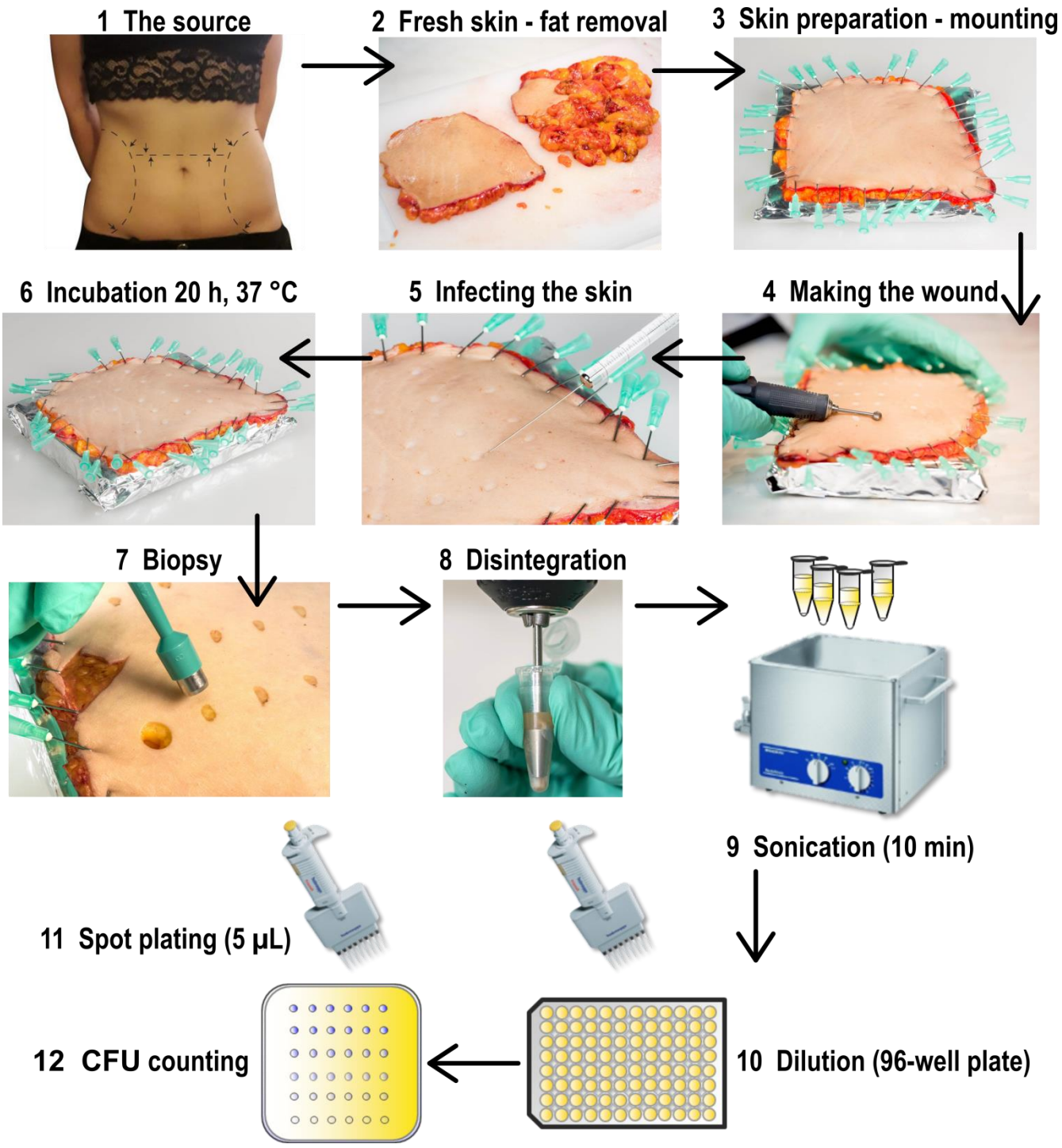

Figure 4.1 Schematic representation of the human skin *ex-vivo* infected wound model.

4.3 Results and Discussion

4.3.1 Preparation and characterization of foils and nanofibers

Starting from aqueous solutions of PVP, acetic acid and Cipro at different concentrations, transparent films and nanofibers were fabricated by using solvent casting method and electrospinning, respectively, as described in Figure 3.2. The final dry transparent films had a thickness of 150-180 μm and the absence of crystals formation was verified by SEM and opacity analysis, see Figure 2.1C and D. Moreover, as recently demonstrated, PVP-based films resulted in suitable wound dressings due to their flexibility, adhesion and resorption properties. The obtained nanofibers did not show defects or beads, as can be noted in Figure 2.2, with an average diameter of 400 nm.

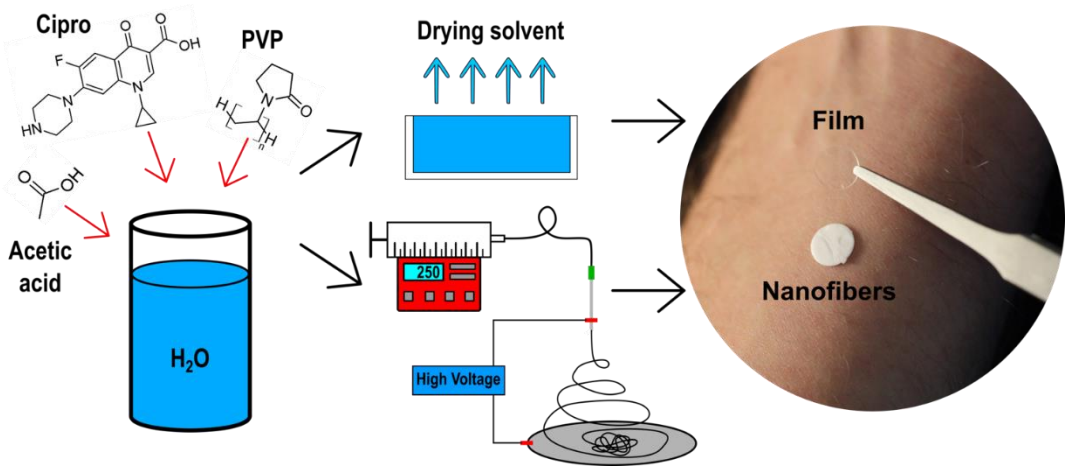

Figure 4.2 Schematic representation of the films and nanofibers fabrication.

4.3.2 Different drug penetration kinetics were measured after topical application of ciprofloxacin-loaded foils and nanofiber mats on ex vivo wounds

Foils and nanofibers mats (discs of 8 mm diameter) were applied on the top of the wounds created on the *ex vivo* skin to have a topically applied drug concentration of approximately 250 µg/wound. After different incubation times, the drug penetrated in the wound was extracted in 0.1 N HCl and measured by means of a fluorescence microplate reader (Figures 4.3 A and B). Amounts ranging between 6 and 18 µg of ciprofloxacin were detected in wound extracts. Such concentrations could be maintained for 24h in the case of foils and between 4 and 24h for nanofibers. Similar drug penetration profiles, with an initial increase of drug concentration in the wound followed by a decrease due to diffusion to the surrounding tissue, were observed for both foils and nanofibers. Both penetration kinetics could be well fitted to a second-degree polynomial trend line. However, lower amounts of Cipro were detected in the wounds treated with the nanofibers than those treated with foils. In addition, whereas foils delivered very quickly high amounts of ciprofloxacin (approximately 12 µg after only 2 h), the nanofibers reached similar concentrations later, after 6h. Interestingly, foils could maintain for over 24h a drug concentration in the wound between 12 and 18 µg, reaching the maximal concentration after 16h. For nanofiber mats, the maximal drug amounts in the wound were found already after 6 h, were maintain for other 10 hours of incubation and decreased to lower concentration after 24h. In a previous study, we have investigated the dissolution rate of both materials in phosphate buffer and on a mice full thickness wound model [203]. Results showed that nanofibers dissolve very quickly, within the first two hours, whereas foils took longer.

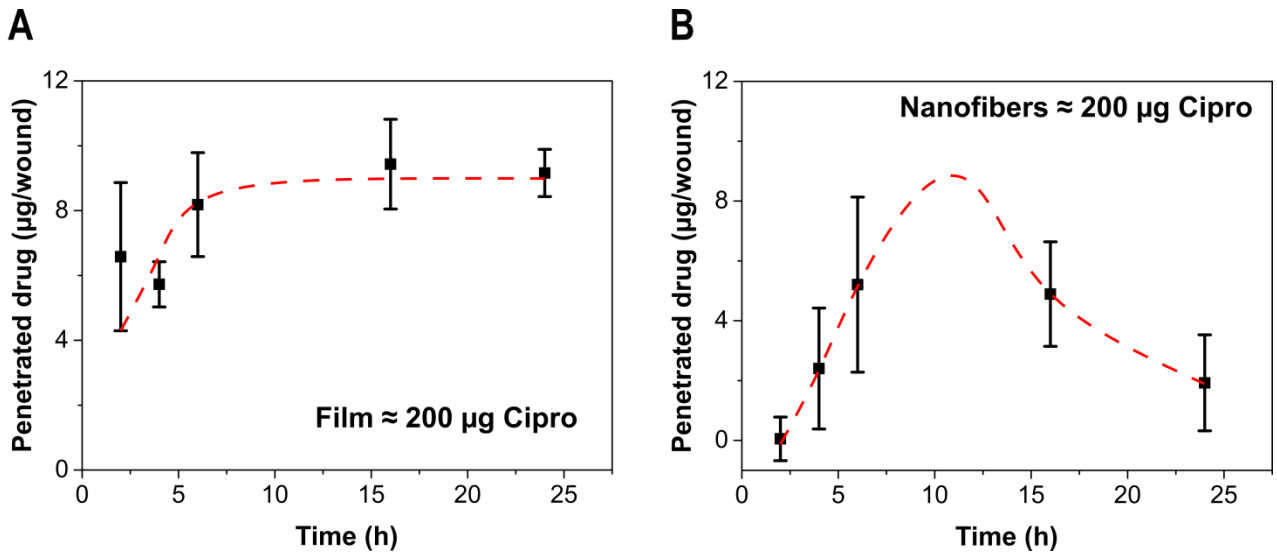

Figure 4.3 A, **B**, Penetration of ciprofloxacin into wounds after topical application of ciprofloxacin- loaded foils and nanofibers, respectively. Wounds of approximately 5 mm in diameter were produced in skin explants of 1.5x1.5 cm by removing superficial skin layers using a milling cutter. A 8 mm disc, corresponding to a dose of approximately 250 µg ciprofloxacin, was applied on the top of the wound and skin samples were incubated at 37°C for 2, 4, 6, 16, and 24 hours. A biopsy of tissue was taken chopped into small pieces and extracted in 1 N HCl. Ciprofloxacin fluorescence in extracts was measured and drug concentrations were calculated using a standard curve. n=3.

This means that once applied on the wound, nanofibers release almost all loaded drug within the first incubation hours. This might result in a high local concentration whereby precipitation or crystallization can occur and hinder drug penetration. On the contrary, foils dissolved over a prolonged time of 6-8 h and released small amounts of the drug. In this way, crystallization is avoided and the free drug can penetrate in the wound. The fact that foils dissolve slower may also have the advantage of reducing skin water loss. This has a hydrating effect and might positively influence drug penetration. Another important aspect that should be mentioned is that, due to the spinning process, the amount of polymer and drug in the nanofiber mats may vary from batch to batch and even in different areas of the

same mat. These means that the amount of applied drug may vary from sample to sample. To avoid this problem, we waited for foils and nanofiber mats before application. We found that the weight deviation from disc to disc varied more for nanofiber mats than for foils. However, this had only a small influence on the amounts of the penetrated drug.

In summary, drug penetration experiment using the 3D wound model showed that foils can deliver high amounts of Cipro very quickly and maintain the reached concentration over 24 hours. Such kinetics are desirable especially when wound are infected by bacterial biofilms, which are usually sensible only to high concentrations of antibiotics. In addition, high and sustained drug concentrations are necessary for eradication of all bacteria and avoid inducing bacterial resistance.

4.3.3 Ciprofloxacin-loaded foils and nanofiber mats are not toxic toward cells of the ex vivo skin model

Next, we used the 3D wound model to test if the used materials and drug concentrations are toxic to skin cells once applied on the top of the wound. For these experiments, after the creation of the wounds, the tissue blocks were placed in RPMI 1640 medium at the air-liquid interface previous application of the tested material. After 20h of incubation, XTT was added, and the absorption of the reduced metabolite was measured after 4 hours. Many cells in skin explants were still metabolic active, and an evident formation of the red formazan product was observed.

Wounds treated with isotonic sodium chloride solution served as negative control, whereas silver nanoparticles which can release toxic silver ions served as positive controls (Figure 4.4). PVP-foils did not show any toxicity. This was somehow expected to be PVP a well-tolerated, FDA approved polymer used as a binder in tablets, as a food additive, and also as plasma volume expander [227]. Foils prepared to dissolve PVP in 30% acetic acid resulted to have no effect on skin viability. The tested foils

contain only residual amounts of acetic acid molecules incorporated within the PVP polymers, being most of the solvent evaporated during the preparation process, as described in the section 2.3.2 on the quantification of residual acetic acid.

Finally, also the PVP foils loaded with the three concentrations of ciprofloxacin resulted to have no influence on the viability of skin cells. Previous studies have shown that ciprofloxacin has toxic effects on fibroblasts [228] and keratinocytes [229].

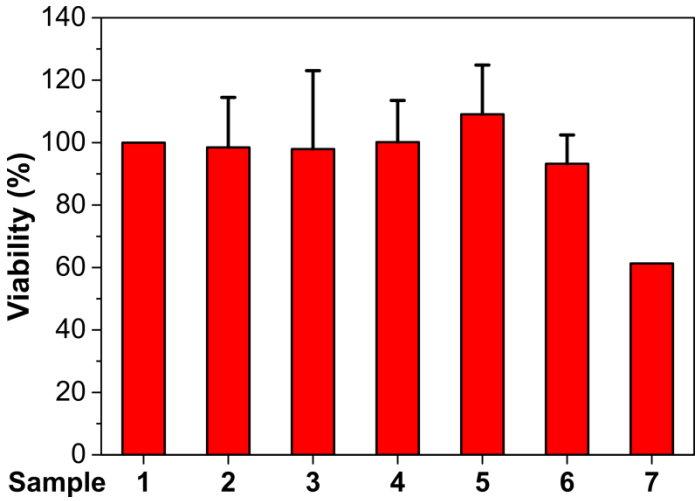

Figure 4.4 Toxicity of foils towards skin tissue. The XTT assay was run with skin biopsy previously treated with: (1) 0.9% NaCl; (2) PVP foils prepared from solutions in ddH_2O; (3) PVP foils prepared from solutions in 30% acetic acid; (4) PVP foils loaded with 11 µg of drug; (5) PVP foils loaded with 250 µg of drug; (6) PVP foils loaded with 500 µg of ciprofloxacin; and (7) 50 µg of PVP-coated silver nanoparticels. n=3 for 1-6, n=1 for 7.

Toxicity was shown to be time and concentration dependent. The *ex vivo* model give no information about the type of cells been affected by applied test substances, however, in case of a material with an

unspecific mechanism of toxicity, like silver ions, it is a useful set up to detect over all acute toxic effects.

In recent years it has been recognized that fluoroquinolones, despite being well tolerated by a broad portion of patients, can have rare, very disabling side effects like tendon rupture and irreversible nerve damage [230]. There are several hypotheses about the mechanism of toxicity and the reason why some persons seem to be more prone than others to develop these side effects. One theory is that there might be a gene variant responsible for low quinolones metabolism. Thus, drug delivery systems able to deliver drug locally and maintain low systemic concentrations but effective and non-toxic local drug levels may prevent such toxic effects.

4.3.4 Efficacy of ciprofloxacin-loaded foils and nanofiber mats against PAO1 infections in the 3D wound model

A further possibility of the 3D *ex vivo* skin explant model is that wounds can be inoculated with bacteria to simulate an infection. To measure the efficacy of foils and nanofiber mats, we used the PAO1 infected wound model that was recently developed and characterized in our lab [130]. The used PAO1 strain possesses several proteolytic enzymes, among those collagenases, and use skin components as nutrients. Bacteria inoculated in the wounds grown from $1x10^7$ reaching a number of $1x10^9$ bacteria per wound after 20h of incubation [130]. *P. aeruginosa* can grow in both aerobic and anaerobic conditions. Accordingly, we found bacteria deep in the wound as well as on the wound surface. Most of the bacteria, however, grown on the surface, despite the fact that they were inoculated in deeper layers of the wound. Macroscopic, the surface of the PAO1 infected wound appeared shiny and yellowish (Figure 4.5A). Scanning electron microscopy images of the wound surface showed bacteria conglomerations typical of a biofilm: three-dimensional structures, resembling towers, made of microbes and extracellular materials (Figures 4.5 B, C). The microscopic pictures of stained skin sections revealed an approximately 10 µm-thick bacteria film on the surface of the wound. The

scanning electron microscopic analysis of the wound profile showed the details of the bacterial biofilm. PAO1 microbes, together with extracellular materials as well as digested skin connective tissue, were piled on each other to form compact assemblies (Figures 4.5 E, F). As also shown by *Schaudinn et al.* [130], after 20h of incubation, PAO1 had grown in the wound using connective tissue as adhesion surface as well as a nutrient. In addition, small agglomerates or scattered bacteria were found deep in the tissue (Figures 4.5 D, F). These PAO1 cells were growing slower than bacteria on the wound surface, probably due to less favorable conditions. Nevertheless, they represent a risk for potential recurrent infections after treatment is completed. For this reason, the penetration of adequate drug concentrations in the wound and the eradication of small bacterial colonies deep in the wound tissue is a crucial factor for successful therapy. Thus,

besides the possibility to study the mechanisms of PAO1 wound infections and skin immune response, this animal-free model offers also a 3D set up suitable for testing new anti-biofilm treatments as well as strategies for targeting bacteria difficult to reach, e.g. small colonies deep into the wound or intracellular bacteria.

Pseudomonas aeruginosa has already been cultured on *ex vivo* human skin. However, different protocols were used in the different studies and often the induced infection was poorly characterized. Schmidtchen *et al.* used 4 mm skin biopsies that were immersed in a medium where bacteria were inoculated together with the treatment substance [231, 232]. Vieira et al. used *ex vivo* human skin to test the efficacy of phage therapy but no wound was induced, and PAO1 bacteria were applied on the skin surface, and only superficial bacteria were collected and counted after treatment [233].

In another study, pig skin was used, where a wound was created by a punch biopsy and a bacterial suspension of S. aureus was applied on the top of the wound for 2h before treatment. Nevertheless, bacteria were cultured and harvested only from the surface of the wound while deeper tissue infection was not investigated [234].

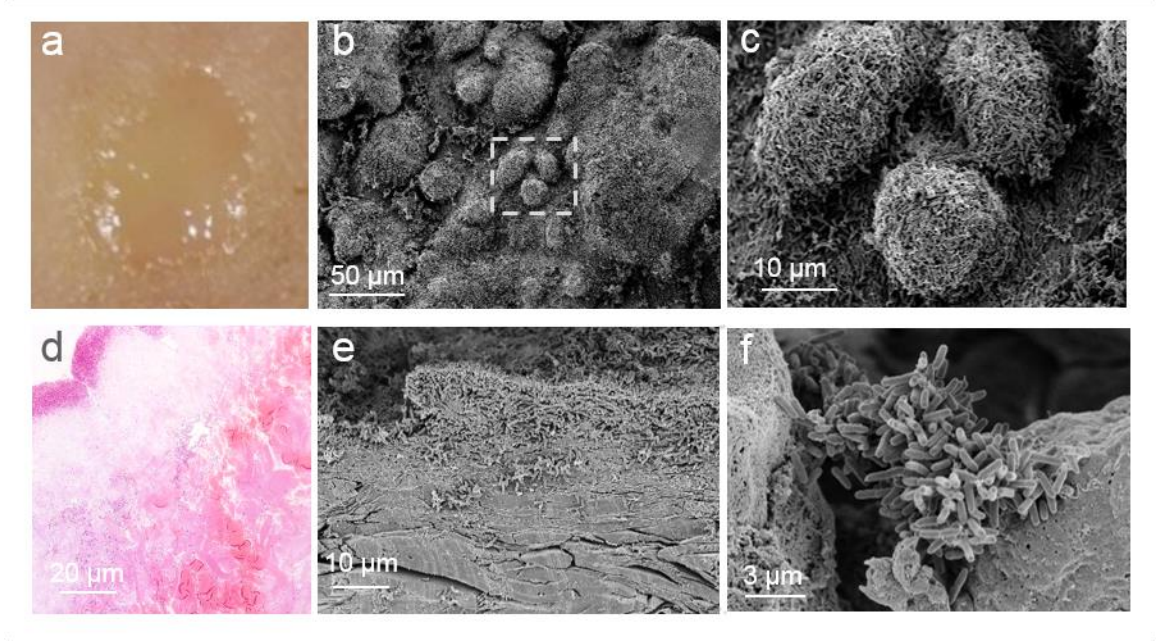

Figure 4.5 Wound infection model with PAO1. A superficial wound of approximately 5 mm in diameter was applied on skin explants. Bacteria ($1x10^7$ per wound) were inoculated and incubated in the skin for 20 h. **A**, Microscopic appearance of a representative wound after growing of PAO1 biofilm. **B**, **C**, SEM images of wound surface at two different magnification showing the typical biofilm morphology of bacterial communities. **D**, Wound section stained with A&E showing a bacteria film on the surface and d more scattered bacteria deep into the wound. **E**, **F**, SEM images of skin sections at different magnifications showing bacterial cell agglomeration on the surface (E) and deep in the wound (F).

In general, most of the studies did not consider the three-dimensional aspect of the model. On the contrary, Phillips *et al.* used porcine skin to model PAO1 wound infections by injecting the bacteria in the tissue and measuring the efficacy of topically applied treatments by extracting all bacteria at the end of the experiment [223]. Even if the infection was not characterized, this set up is more adequate to investigate the efficacy of treatment towards superficial as well as deep bacteria.

In this study, a similar experimental protocol to test the efficacy of innovative wound dressing materials was used. Further, the 3D *ex vivo* infection model was exploited to correlate the antibacterial efficacy of the tested materials with their drug delivery properties.

The investigate foils, and nanofiber mats were loaded with three different concentrations of ciprofloxacin, corresponding to final concentrations of 11, 250, and 500 µg per wound. The treatment was applied 1h or 20h after inoculation of the bacteria in the wound followed by further 20h of incubation. Samples treated 1h after bacteria inoculation served to test the drug efficacy on planktonic bacteria (approximately $1x10^7$), whereas samples treated 20h after PAO1 inoculation served to test the efficacy of foils and nanofiber mats on a high concentration of bacteria (approximately $1x10^9$) primarily organized into a biofilm. Macroscopically, a thick, yellow biofilm was visible on the surface of untreated wounds after 20h of incubation, whereas no bacterial film was visible on the treated samples (Figure 4.6A). When applied 1h after bacterial inoculation, both foils and nanofiber mats resulted efficient independently from the amount of loaded drug. The 20h biofilm infection was more difficult to treat. The best efficacy was measured for the PVP foils (Figure 4.6B). Foils loaded with 500 µg ciprofloxacin achieved a complete eradication of the bacteria, and the two lower concentrations resulted in a 3-log reduction of bacteria concentration with respect to the untreated controls. For nanofiber mats, a lower antimicrobial activity was measured with a maximal 3-log reduction measured by the highest concentration. Control experiments were also run to measure the potential antibacterial activity of plain PVP foils prepared using water or 30% acetic acid. No effects on bacterial growth was measured for these controls.

The most striking result is that the 500 µg PVP foils achieved the complete eradication of the biofilm infection. The superior efficacy of the foils compared to the nanofiber mats is probably due to the release kinetics.

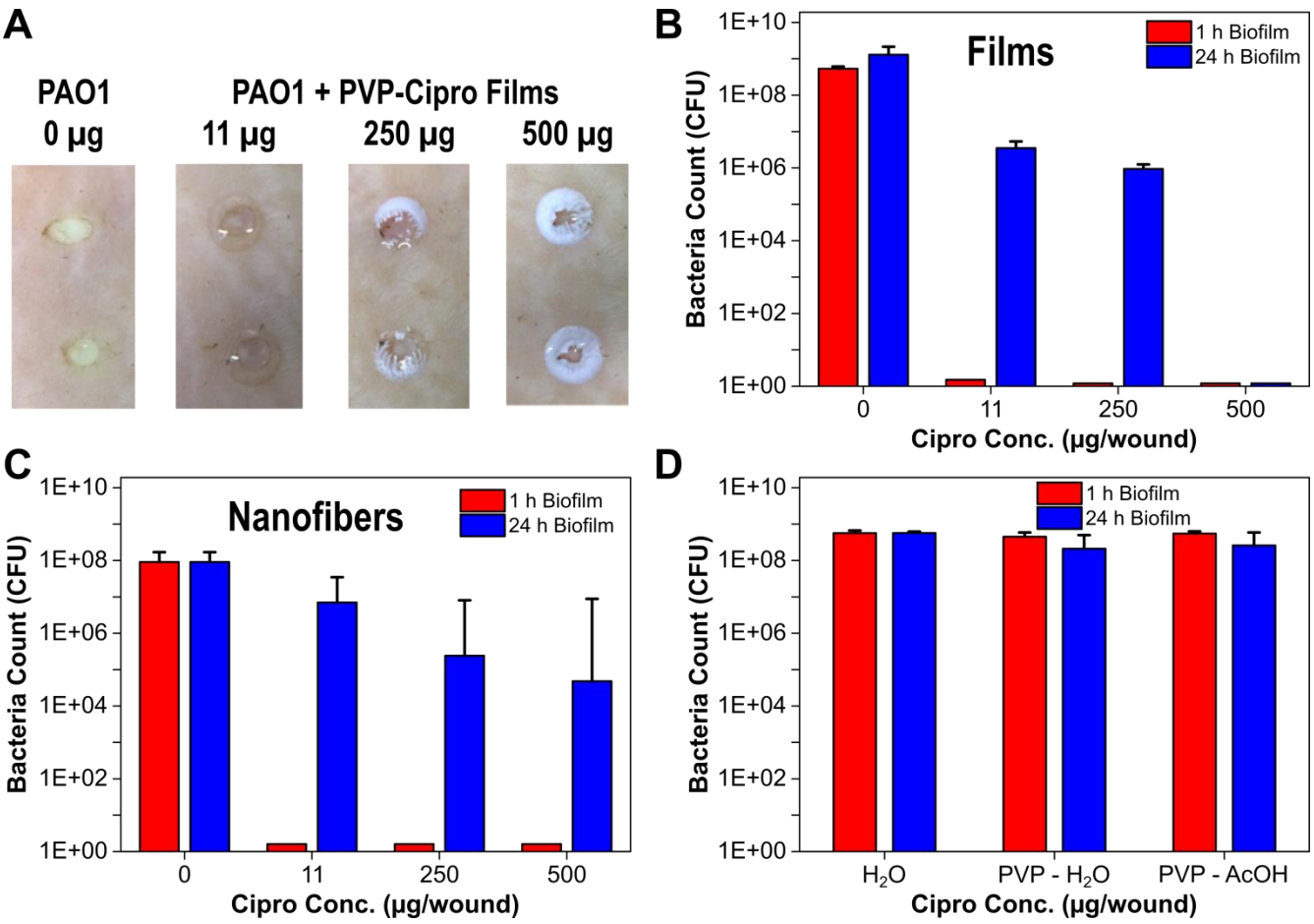

Figure 4.6 Antimicrobial efficacy of PVP foils and nanofiber mats with different ciprofloxacin payloads applied to the wound 1h or 20h after PAO-1 inoculation. Representative pictures (**A**) and CFU unit counts in tissue extracts after wound infection with PAO1 and treatment with foils (**B**) or nanofibers (**C**) loaded with different concentrations of ciprofloxacin (Cipro) as well as plain PVP foils prepared from solutions in water or 30% acetic acid (**D**).

While with the foils high drug concentrations were obtained already 2h after topical application and were maintained over 24h, with nanofiber mats the highest concentration was reached 6h after application and was already decreased after 16h of incubation. Phillips *et al.* assessed the efficacy of several commercially available treatments in porcine ex vivo wound model and found that only time-

release silver gel and cadexomer iodine dressings were the most effective in reducing mature biofilm with a reduction between 5 and 7 log of 7-log total [223]. Using an *in vivo* mouse model, Roy *et al.* found out that ciprofloxacin-loaded keratin-based hydrogels with a sustained drug release profile could reduce the amount of P. aeruginosa in the wound bed by 99.9% without interfering with key processes of wound healing [235]. Thus, these and our results underline the importance of drug delivery systems with sustained release profile for an efficient treatment of P. aeruginosa wound infections.

4.4 Conclusions

In this chapter, on a 3D *ex vivo* wound infection model was investigated the efficacy and tolerability of PVP-based foils and nanofiber mats. The 3D model allowed to test the antimicrobial efficacy of these innovative materials and correlate it to their delivery properties. The results showed that, despite nanofiber mats dissolved faster *in vitro*, foils had a better delivery profile of ciprofloxacin base in the wound. High concentration and sustained drug delivery were required for successful eradication of the PAO1 biofilm infection.

Ciprofloxacin was used as an example of a poorly water-soluble drug. PVP-based delivery systems can be used to load different types of antimicrobials with different molecular weight and water-solubility. Thus, especially the elastic, adhesive and transparent PVP-foils represent attractive new pharmaceutical forms for topical drug delivery. Beside their sustained drug release properties, foils also allow for more precise dosing of the active. Finally yet importantly, foils hold the potential for reaching high patient compliance because they can be applied easily and quickly also in skin areas difficult to reach for old and disabled patients, e.g. the lower back or between the toes.

Chapter 5 : Transparent biopolymer films based on the dietary phenolic *p*-coumaric acid and PVP for controlled release

5.1 Discovering *p*-coumaric acid and its biological properties

Most commercially available medical formulations derive from natural products [236]. For instance, there are many drug delivery systems and therapeutic approaches based on the use of biopolymers as well as alternative natural bio-active agents such as essential oils [83, 237, 238] and propolis [239], with polyphenols as their main active components. These organic chemicals are characterized by the presence of phenol structural units and have notable antioxidant properties [92, 240]. Among this large class of compounds, hydroxycinnamic acid derivatives, also known as dietary phenolic compounds, such as ferulic, caffeic, and *p*-coumaric (4-hydroxycinnamic acid, PCA) acids have gained a growing interest due to their remarkable biological activity: they can reduce the inflammatory response [241, 242], show protective effect against cancer and atherosclerosis [243-246], affect the angiogenesis process [247-249], and interact with the β-amyloid (*i.e.*, the main protein involved in Alzheimer disease), affecting the formation of toxic protein fibrils [250, 251]. For instance, Abdel-Wahab *et al.* [252] demonstrated that PCA protects rats' hearts against doxorubicin-induced oxidative stress, while Ferguson *et al.* [253] showed that ferulic and *p*-coumaric acids have a better activity in comparison to curcumin, another common polyphenol, protecting cultured mammalian cells against oxidative stress and genotoxicity. On the other hand, Luo *et al.* [254] described a double antibacterial action mechanism for PCA. Recently, several studies have demonstrated that these medically beneficial compounds are also suitable for the treatment of skin issues due to their strong antioxidant properties [83, 237]. Indeed, several types of skin damages and diseases are characterized by local and/or protract inflammatory and oxidant events that drastically increase the levels of interleukin and free radicals, causing cellular damages, slowing down the healing process, and potentially driving into the chronic state [255]. Ghaisas *et al.* [256] evaluated the administration of ferulic acid as an oral solution and in the form of ointment for topical delivery in an excision wound model on diabetic rats that produced the reduction of inflammation and the acceleration of the healing process. In addition, PCA and other

phenolic acids have been reported as efficient photoprotective agents for skin against dangerous solar ultraviolet radiation (UVB) [257-259].

Although PCA has antioxidant properties, as previously demonstrated in cultured cells [241, 244, 260] and animal models [260-264], its activity on cutaneous wound healing is yet to be investigated in detail. In this sense, incorporation of PCA in pharmaceutical polymeric matrices, like PVP, can yield alternative antibiotic-free biomaterials that can be used in the treatment of infected wounds. PCA integrated skin dressing systems can potentially regulate the levels of free radicals and pro-inflammatory molecules for healing skin along with other important parameters, such as antibacterial activity, good adhesion, exudate absorption, transparency and resorbing from the skin [60]. Recently, we demonstrated the possibility of using polyvinylpyrrolidone (PVP) as a biocompatible polymer matrix for fabrication of skin wound dressing films with a high level of transparency, adhesion to the skin, for controlled ciprofloxacin release [203].

Here, we present the fabrication of new biomaterials in the form of transparent, free-standing films composed of different proportions of PCA and PVP blended in ethanol solutions. We demonstrate that both components strongly interact by H-bonds and this allows the fine-tuning of thermal, mechanical, and hydrodynamic properties. The incorporation of PCA into PVP not only confers antioxidant and antibacterial properties to the polymer but also controlled the release of model drugs due to increased water dissolution resistance. Furthermore, PVP/PCA 2:1 films demonstrated promising activity in reducing matrix metallopeptidase 9 (MMP-9) levels in a wound mice model that indicates the future potential for chronic wound treatment.

5.2 Materials and Methods

5.2.1 Materials

Polyvinylpyrrolidone (MW = 1300000 Da), *p*-Coumaric acid (≥98.0% HPLC; MW = 164.16 g/mol), carminic acid (CA; MW = 492.39 g/mol), methylene blue (MB; MW = 319.85 g/mol), ethanol, and phosphate buffered saline (PBS) solution (pH 7.4) were purchased from Sigma-Aldrich and used without further purification.

5.2.2 Preparation of the films

PVP/PCA solutions with different molar ratios were prepared by dissolving PCA and PVP powders in 15 mL of ethanol. The solutions were first shaken (standard lab shaker) overnight, casted onto plastic Petri dishes (5 cm diameter), and dried for 2 days under an aspirated hood ambient conditions (16-20°C and 40-50% R.H.). Films with PVP/PCA molar ratio of 10:1, 7.5:1, 5:1, 3.5:1, and 2:1 were prepared, Table 1. The films had an average thickness of (170 ± 30) μm. Samples with higher PCA contents were not prepared due to the segregation of both components and macroscopic crystallization of *p*-coumaric acid. A control film of the only PVP at 3% (w/v), labeled as PVP/PCA 1:0, was also fabricated. PCA powder was the sample PVP/PCA 0:1.

To investigate the dispersion and delivery of model drugs in the PVP/PCA formulation, samples loaded with methylene blue (MB) and carminic acid (CA), were prepared. In particular, 10 mg of MB and 15 mg of CA, respectively, were added to 15 mL solutions of PVP/PCA 1:0, 10:1 and 2:1.

Sample Label	Molar ratio PVP/PCA	The molar fraction of PCA	Weight % of PCA	Weight % of MB respect to PVP	Weight % of CA respect to PVP
PVP/PCA 1:0	1:0	0.00	0	-	-
PVP/PCA 10:1	10:1	0.09	12.8	-	-
PVP/PCA 7.5:1	7.5:1	0.12	16.3	-	-
PVP/PCA 5:1	5:1	0.17	22.6	-	-
PVP/PCA 3.5:1	3.5:1	0.22	29.5	-	-
PVP/PCA 2:1	2:1	0.33	42.2	-	-
PVP/PCA 0:1	0:1	1.00	100	-	-
PVP/PCA 1:0+MB	1:0	0.00	0	1.0	1.6
PVP/PCA 10:1+MB	10:1	0.09	12.8	1.0	1.6
PVP/PCA 2:1+MB	2:1	0.33	42.2	1.0	1.6
PVP/PCA 1:0+CA	1:0	0.00	0	1.0	1.6
PVP/PCA 10:1+CA	10:1	0.09	12.8	1.0	1.6
PVP/PCA 2:1+CA	2:1	0.33	42.2	1.0	1.6

Table 5.1 Sample labeling, molar ratio between PVP and PCA, molar fraction of PCA, weight percentage of both components, and concentration of drugs used.

5.2.3 Scanning Electron Microscopy (SEM)

Morphology of the films was analyzed by Scanning Electron Microscopy (SEM), using a variable pressure JOEL JSM-649LA microscope equipped with a tungsten thermionic electron source working in high vacuum mode, with an acceleration voltage of 10 kV. The specimens were coated with a 10 nm thick film of gold using a Cressington Sputter Coater – 208 HR.

5.2.4 X-ray diffraction

X-ray diffraction (XRD) measurements were performed on a PANalytical Empyrean X-ray diffractometer by using a Cu Kα anode (λ = 1.5406 Å) operating at 45 kV and 40 mA. The diffraction patterns were collected in the range 5–70° 2θ with a 0.02° step size.

5.2.5 ATR-FTIR spectroscopy

Infrared spectra were obtained with an ATR accessory (MIRacle ATR, PIKE Technologies) with a diamond crystal coupled to a Fourier Transform Infrared (FTIR) spectrometer (Equinox 70 FT-IR, Bruker). All spectra were recorded in the range from 3800 to 600 cm^{-1} with a resolution of 4 cm^{-1}, accumulating 128 scans.

5.2.6 NMR spectroscopy

~65 mg of samples were dissolved in DMSO-d6 (deuterated DMSO) and transferred into 5 mm disposable tubes. NMR experiments were acquired on a Bruker Avance III 600 MHz spectrometer, equipped with 5 mm QCI cryoprobe, at 303K, after an automatic 90° pulse optimization. ^{1}H-NMR was acquired with 16 transients, over a spectral width of 20.03 ppm (offset at 4.7 ppm), at a fixed receiver gain (1), and using 30 s of inter pulses delay. 1D-CPMG (Carr-Purcell-Meiboom-Gill) was acquired with 4 transient, over a spectral width of 20.03 ppm (offset at 4.7 ppm), at a fixed receiver gain (1), by using an inter pulse spacing of 0.3 ms, a duty cycles of 126, and 30 s of inter pulses delay. A line

broadening of 0.3 Hz was applied to FIDs (Free Induction Decay) before Fourier Transform. All the NMR chemicals shifts were referred to the not deuterated DMSO-d6 residual peak at 2.5 ppm.

5.2.7 Thermal characterization

The thermal stability behavior of the films was investigated by a standard thermogravimetric analysis (TGA) method, using a TGA Q500 from TA Instruments. Measurements were performed with 3-5 mg samples in an aluminum pan under inert N_2 atmosphere with a flow rate of 50 mL/min in a temperature range from 30 to 600°C and with a heating rate of 5°C/min. The weight loss and its first derivative were recorded simultaneously as a function of time/temperature. Differential Scanning Calorimetry (DSC) thermograms were acquired with a DSC Q20 (TA Instruments) from RT to 200 °C under nitrogen flow (50 mL/min) at 20 °C/min using non-hermetic aluminum pans. About 4 mg (weighted with +0.00001 g precision) of the sample were used. Specimens were first heated to 150 °C to release moisture, cooled to RT and finally ramped to 200 °C. The glass transition temperature (T_g) was calculated using the inflection method.

5.2.8 Water absorption

The water absorption capacity of the films was obtained as follows: dry samples were weighed (~100 mg) on a sensitive electronic balance and placed in different chambers with controlled, increasing humidity. The humidity conditions were: 0%, 11%, 44%, 84%, 100%. After conditioning in different humidity chambers until equilibrium conditions (usually 24 h), each film was weighed, and the amount of absorbed water was calculated based on the difference between the weight of each film and its initial dry weight.

5.2.9 Water contact angle

Static water contact angle measurements were performed by using the sessile drop method with a DataPhysics OCAH 200 contact angle goniometer equipped with a CCD camera and image processing

software operating under laboratory conditions (temperature 22–25 °C and relative humidity 50–60%). For the characterization, droplets of 1 µL volume MilliQ water were used. Up to 10 contact angle measurements were carried out on each sample at random locations, and their average values and standard deviation were reported.

5.2.10 ABTS free radical cation scavenging assay

The ABTS radical cation ($ABTS^{\cdot+}$) was generated by the reaction between 7 mM ABTS water solution with 2.45 mM potassium persulfate solution in the dark at room temperature for 12-16 hours. The $ABTS^{\cdot+}$ solution was diluted with water to obtain an absorbance of 0.80 a.u. At 734 nm. After that, 5x5 mm^2 films were added to 3 mL of diluted $ABTS^{\cdot+}$ solution. The decrease in absorbance was determined at 734 nm with a Cary 300 Scan UV-visible spectrophotometer at different times. All the measurements were performed in triplicate, and the results were averaged to obtain a mean value. Radical scavenging activity (RSA) was expressed as the inhibition percentage of free radical of the sample and calculated as follows[255, 265]:

$$Radical\ Scavenging\ Activity\ (\%) = \frac{A_0 - A_1}{A_0}\ x\ 100$$

where A_0 is the absorbance value of the control radical cation solution, and A_1 is the absorbance value of the sample at different times.

5.2.11 Mechanical tests

The mechanical properties of the PVP/PCA samples were determined by uniaxial tension tests on a dual column universal testing machine (Instron 3365). Films were cut in dog bone specimens (at least seven of them for each sample) with a width of 4 mm and an effective length of 25 mm. Displacement was applied at a rate of 10 mm/min. The Young's modulus, stress at maximum load, and elongation at break were calculated from the stress-strain curves. All the stress-strain curves were recorded at 25 °C and 44 % R.H.

5.2.12 Drug release studies

The release of PCA, MB, and CA from PVP-PCA films was performed by using a Cary 300 Scan UV-visible spectrophotometer. PCA, MB, and CA present characteristic UV absorbance peaks at 334, 664, and 528 nm, respectively. Calibration curves were made to calculate the molar extinction coefficients (ε) for these substances, resulting in 22200 cm^{-1} M^{-1} for PCA, 26000 cm^{-1} M^{-1} for MB, and 8520 cm^{-1} M^{-1} for CA. Samples were cut in round shapes with a diameter of 0.8 mm and placed in 24-well plates with 2.5 mL of PBS. For the release of PCA, at each time point (1, 5, 10 15, 20, 30 minutes and 1, 2, 3, 4, 6, 8, 12, 24, 48, 72 hours), 100 µL of the solution were taken out and substituted with 100 µL of fresh medium. Similarly, in the release studies of MB and CA release, at the given times points, 500 µL of the solution were taken out and replaced with 500 µL of fresh PBS. All the measurements were carried out at room conditions (22–25 °C and 50–60% R.H.). For each sample, triplicates were used and the experiment was repeated twice.

5.2.13 Antibacterial tests

0.5 cm^2 pieces of PVP-PCA 1:0, 10:1, 5:1, and 2:1 films were sterilized under UV at 254 nm for 30 minutes. 50 µL of a diluted ($1:10^4$) Gram-negative *Escherichia coli* (*E. coli*) or Gram-positive *Staphylococcus aureus* (*S. aureus*) cultured overnight were spread on LB or blood agar plates respectively, and after 10 minutes the film samples were placed in the center of the plates and incubated at 37 °C overnight. The inhibitory effect on bacterial growth was determined by measuring the radius of the bacteria-free zone.

5.2.14 Full-thickness skin wound model

In vivo experiments were performed according to the guidelines established by the European Communities Council Directive (Directive 2010/63/EU of 22 September 2010) and approved by the National Council on Animal Care of the Italian Ministry of Health. 8–12 weeks old male C57BL/6J

mice (Charles River, Calco, Italy) were used. They were maintained under a 12-hour light/dark cycle (lights on at 8:00 am) under a controlled temperature of (21 ± 1) °C and relative humidity of (55 ± 10) % conditions. All efforts were made to minimize animal suffering and to use the minimal number of animals required to produce reliable results. The dorsal skin of mice was shaved after light anesthesia induced by intra-peritoneal injection of ketamine (10%) and xylazine (5%) mixture. One full-thickness skin wound was created in the center of the back of each animal, using a sterile 6-mm biopsy punch. The wounds were photographed and covered with PVP/PCA 2:1 or PVP/PCA 10:1 films (n = 5 each experimental group). To avoid the removal of the dressings when the animals awake, all treated wounds were covered with Tegaderm™ just before the animals woke, until the end of the experiment. To evaluate bio-resorption over time, the condition of each dressing has been photographed at different time intervals (1, 3, 5, 15, 30, 60, 120, 240, 360, 1440 min) after film application with a Microscope Leica digital camera. ImageJ software was used for the analysis of each picture to calculate the percentage of the bio-resorbed membrane during the time[158]. Mice were housed individually during the experiments, with water and food *ad libitum*. All animals were sacrificed at the end of the experiment by carbon dioxide euthanasia.

5.2.14 MMP-9 measurement by Western blot

Skin samples from Naïve, Sham, PVP/PCA 2:1, and PVP/PCA 10:1 groups were collected 48 h post wound induction and stored at -80 °C. Tissues were homogenized in lysis buffer (150 mM sodium chloride, 50 mM Tris·HCl, pH 8.0, 0.5% sodium deoxycholate, 0.1% SDS, and 1% Triton X-100). The tissue extract was cleared by centrifugation (15 min at 12000x g, 4 °C). Proteins (30 μg) were separated by SDS/PAGE and transferred to nitrocellulose membranes. Anti–MMP-9 (1:100; Abcam) and antiGAPDH (1:2000; Abcam) antibodies were used followed by incubation with, respectively, anti-rabbit and anti-mouse IgG antibody (1:5000; Millipore). Finally, MMP9 and GAPDH were visualized

with a chemiluminescence kit (Bio-Rad). Images were obtained by using a LAS-4000 lumino-image analyzer system (Fujifilm).

5.3 Results and Discussion

5.3.1 Morphological characterization

Figure 5.1A shows the photographs of PVP/PCA samples. As observed, all of them were transparent. PVP/PCA 1:0 (pure PVP) was colorless while a light orange color started to appear as the PCA content was increased due to the presence of the phenolic acid [266, 267]. The micro-morphology was also analyzed by SEM, Figure 5.1B. A flat, featureless, smooth surface was observed for all samples, with no presence of aggregates, segregation or PCA crystals, indicating that the polymer and the phenolic acid were miscible in the concentration range investigated, as confirmed in the following sections.

5.3.2 Chemical and structural characterization

The miscibility and crystalline structure of pure PVP, *p*-coumaric acid, and the corresponding blends were characterized by XRD in Figure 5.2A. PVP showed two broad halos centered at 10.8 and 20.8°, typical of the amorphous structure of the polymer [25, 268]. On the other hand, pristine PCA exhibited an XRD pattern with multiple narrow peaks indicative of a well-defined monoclinic crystal system characteristic of the acid [269]. The diffraction patterns are shown in Figure 5.2A. The absence of crystalline peaks from PCA fraction in the blends revealed that the acid was included in the amorphous structure of the polymer matrix. As such, no phase separation was determined, suggesting a high-level of miscibility between both components. Similar behavior has been described for solid dispersions of PVP with other drugs such as curcumin, piroxicam, ketoconazole, and flunarizine [24-26, 268]. To further investigate the interactions between PVP and PCA, ATR-FTIR spectroscopy was carried out as shown in Figures 5.2B,C.

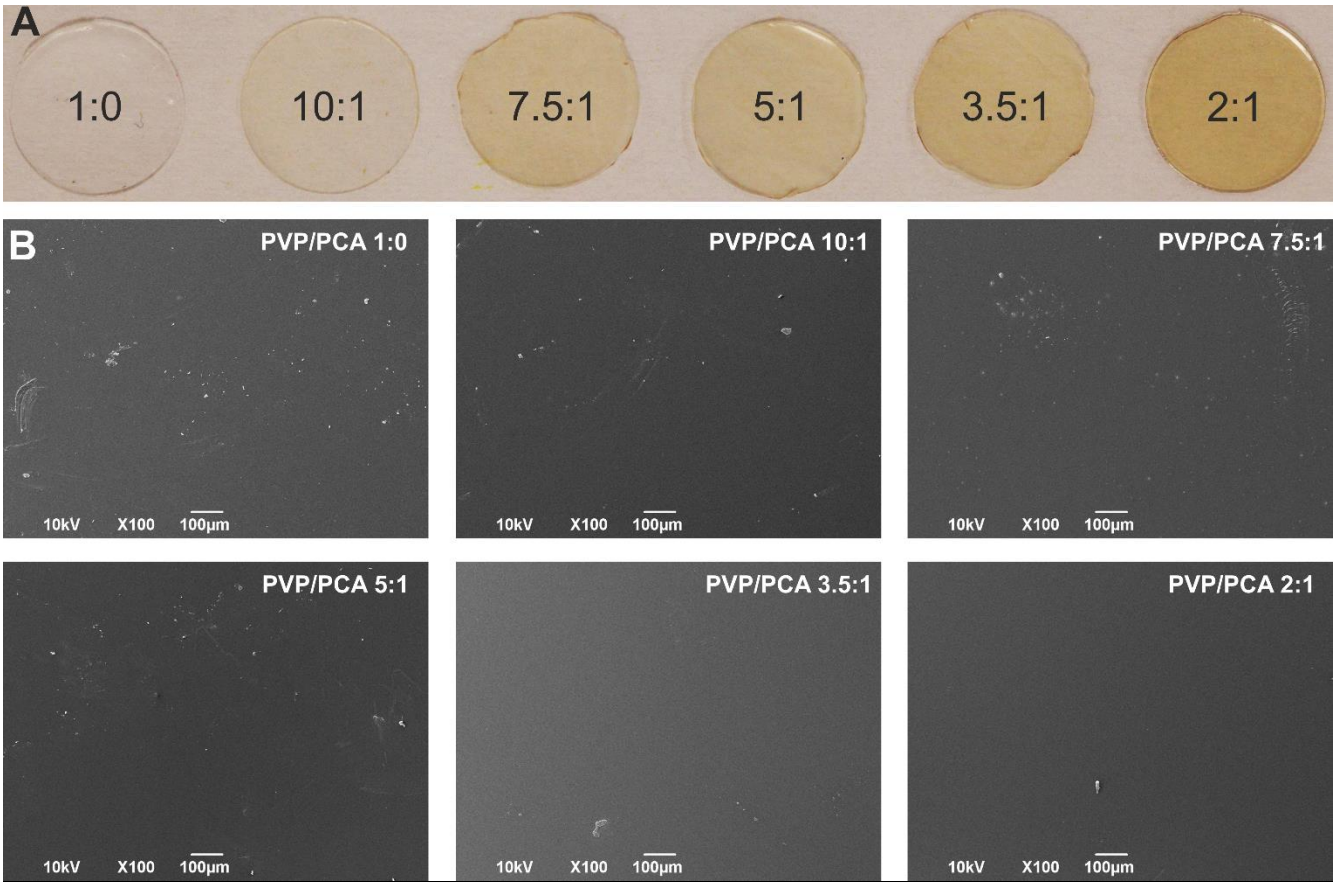

Figure 5.1 A, **B**, photographs and SEM top-view images, respectively, of PVP/PCA samples.

Figure 5.2B shows the infrared spectra of PVP, *p*-coumaric acid, and PVP/PCA 2:1, 5:1, and 10:1 samples. Main bands of PVP were associated with the chemical structure of the polymer: O-H stretching mode at 3403 cm^{-1}, asymmetric and symmetric CH_2 stretching mode at 2951 and 2868 cm^{-1}, respectively, C=O stretching mode at 1645 cm^{-1}, C-N stretching mode at 1018 cm^{-1}, out-of-plane C-H bending mode at 845 cm^{-1}, and C-H rocking mode at 735 cm^{-1} [160]. On the other hand, PCA was characterized by the following bands: O-H stretching mode at 3375 cm^{-1}, C=O stretching mode at 1685 cm^{-1}, C=C stretching mode at 1668 cm^{-1}, two in-plane C-H deformation modes at 1215 and 690 cm^{-1}, and out-of-plane C-H bending mode at 829 cm^{-1} [270]. For the blends, most of the bands overlapped in the spectral region between 1800 and 600 cm^{-1}. However, a new band at ~3175 cm^{-1} related to

hydroxyl groups interacting by strong H-bonds appeared, Figure 5.2C. The intensity of the band was higher, and the wavenumber lower as the PCA content increased, revealing a stronger H-bond network between the polymer matrix and the acid depending on the amount of *p*-coumaric acid. In the end, the formation of any kind of chemical bond between both species during the preparation of the films was discarded, as checked by NMR and reported in Figures 5.3 and 5.4.

The ^{1}H NMR spectrum of PVP shows signals between 1 and 4 ppm whose assignments are reported in Figure 5.3A. Such signals are broad and with unresolved fine structure, characteristic of polymers (with short T_2, the transversal correlation time). On the contrary, signals between 6.26 and 7.53 ppm are sharp and with a recognizable multiplicity, typical of small molecules (with long T_2 time) [271]. Assignments, in such a region, reported in Figure 5.3B, are attributed to the *p*-coumaric acid moiety (region of double bonds and aromatic ^{1}H). Such signals remain substantially unaffected by applying a 1D-CPMG [272] acquisition scheme Figure 5.4 while the broad signals belonging to the PVP moiety are reduced in intensity down to the baseline. We can thus exclude that the *p*-coumaric acid is chemically bound to the PVP.

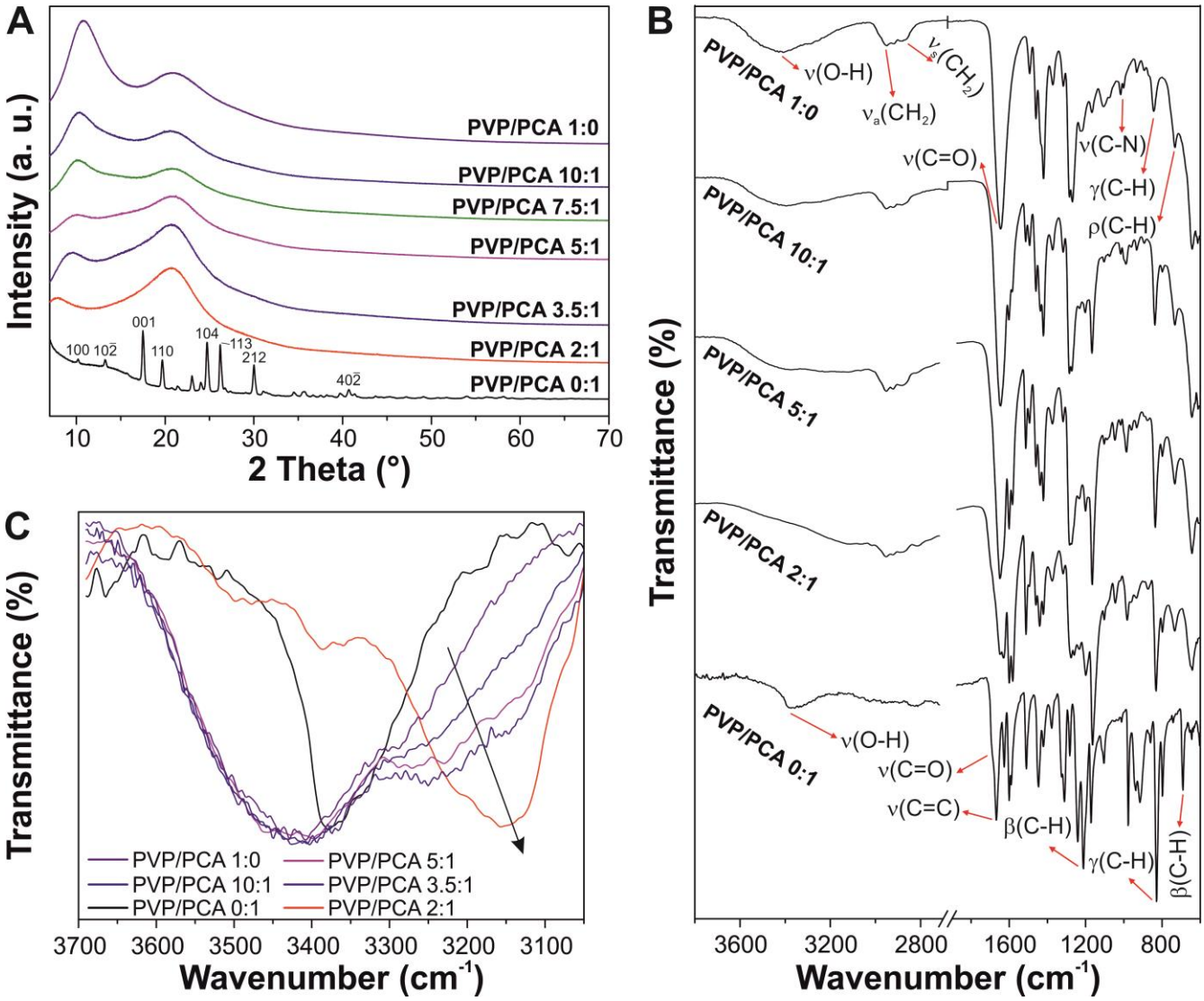

Figure 5.2 A, XRD patterns of PVP/PCA samples. Several crystalline peaks are detected for PVP/PCA 0:1, while the rest of the samples show two broad bands. Main assignations of the XRD pattern of PVP/PCA 0:1 are included. **B**, ATR-FTIR spectra of PVP/PCA 1:0, 10:1, 5:1, 2:1, and 0:1. Main assignments of pure PVP and *p*-coumaric acid are included. **C**, variation of the OH stretching band for PVP/PCA 1:0, 10:1, 5:1, 2:1, and 0:1 samples. The arrow is a visual guide that indicates the shift of the band in this region, indicative of stronger H-bonds.

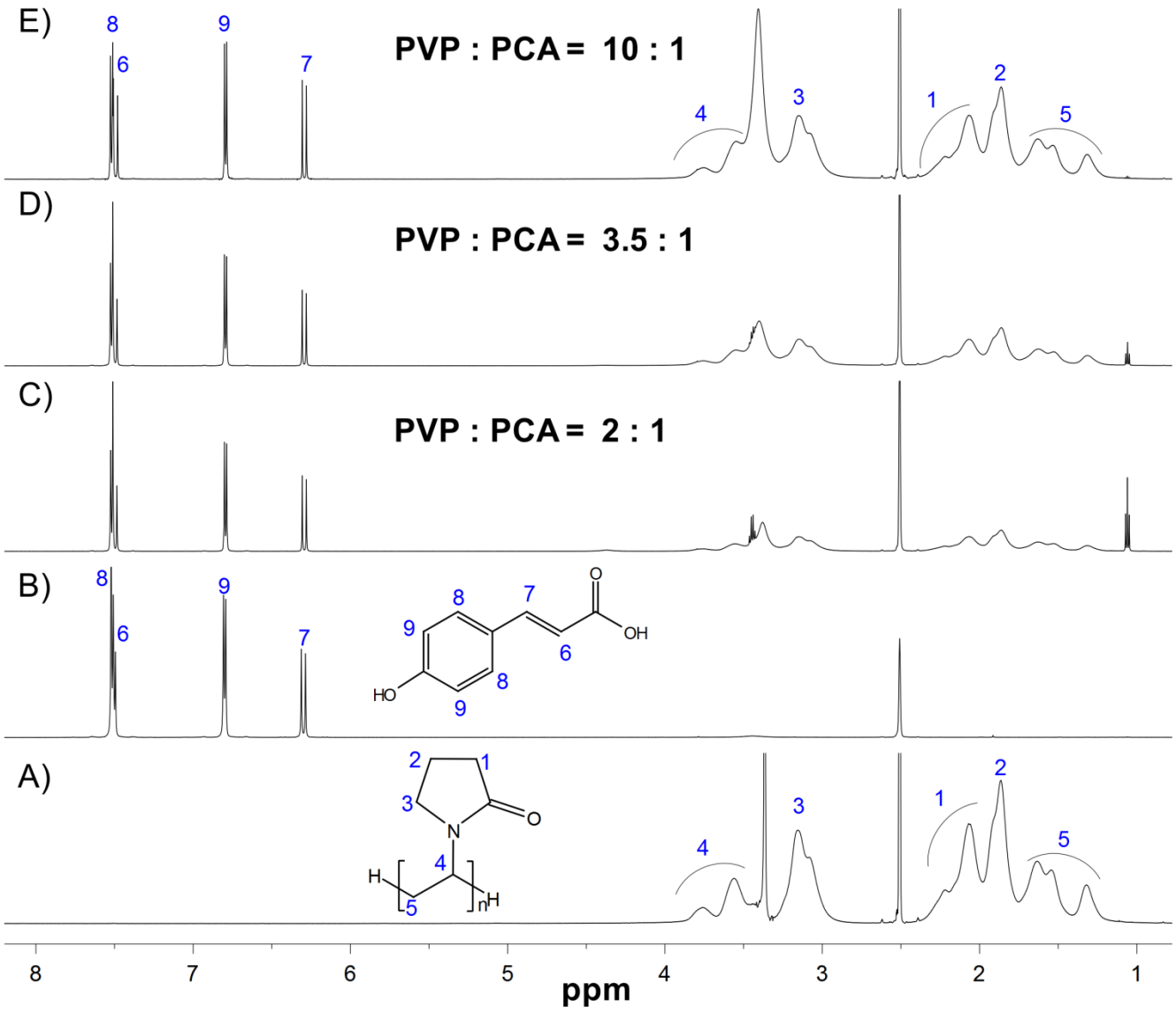

Figure 5.3 ^{1}H NMR in DMSO-d6 of **A**) PVP, **B**) PCA, **C**) PVP/PCA 2:1, **D**) PVP/PCA 3.5:1, **E**) PVP/PCA 10:1.

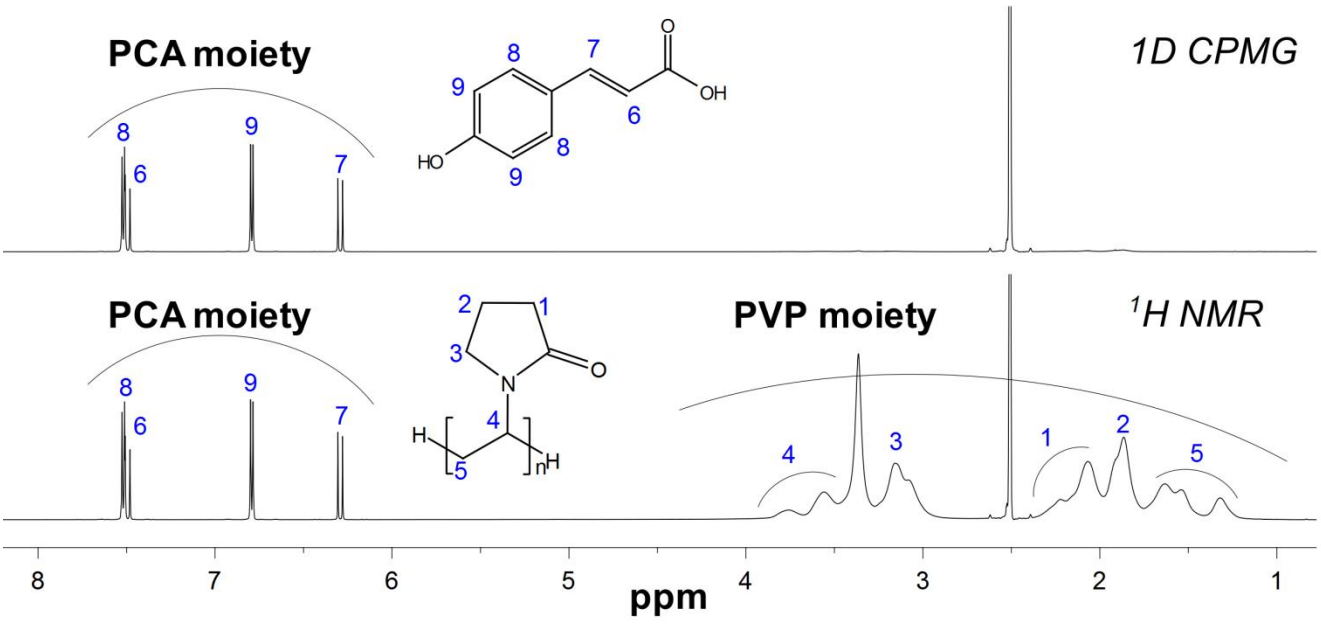

Figure 5.4 ^{1}H NMR and 1D-CPMG of the PVP/PCA 10:1 sample in DMSO-d6. The PVP signals are suppressed after the application of a 1D CPMG acquisition scheme, while the signals of PCA are only slightly decreased in intensity (due to their intrinsic T_2 resonance decay). Analogous results were obtained with all the samples.

5.3.3 TGA and DSC analysis

The thermal properties of the PVP/PCA samples were evaluated by TGA and DSC, Figure 5.5. Figure 5.5A shows the thermogravimetric analysis of PVP/PCA 0:1, 2:1, 5:1, 10:1, and 0:1 samples. For pure PCA an intense weight loss of ~87% at 216°C related to the thermal decomposition of the molecule was observed [273]. On the other hand, PVP showed two different thermal events at 64°C and 427°C (weight losses of ~16 and ~84%, respectively) associated with the evaporation of the retained solvent and the degradation of the polymer backbone, respectively [274]. The TGA for the blends displayed an intermediate behavior with events from both components. However, as the amount of the acid

increased, a shift to lower values of the maximum decomposition temperature of PCA was determined, inset of Figure 5.5A, suggesting good miscibility between both components [275].

DSC characterization of PVP/PCA samples showed a single glass transition in Figure 5.5B. No thermal events associated with melting or crystallization processes were observed, indicating the amorphous nature of films, as previously confirmed by XRD. The glass transition temperature linearly decreased from 183°C for pure PVP to 91°C for PVP/PCA 3.5:1, then the value slightly decreased to 89°C for PVP/PCA 2:1. Such depression of the glass transition temperature is typical of a plasticization of polymer matrixes by addition of molecules that weaken selective intermolecular interactions between polymer chains and increase the free volume of the system. In this case, PCA molecules by formation of H-bonds with PVP, as elucidated by infrared spectroscopy, can effectively separate the polymer chains, thus reducing the T_g.

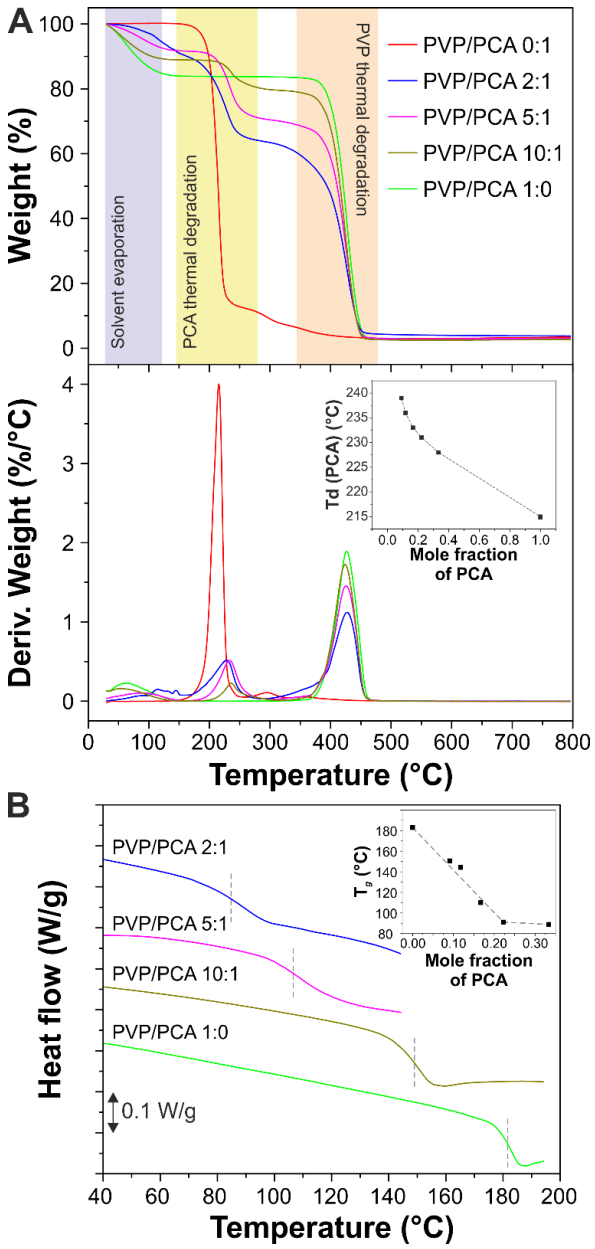

Figure 5.5 A, TGA thermograms (top) and derivative thermogravimetric curves (bottom) of PVP/PCA 0:1, 2:1, 5:1, 10:1, and 0:1 samples in the range of temperatures between 25 and 800°C. Main thermal events are highlighted. The inset in the bottom graph shows the temperature of maximum degradation of *p*-coumaric acid as a function of the mole fraction of PCA. **B**, DSC curves of PVP/PCA 0:1, 2:1, 5:1, 10:1, and 0:1 samples in the range of temperatures between 40 and 200°C. The glass-transition temperatures have been highlighted with grey dashed lines. The inset shows the variation of the T_g with the mole fraction of PCA in the film.

5.3.4 Mechanical characterization

The mechanical properties were evaluated by tensile tests, Figure 5.6. Figure 5.6A displays the typical stress-strain curves of the films, while the values for Young's modulus, stress at maximum load, and the elongation at break are plotted as functions of the mole fraction of PCA in Figures 5.6B,C,D, respectively. Pure PVP presented the behavior of a rigid polymer with high Young's modulus and stress at maximum load (1095 and 25 MPa, respectively) and low elongation at break (3.7%). When small amounts of PCA were added, (PVP/PCA 10:1 and PVP/PCA 7.5:1 samples) PCA acted as a reinforcement agent increasing Young's modulus and stress at maximum load and keeping the value for elongation at break. From this molar ratio, samples with richer contents of the acid became ductile reducing their values of Young's modulus and stress at maximum load and increasing the elongation at break. In particular, Young's modulus, stress at maximum load, and elongation at break were 35 MPa, 0.75 MPa, and 300%, respectively, for the sample with the highest PCA content (PVP/PCA 2:1). This change from rigid to ductile behavior is commonly associated with a lower interaction between polymer chains caused by the interference of external molecules. This phenomenon together with the depression of T_g caused by the presence of *p*-coumaric acid, as determined by DSC, are indicative of a clear plasticization of PVP matrix due to the acid.

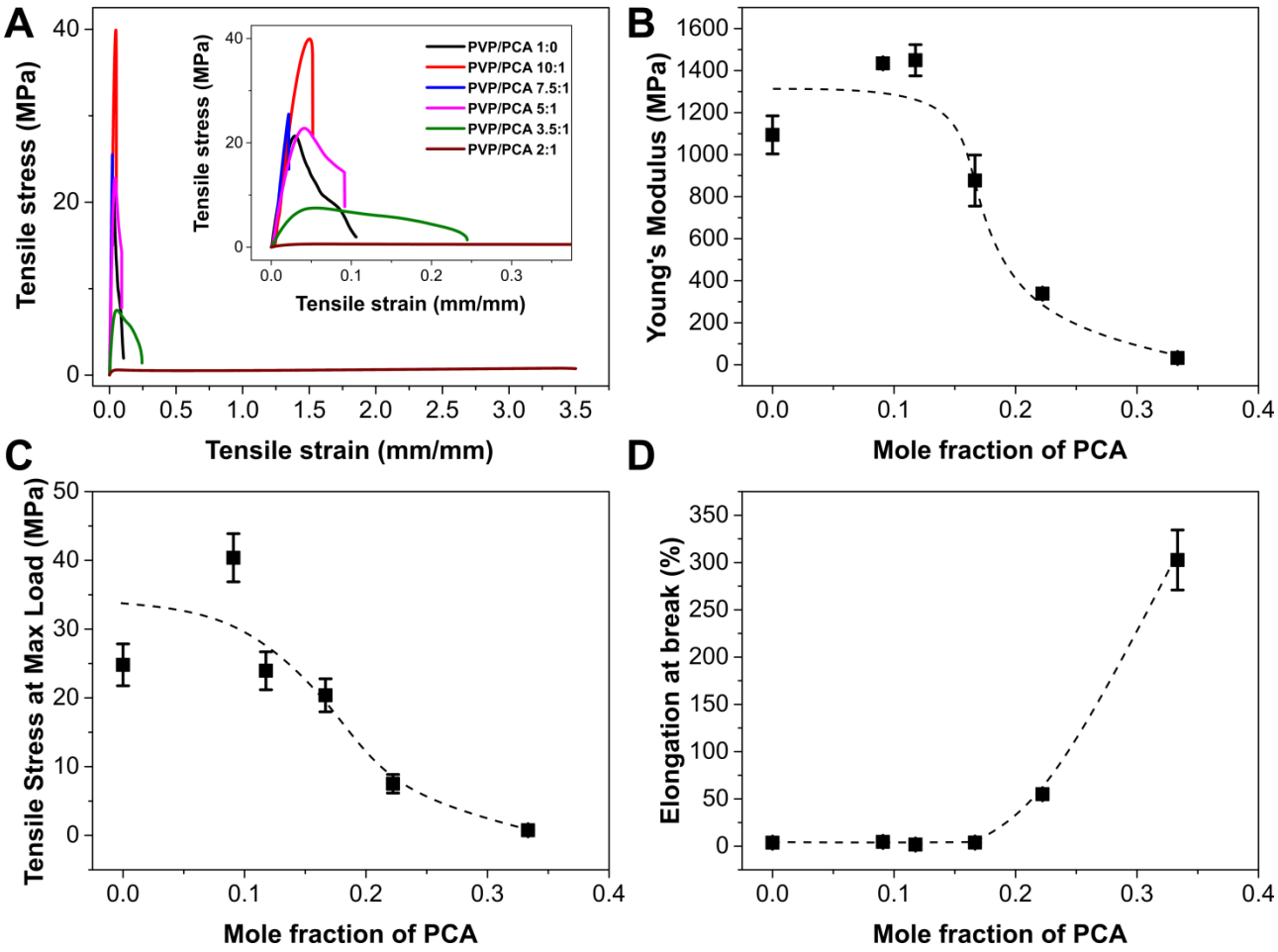

Figure 5.6 A, stress-strain curves of PVP/PCA films. The inset shows a magnification at low strain values. **B**, **C**, **D**, variation of Young's modulus, stress at maximum load, and elongation at break, respectively, with the mole fraction of PCA.

5.3.5 Water uptake, water contact angle, and antioxidant capacity

Figure 5.7A shows the water uptake of PVP/PCA samples at different values of relative humidity. Pure PVP presented the highest increase of weight, while the samples with PCA showed a regular decrease in their capacity to uptake water. This trend was also observed by plotting the values obtained at 100% RH, Figure 5.7B. The water uptake decreased from ~36% for PVP/PCA 1:0 to ~9.5% for PVP/PCA 3.5:1 and, then, slightly was reduced to ~6% for PVP/PCA 2:1. Such a decrease is attributed to the

interaction of *p*-coumaric acid molecules with the polar functional groups of PVP, thus reducing the number of potential anchor points for water. The results of the water contact angle analysis are presented in Figure 5.7C. The wettability depended on the relative proportion of both components. Pure PVP and PVP/PCA 10:1 were hydrophilic with WCA values of 55 and 73°, respectively. For higher PCA contents, the samples become hydrophobic with water contact angles close to 100°. Similarly to water uptake, this phenomenon can be related to a lower presence of available polar groups on the surface due to the interaction between PVP and PCA. Finally, in Figure 5.7D, the antioxidant properties of the films expressed as RSA percentages are reported. As expected, all the films loaded with PCA showed a high antioxidant capacity, reaching 100% RSA after 1 hour, while RSA percentages were very low for pure PVP.

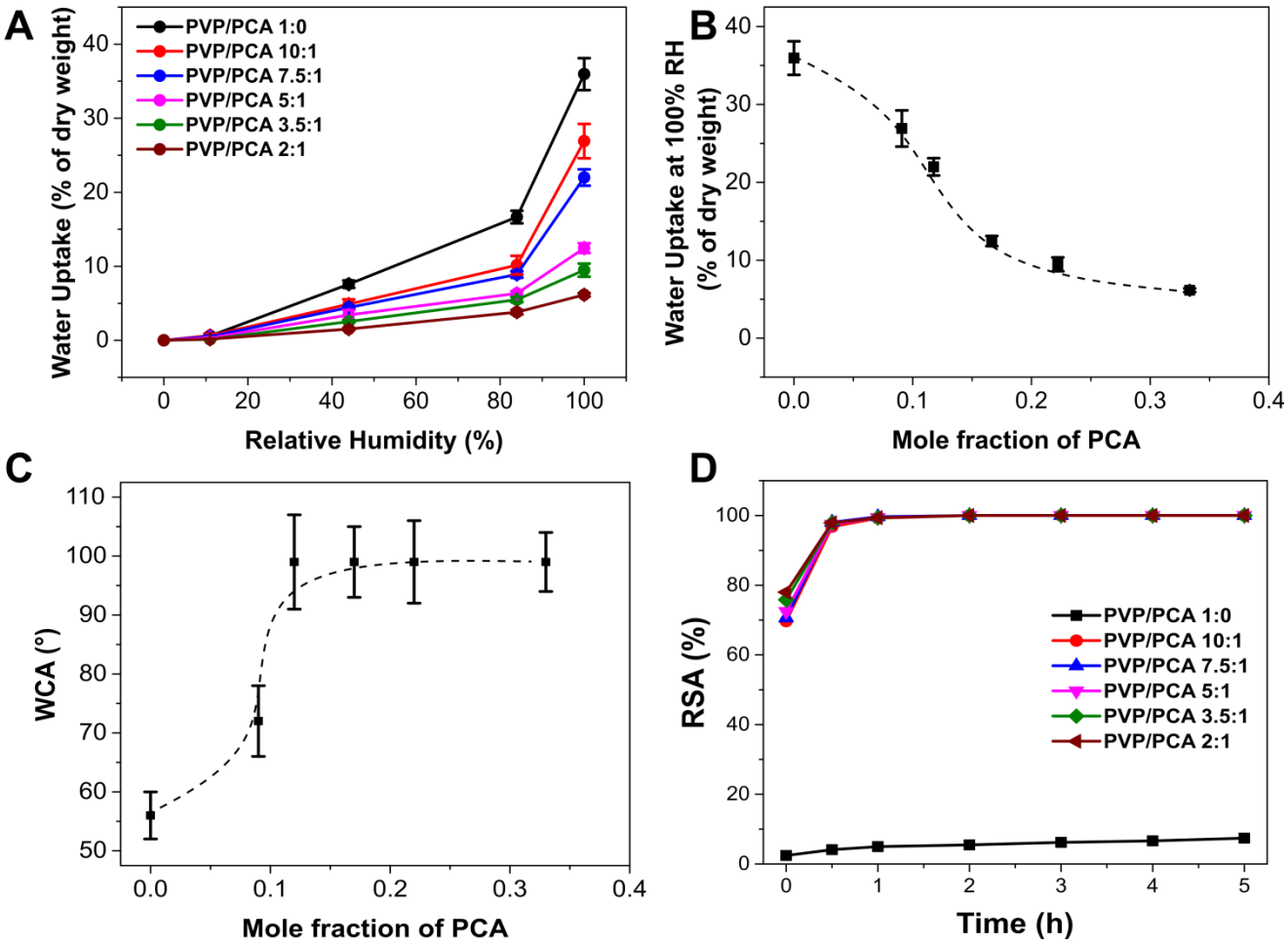

Figure 5.7 A, water uptake of PVP/PCA samples as a function of relative humidity. **B**, values of water uptake of PVP/PCA films at 100% of relative humidity. **C**, variation of water contact angles with the mole fraction of PCA in the films. **D**, radical scavenging activity of PVP/PCA samples as a function of time.

5.3.6 Study of drug release of PCA, MB, and CA

Drug release experiments were carried out to investigate the PCA release from the PVP-based materials and verify the possibility to use the PVP/PCA system for the delivery of other drugs. In Figure 5.8A, the main results of PCA release are displayed and expressed as cumulative percentages. PVP/PCA 10:1 and 7.5:1 samples showed a burst-like release profile, reaching the maximum release of PCA in 2 and 3

hours, respectively. Instead, PVP/PCA 5:1, 3.5:1, and 2:1 films showed a slower release, with maximum releases at 24, 48, and 72 hours respectively. The release during the first 24 hours is shown in Figure 5.8B. At this time, the PCA release from PVP/PCA 5:1, 3.5:1, 2:1 samples was 97%, 83%, and 43%, respectively. As observed, the release was slower as the PCA content was higher.

Figures 5.8C,D shows the release profile of MB and CA, respectively, from PVP/PCA 1:0, 10:1, and 2:1 samples. Pure PVP showed the fastest releases for both drugs, by reaching 99% and 91% of the release for MB and CA, respectively, in 30 minutes. Likewise, the release of the two model drugs from the PVP/PCA 10:1 system was completed in ~2 hours. On the other hand, the release of the model drugs from PVP/PCA 2:1 matrix took much longer. The samples PVP/PCA 2:1 + MB released 93% of the blue dye in 48 hours. Similar behavior was observed for the sample PVP/PCA 2:1 + CA where 89% of the red dye was released in 48 hours. The low releases found in PCA-rich samples can be caused by a high chemical affinity between MB, CA, and PCA. All these molecules have aromatic rings and polar groups that allow the interaction between them by different secondary bonds such as π-π or dipole-dipole interactions and H-bonds [276].

Kinetics data regarding PCA release showed how these release profile fitted with first order kinetics. Moreover, a reduction of the rate constants in the samples with a higher concentration of PCA was observed, see Figure 5.9. Indeed, from the drug release data shown in Figures 5.8A and B the apparent rate constants were calculated, Figure 5.9. The increase of cumulative percentages was empirically best fitted to a $\ln(1-P) = -kt$ first-order kinetic law, where P is the fraction of PCA released at time t and k is the apparent rate constant. As an example, the fittings of PVP/PCA 10:1 and 2:1 are displayed in Figure 5.9A. Rate constants were reduced with the PCA content, ranging from ~1.10 h-1 for PVP/PCA 10:1 to ~0.04 h-1 for PVP/PCA 2:1, Figure 5.9B. An important drop in the value of k was observed between PVP/PCA 7.5:1 and 3.5:1. This phenomenon can be related to a PCA content-dependent formation of H-bonds, as described in the infrared characterization.

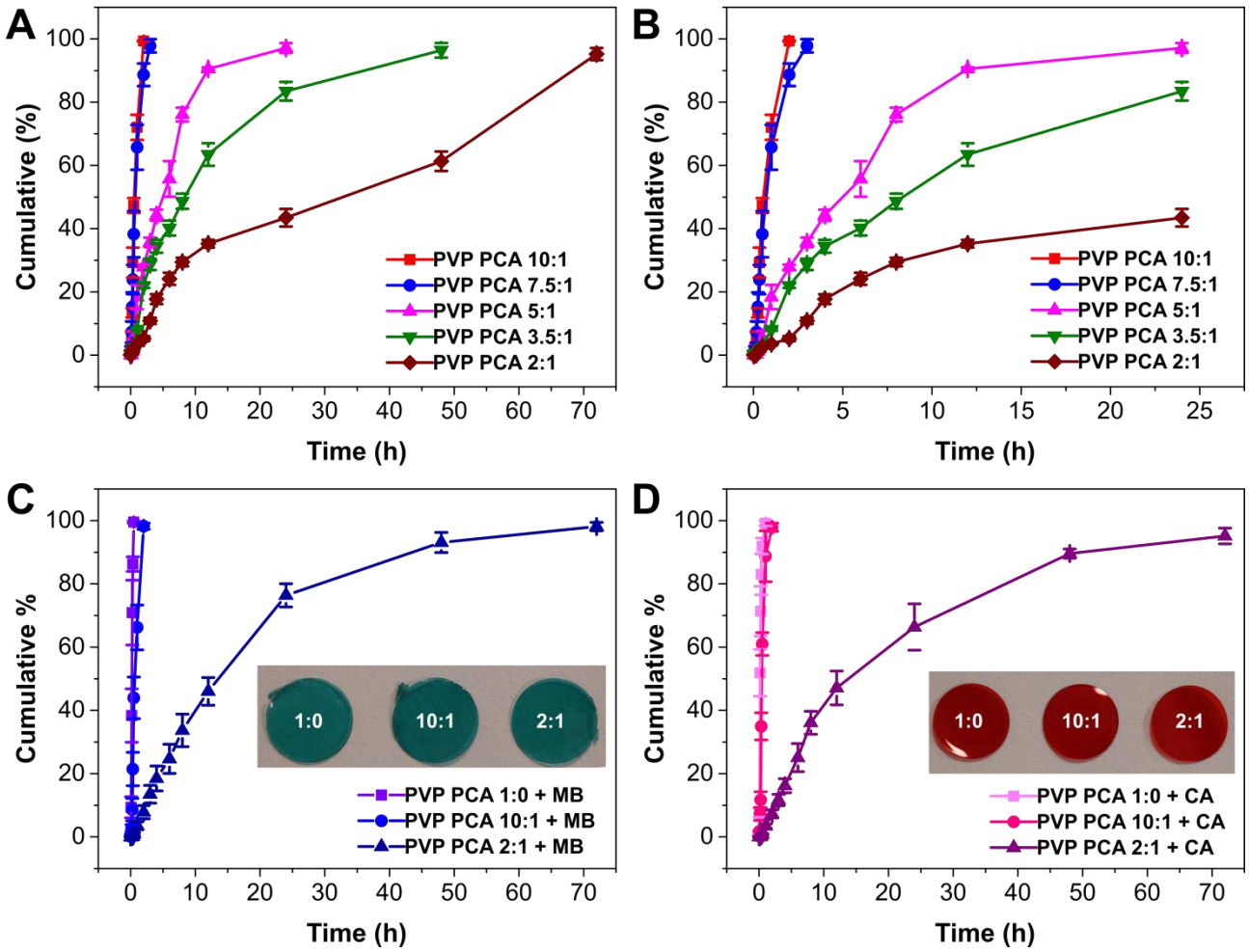

Figure 5.8 A, **B**, release profile of PCA from the different PVP/PCA matrices under investigation over a period of 72 and 24 hours, respectively. **C**, **D**, the release of methylene blue (MB) and carminic acid (CA) from PVP/PCA 1:0, 10:1, and 2:1 systems over a period of 72 hours. Insets show the corresponding photographs of the analyzed materials.

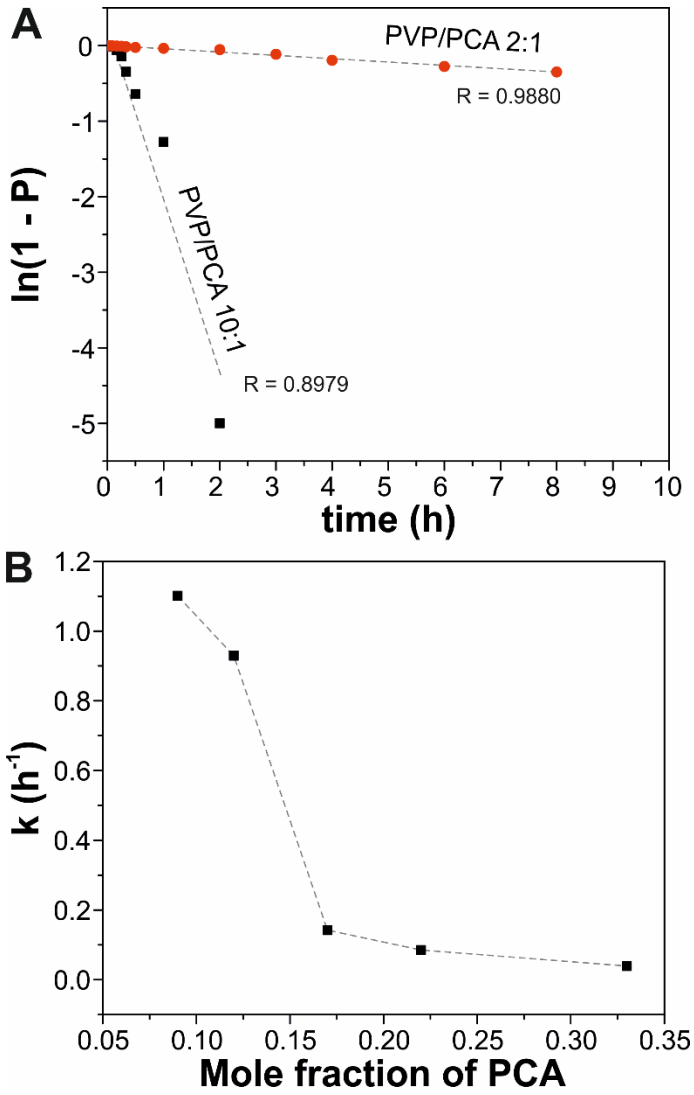

Figure 5.9 A, first-order fitting of drug release experiments for PVP/PCA 10:1 and 2:1. The correlation factor R is included. **B**, calculated kinetic constants as a function of the mole fraction of PCA.

5.3.7 Antibacterial assay

In the hospital environment, among the most common bacterial strains that can cause wound infections are *S. aureus*, and *E. coli* [277]. These strains can strongly affect the healing in terms of time, cost, and compliance of the patients [278, 279]. For this reason, a suitable dressing should be able to ensure a well-disinfected wound bed to improve the healing process. In particular, we investigated the antibacterial properties of PVP/PCA samples against *E.coli* and *S. aureus*. More specifically, PVP/PCA 1:0, 10:1, 5:1, and 2:1 films were placed on LB agar plates with *E.coli* and on blood agar plates with *S. aureus*. After 24 hours of growth, an inhibition growth zone increasing in a dose-dependent manner was formed, as reported in Figure 5.10 and Table 5.2. On the contrary, no inhibition zone was observed in the plates of pure PVP, suggesting that the antibacterial activity occurred due to the PCA release.

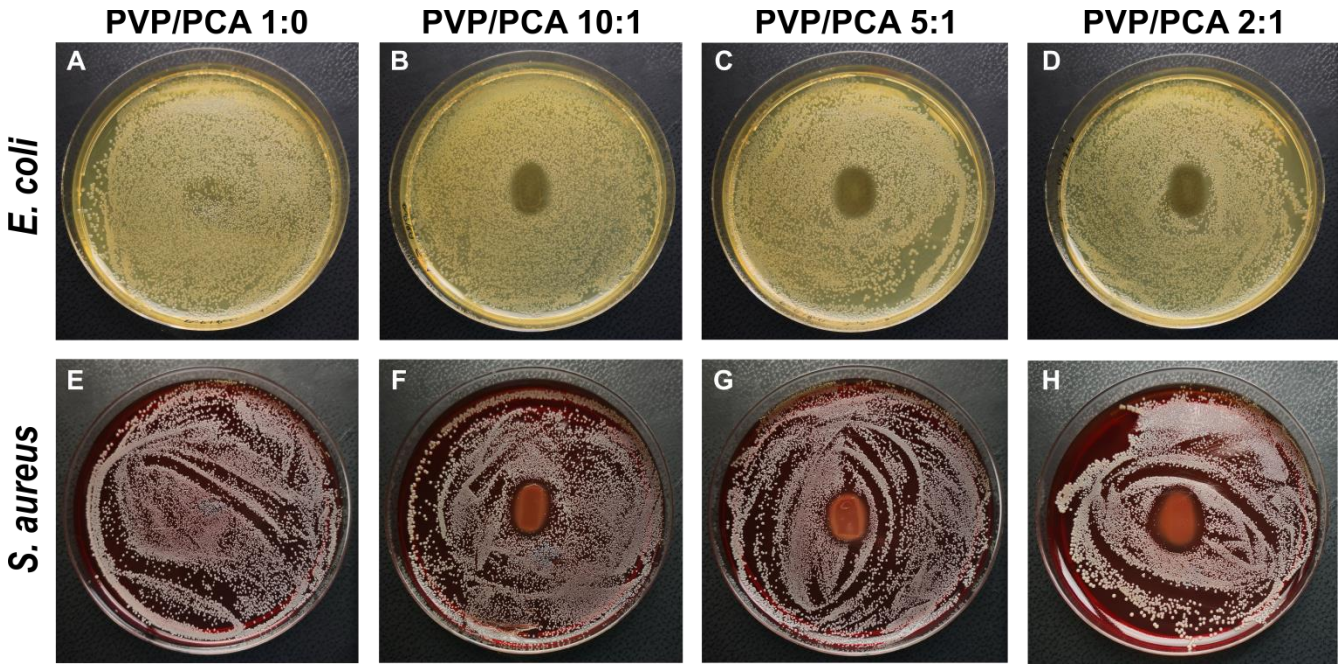

Figure 5.10 The films PVP/PCA 1:0, 10:1, 5:1, 2:1, were tested against *E. coli* (**A-D**) and *S. aureus* (**E-H**), respectively.

PVP/PCA	Inhibition radius for *E. coli*	Inhibition radius for *S. aureus*
1:0	N.D.	N.D.
10:1	0.2 ± 0.1 cm	0.25 ± 0.1 cm
5:1	0.3 ± 0.05 cm	0.35 ± 0.1 cm
2:1	0.4 ± 0.1 cm	0.5 ± 0.05 cm

Table 5.2 Results of antibacterial assays for the PVP/PCA 1:0, 10:1, 5:1, 2:1 samples expressed as a radius of the bacteria-free zone

5.3.8. Mice tests

5.3.8.1. In vivo films application

We evaluated the *in vivo* bio re-sorption and biocompatibility of PVP/PCA films. PVP/PCA film 2:1 and PVP/PCA film 10:1 were applied on the wound and monitored for 48 hours, Figures 11A, B. No adverse signs were observed after the application of both types of films. PVP/PCA 10:1 showed a regular tendency in film degradation and exudate absorption. In the first 4 hours, almost 50% of the starting material was reabsorbed. Six hours after application, PVP/PCA 10:1 film was completely disappeared. On the other hand, PVP/PCA 2:1 film displayed a similar tendency with PVP/PCA 10:1 film in the first two hours. After this time, PVP/PCA 2:1 absorbed exudate and swelled until 6 hours when it started to disappear and was eventually reabsorbed 24 hours after the application. The slower reabsorption of PVP/PCA 2:1 with respect to PVP/PCA 10:1 can ensure the prolonged release of PCA and higher covering time for the wound.

5.3.8.2 MMP-9 measurement by Western blot

Matrix metallopeptidases (MMPs) are present in wounds and are key elements of inflammation, epithelial repair, and resolution: excessive MMPs are a feature of chronic wounds, with patients more prone to infections and ulcers, while regulation of MMP levels could lead to improved wound healing [280, 281]. MMPs expression is very low in normal skin, but their levels increase after injury. In the first phase of wound healing, MMPs are secreted by inflammatory cells and facilities cleaning of wound bed while in the second phase the MMPs play an important role in the formation of new granulation tissue which leads to re-epithelization [282]. Among MMPs, MMP9 is the main regulator and exerts multiple roles during different phases of wound healing [282, 283].In order to verify the activity of PCA, the presence of the metalloproteinase MMP-9, which is normally increased in wounded mice, was investigated [284, 285]. Figure 5.12A shows a high MMP-9 immunoreactivity in the skin of wounded mice of the sham group. The expression of MMP-9 was significantly reduced in mice treated with PVP/PCA 2:1 film, whereas there was no change in expression between sham group and PVP/PCA 10:1 film group, Figures 5.12A and 5.12B. One possible explanation could be that despite PVP PCA 10:1 film is absorbed faster, the amount of *p*-coumaric acid is not enough to develop any anti-inflammatory response. On the other hand, the modulation by PCA/PVP 2:1 sample of MMP-9 activities suggests that it can be useful as an active wound healing material.

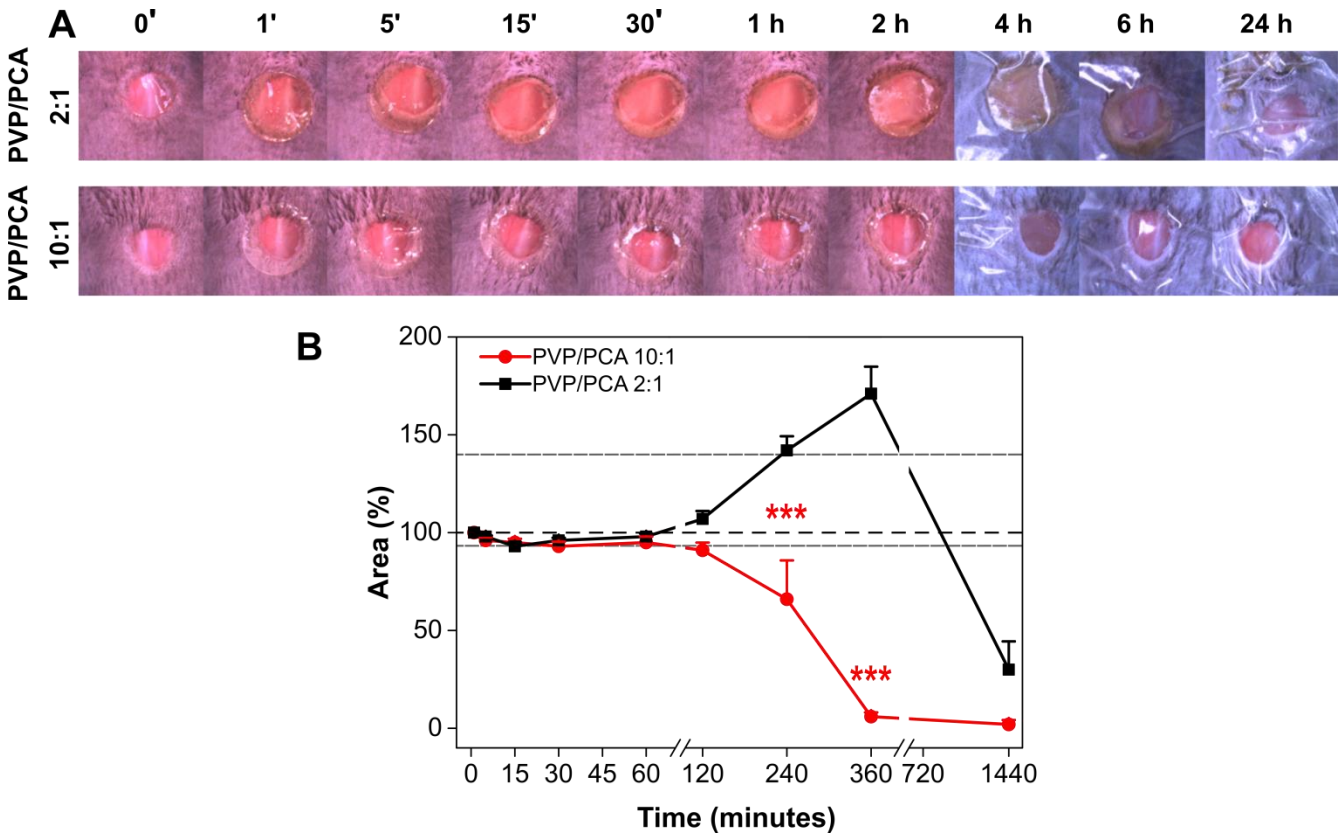

Figure 5.11 A, representative pictures showing different wounds treated with PVP/PCA 2:1 and 10:1 films. **B**, PVP/PCA 2:1 and 10:1 reabsorption profiles percentage as function of time (***$p < 0.0001$, $n = 5$ each group).

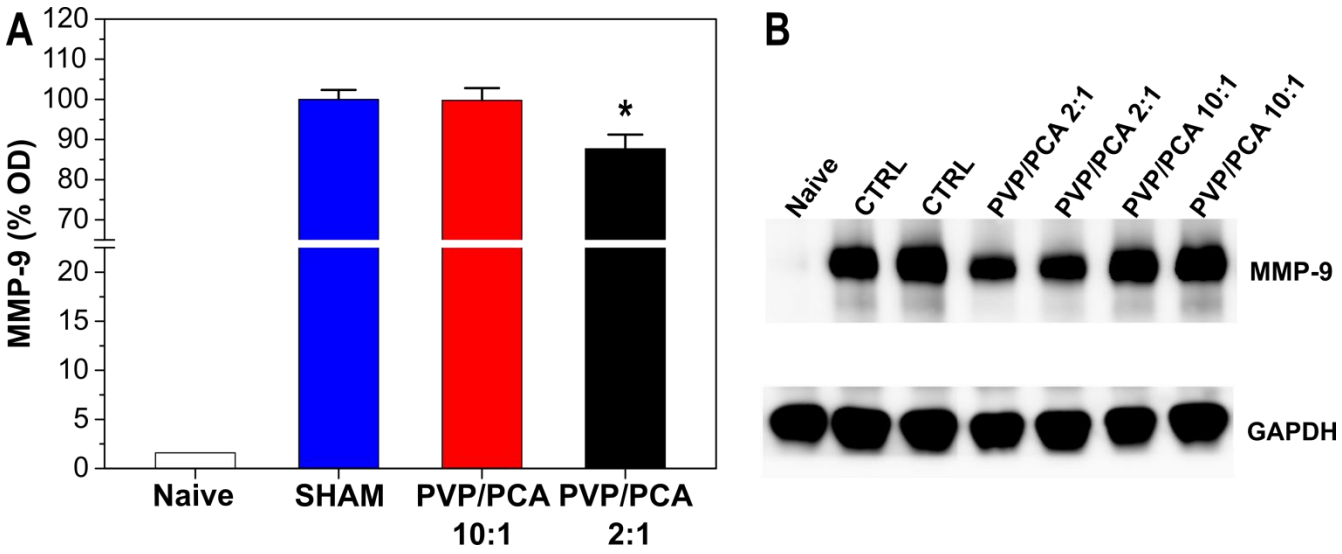

Figure 5.12 A, percentage expression of MMP-9 protein in naïve, sham, PVP/PCA 2:1, and PVP/PCA 10:1 mice. **B**, Western blot analysis of MMP-9 protein in naïve, sham, PVP/PCA 2:1 and PVP/PCA 10:1 mice. The blot is representative of 3 different analyses and illustrates the MMP-9 protein expression in mouse wounded skin. GAPDH was used as internal control. Protein weights are expressed in kDa.

5.4 Conclusions

This chapter showed that significant amounts of a dietary phenolic compound, PCA, can be blended with PVP in ethanol solutions. After drop-casting and evaporation of the solvent, transparent, free-standing films were obtained in the form of miscible solid dispersions, as confirmed by XRD. Both components strongly interacted by H-bonds, originating a new network of these secondary interactions that modified the physical properties of the final materials. Thus, PCA showed a role as a plasticizer reducing the glass transition temperature and changing the mechanical behavior of the biopolymer matrix from rigid to ductile. Resistance to water dissolution was also increased due to the interaction between the polar groups of PVP and the phenolic acid compound, resulting in more hydrophobic and

waterproof materials. In addition, the blends were highly antioxidant because of the presence of PCA, as demonstrated *in vitro*. Moreover, these films showed good antibacterial activity against common pathogens such as *E. coli* and *S. aureus*. On model mice wounds, a reduction of the levels of MMP-9, related to an anti-inflammatory response, was observed in samples with high concentrations of PCA. These results indicate that these biopolymer composites can be promising materials for the treatment of various skin related diseases or cosmetic applications.

Chapter 6 : Conclusions

6.1 Contributions of this thesis

This dissertation has contributed to the area of biomedicine and bioengineering by exploring and studying novel scalable solutions in fabrication and design of PVP-based biomedical devices for treatment of different type of wounds, taking in account all the modern features required for the production of smart and effective wound dressings.

A new formulation for the dispersion of the antibiotic Ciprofloxacin in a matrix of PVP using the acetic acid in the form of transparent and flexible films avoiding crystals formation inside the materials was obtained. A plasticizer effect on the polymer matrix by the Ciprofloxacin and acetic acid was observed. Moreover, electrospun PVP/Cipro/acetic acid-based nanofibers starting from an aqueous solution with a diameter between 250-400 nm were produced. The biocompatibility, the drug release and penetration into the skin, and the antibacterial efficacy against P. aeruginosa of the PVP/Cipro/acetic acid-based films and nanofibers were tested on an infected-wound model based on ex-vivo human skin, resulting in suitable for the treatment of biofilms infected wounds.

A novel multifunctional bilayer construct for the sequential delivery of a local disinfectant, and an antibiotic was produced by scalable water-based methods with the possibility of large size samples preparation. The multifunctional bilayer construct showed self-adhesion to human skin, water absorption capacity, antibacterial activity against three different strains, biocompatibility, no hemolytic effects, and anti-inflammatory properties *in vitro*. Moreover, it was tested in an *in-vivo* full-thickness excisional wound healing mice model, and it can be totally-resorbed by the wound, accelerate the wound closure and reduce the level of cytokines, suggesting that this material can be considered a useful tool in case of burns and chronic wounds.

The facile fabrication of a new bio-composite based on PVP and the phenolic compound *p*-coumaric acid was described. *p*-Coumaric acid strongly affected the PVP properties regarding interaction and dissolution in water, antioxidant activity, and mechanical properties. The PVP/PCA system ensured a

prolonged release not only of the *p*-coumaric acid but also of other model drugs dispersed in the bio-composite. Moreover, the films showed total resorption of the materials and a reduction of the levels of matrix metallopeptidases 9, when tested in an *in-vivo* full-thickness excisional wound healing mice model, indicating a potential application for the treatment of chronic wounds.

6.2 List of conferences, summer schools and publications

6.2.1 Conference:

Oral presentation: Polyvinylpyrrolidone/Ciprofloxacin-based transparent films and electrospun nanofibers as potential wound care dressings; M. Contardi, J. A. Heredia-Guerrero, G. Perotto, P. Valentini, P. P. Pompa, R. Spanò, L. Goldoni, R. Bertorelli, A. Athanassiou, I. S. Bayer. 4th International Conference on Biomedical Polymers and Polymeric Biomaterials, July, 15 – 18, 2018, Krakow, Poland.

Oral Presentation: Transparent Ciprofloxacin-polyvinylpyrrolidone antibiotic films and nanofiber mats as potential skin and wound care dressings; M. Contardi, J. A. Heredia-Guerrero, G. Perotto, P. Valentini, P. P. Pompa, R. Spanò, L. Goldoni, R. Bertorelli, A. Athanassiou, I. S. Bayer. 10th International Conference & Exhibition on Pharmaceutics & Novel Drug Delivery Systems, March 13-15, 2017, London, UK.

6.2.2 Summer Schools:

Ph.D. Summer School on "Drug Delivery" at Danmarks Tekniske Universitet (DTU), August, 13 – 24 , 2018, Copenhagen, Denmark.

Ph.D. Summer School on "43rd Course of International School of Biophysics «Antonio Borsellino»" on "Focus on Methods and Techniques", April, 17-24, 2016, Erice, Italy.

6.2.3 Papers in Journals:

M. Contardi, J. A. Heredia-Guerrero, S. Guzman-Puyol, M. Summa, J. J. Benítez, L. Goldoni, G. Caputo, G. Cusimano, P. Picone, M. Di Carlo, R. Bertorelli, A. Athanassiou, I. S. Bayer; Combining **Dietary Phenolic Antioxidants with Polyvinylpyrrolidone: Transparent Biopolymer Films based on p-Coumaric Acid for Controlled Release**, *Journal of Materials Chemistry B* 2019 (In press) http://dx.doi.org/10.1039/C8TB03017K

M. Contardi, D. Russo, G. Suarato, J. A. Heredia-Guerrero, L. Cesaracciu, I. Penna, N. Margaroli, M. Summa, R. Spanò, G. Tassistro, L. Vezzulli, T. Bandiera, R. Bertorelli, A. Athanassiou, I. S. Bayer; **Polyvinylpyrrolidone/Hyaluronic acid-based Bilayer Constructs for Sequential Delivery of Cutaneous Antiseptic and Antibiotic**, *Chemical Engineering Journal* (2019) 358, 912-923.

M. Contardi, J. A. Heredia-Guerrero, G. Perotto, P. Valentini, P. P. Pompa, R. Spanò, L. Goldoni, R. Bertorelli, A. Athanassiou, I. S. Bayer; **Transparent ciprofloxacin-povidone antibiotic films and nanofiber mats as potential skin and wound care dressings**, *European Journal of Pharmaceutical Sciences* (2017) 104, 133-144.

6.3 Recommendations for future work

In an attempt to further evaluate PVP-based materials for controlled release and wound treatment the following are potentially valuable suggestions for future work. PVP-Cipro-acetic acid films could test in the infected ex-vivo human-skin model against S. aureus or a polymicrobial infection. The accelerated wound closure mediated by the bilayer construct could be evaluated with histological analysis. Moreover, the anti-inflammatory activity of this material could also be evaluated and characterized by a burn mice model. Finally, the wound closure rate of the PVP/PCA could be tested to better investigate the potential application of this biocomposite in the wound healing field.

References

[1] F. Haaf, A. Sanner, F. Straub, Polymers of N-vinylpyrrolidone: synthesis, characterization and uses, Polymer Journal 17(1) (1985) 143-152.
[2] V. Bühler, Kollidon, Polyvinylpyrrolidone excipients for the pharmaceutical industry 9 (2008).
[3] H. Folttmann, A. Quadir, Polyvinylpyrrolidone (PVP)—one of the most widely used excipients in pharmaceuticals: an overview, Drug Deliv Technol 8(6) (2008) 22-27.
[4] K. Halake, M. Birajdar, B.S. Kim, H. Bae, C. Lee, Y.J. Kim, S. Kim, H.J. Kim, S. Ahn, S.Y. An, Recent application developments of water-soluble synthetic polymers, Journal of Industrial and Engineering Chemistry 20(6) (2014) 3913-3918.
[5] A. Slistan-Grijalva, R. Herrera-Urbina, J. Rivas-Silva, M. Avalos-Borja, F. Castillón-Barraza, A. Posada-Amarillas, Synthesis of silver nanoparticles in a polyvinylpyrrolidone (PVP) paste, and their optical properties in a film and in ethylene glycol, Materials Research Bulletin 43(1) (2008) 90-96.
[6] J. Rodríguez, E. Navarrete, E.A. Dalchiele, L. Sánchez, J.R. Ramos-Barrado, F. Martín, Polyvinylpyrrolidone–LiClO4 solid polymer electrolyte and its application in transparent thin film supercapacitors, Journal of Power Sources 237 (2013) 270-276.
[7] Y. Hida, H. Kozuka, Photoanodic properties of sol–gel-derived iron oxide thin films with embedded gold nanoparticles: effects of polyvinylpyrrolidone in coating solutions, Thin Solid Films 476(2) (2005) 264-271.
[8] L.Y. Lafreniere, F.D. Talbot, T. Matsuura, S. Sourirajan, Effect of poly (vinylpyrrolidone) additive on the performance of poly (ether sulfone) ultrafiltration membranes, Industrial & engineering chemistry research 26(11) (1987) 2385-2389.
[9] M. Schulz, B. Fussnegger, R. Bodmeier, Drug release and adhesive properties of crospovidone-containing matrix patches based on polyisobutene and acrylic adhesives, European journal of pharmaceutical sciences 41(5) (2010) 675-684.
[10] J.-M. Séquaris, A. Hild, H. Narres, M. Schwuger, Polyvinylpyrrolidone adsorption on Na-montmorillonite. Effect of the polymer interfacial conformation on the colloidal behavior and binding of chemicals, Journal of colloid and interface science 230(1) (2000) 73-83.
[11] Y.-P. Luo, Y.-B. Zhao, S. Liu, Evaluation of DFO/PVP and its application to latent fingermarks development on thermal paper, Forensic science international 229(1-3) (2013) 75-79.
[12] S.L. Kopolow, D. Patel, Y.T. Kwak, M. Tallon, D.K. Hood, L. Senak, J.M. Kittrick, Substrate for color inkjet printing, Google Patents, 2003.
[13] T. Schmidt, J.I. Mönch, K.F. Arndt, Temperature-Sensitive Hydrogel Pattern by Electron-Beam Lithography, Macromolecular Materials and Engineering 291(7) (2006) 755-761.
[14] A.P.S. Immich, P.H.H. de Araujo, L.H. Catalani, S.M.G.U. de Souza, A.A.U. de Souza, Coating of cotton yarn with poly (vinyl alcohol) and poly (N-vinyl-2-pyrrolidone) crosslinked via ultraviolet radiation, Journal of Applied Polymer Science 119(5) (2011) 2560-2567.
[15] V.N. Morozov, A.Y. Mikheev, Water-soluble polyvinylpyrrolidone nanofilters manufactured by electrospray-neutralization technique, Journal of membrane science 403 (2012) 110-120.
[16] A. Alpatova, E.-S. Kim, X. Sun, G. Hwang, Y. Liu, M.G. El-Din, Fabrication of porous polymeric nanocomposite membranes with enhanced anti-fouling properties: Effect of casting composition, Journal of membrane science 444 (2013) 449-460.

[17] D.Y. Koseoglu-Imer, The determination of performances of polysulfone (PS) ultrafiltration membranes fabricated at different evaporation temperatures for the pretreatment of textile wastewater, Desalination 316 (2013) 110-119.
[18] W. Schwarz, PVP: a critical review of the kinetics and toxicology of polyvinylpyrrolidone (povidone), CRC Press1990.
[19] M.Y. Kariduraganavar, A.A. Kittur, R.R. Kamble, Polymer synthesis and processing, Natural and Synthetic Biomedical Polymers, Elsevier2014, pp. 1-31.
[20] W. Sneader, Drug discovery: a history, John Wiley & Sons2005.
[21] Y. Park, J. Park, G.S. Chu, K.S. Kim, J.H. Sung, B. Kim, Transdermal delivery of cosmetic ingredients using dissolving polymer microneedle arrays, Biotechnology and Bioprocess Engineering 20(3) (2015) 543-549.
[22] B. Nair, Final report on the safety assessment of polyvinylpyrrolidone (PVP), International journal of toxicology 17(4_suppl) (1998) 95-130.
[23] F. Yanez, A. Concheiro, C. Alvarez-Lorenzo, Macromolecule release and smoothness of semi-interpenetrating PVP–pHEMA networks for comfortable soft contact lenses, European Journal of Pharmaceutics and Biopharmaceutics 69(3) (2008) 1094-1103.
[24] M.T. Marın, M.V. Margarit, G.E. Salcedo, Characterization and solubility study of solid dispersions of flunarizine and polyvinylpyrrolidone, Il Farmaco 57(9) (2002) 723-727.
[25] N. Kaewnopparat, S. Kaewnopparat, A. Jangwang, D. Maneenaun, T. Chuchome, P. Panichayupakaranant, Increased solubility, dissolution and physicochemical studies of curcumin-polyvinylpyrrolidone K-30 solid dispersions, World academy of science, engineering and technology 55 (2009) 229-234.
[26] G. Van den Mooter, M. Wuyts, N. Blaton, R. Busson, P. Grobet, P. Augustijns, R. Kinget, Physical stabilisation of amorphous ketoconazole in solid dispersions with polyvinylpyrrolidone K25, European journal of pharmaceutical sciences 12(3) (2001) 261-269.
[27] C. Mora-Huertas, H. Fessi, A. Elaissari, Polymer-based nanocapsules for drug delivery, International journal of pharmaceutics 385(1-2) (2010) 113-142.
[28] A. Saroj, R. Singh, S. Chandra, Studies on polymer electrolyte poly (vinyl) pyrrolidone (PVP) complexed with ionic liquid: effect of complexation on thermal stability, conductivity and relaxation behaviour, Materials Science and Engineering: B 178(4) (2013) 231-238.
[29] M.-K. Chun, C.-S. Cho, H.-K. Choi, Mucoadhesive drug carrier based on interpolymer complex of poly (vinyl pyrrolidone) and poly (acrylic acid) prepared by template polymerization, Journal of controlled release 81(3) (2002) 327-334.
[30] H. Shelanski, PVP-iodine: history, toxicity and therapeutic uses, J. Inter. College of Surgeons (1956).
[31] D. Michel, G. Zäch, Antiseptic efficacy of disinfecting solutions in suspension test in vitro against methicillin-resistant Staphylococcus aureus, Pseudomonas aeruginosa and Escherichia coli in pressure sore wounds after spinal cord injury, Dermatology 195(Suppl. 2) (1997) 36-41.
[32] I. Liakos, L. Rizzello, I.S. Bayer, P.P. Pompa, R. Cingolani, A. Athanassiou, Controlled antiseptic release by alginate polymer films and beads, Carbohydrate polymers 92(1) (2013) 176-183.
[33] M. Summa, I. Bayer, I. Liakos, T. Bandiera, A. Athanassiou, R. Bertorelli, In Vivo Characterization Of The Alginate-povidone Iodine Film In The Wound Healing Model In Mice, Wound Repair and Regeneration 23(4) (2015) A29.
[34] S.G. Priya, A. Gupta, E. Jain, J. Sarkar, A. Damania, P.R. Jagdale, B.P. Chaudhari, K.C. Gupta, A. Kumar, Bilayer cryogel wound dressing and skin regeneration grafts for the treatment of acute skin wounds, ACS applied materials & interfaces 8(24) (2016) 15145-15159.

[35] C.F. Rawlinson, A.C. Williams, P. Timmins, I. Grimsey, Polymer-mediated disruption of drug crystallinity, International journal of pharmaceutics 336(1) (2007) 42-48.
[36] P. Jain, A.K. Banga, Inhibition of crystallization in drug-in-adhesive-type transdermal patches, International journal of pharmaceutics 394(1-2) (2010) 68-74.
[37] L.S. Taylor, G. Zografi, Spectroscopic characterization of interactions between PVP and indomethacin in amorphous molecular dispersions, Pharmaceutical research 14(12) (1997) 1691-1698.
[38] P. Nagar, I. Chauhan, M. Yasir, Insights into Polymers: Film Formers in Mouth Dissolving Films, Drug Invention Today 3(12) (2011).
[39] S. Ali, A. Quadir, High molecular weight povidone polymer-based films for fast dissolving drug delivery applications, Drug Delivery Technology 7(6) (2007) 36-43.
[40] T.-y. Song, C. Yao, X.-s. Li, Electrospinning of zein/chitosan composite fibrous membranes, Chinese Journal of Polymer Science 28(2) (2010) 171-179.
[41] A. Raizada, A. Bandari, B. Kumar, Polymers in drug delivery: a review, Int. J. Pharm. Res. Dev 2(8) (2010) 9-20.
[42] S. Benamer, M. Mahlous, A. Boukrif, B. Mansouri, S.L. Youcef, Synthesis and characterisation of hydrogels based on poly (vinyl pyrrolidone), Nuclear Instruments and Methods in Physics Research Section B: Beam Interactions with Materials and Atoms 248(2) (2006) 284-290.
[43] L.C. Lopérgolo, A.B. Lugao, L.H. Catalani, Direct UV photocrosslinking of poly (N-vinyl-2-pyrrolidone)(PVP) to produce hydrogels, Polymer 44(20) (2003) 6217-6222.
[44] G. Fechine, J. Barros, M. Alcântara, L. Catalani, Fluorescence polarization and rheological studies of the poly (N-vinyl-2-pyrrolidone) hydrogels produced by UV radiation, Polymer 47(8) (2006) 2629-2633.
[45] G.J.M. Fechine, J.A.G. Barros, L.H. Catalani, Poly (N-vinyl-2-pyrrolidone) hydrogel production by ultraviolet radiation: new methodologies to accelerate crosslinking, Polymer 45(14) (2004) 4705-4709.
[46] A. Henglein, Crosslinking of polymers in solution under the influence of gamma radiation, The Journal of Physical Chemistry 63(11) (1959) 1852-1858.
[47] S. Kadłubowski, A. Henke, P. Ulański, J.M. Rosiak, L. Bromberg, T.A. Hatton, Hydrogels of polyvinylpyrrolidone (PVP) and poly (acrylic acid)(PAA) synthesized by photoinduced crosslinking of homopolymers, Polymer 48(17) (2007) 4974-4981.
[48] R. Ma, D. Xiong, F. Miao, J. Zhang, Y. Peng, Novel PVP/PVA hydrogels for articular cartilage replacement, Materials Science and Engineering: C 29(6) (2009) 1979-1983.
[49] M.T. Razzak, S. Dewi, H. Lely, E. Taty, The characterization of dressing component materials and radiation formation of PVA–PVP hydrogel, Radiation Physics and Chemistry 55(2) (1999) 153-165.
[50] H. Yu, X. Xu, X. Chen, J. Hao, X. Jing, Medicated wound dressings based on poly (vinyl alcohol)/poly (N-vinyl pyrrolidone)/chitosan hydrogels, Journal of Applied Polymer Science 101(4) (2006) 2453-2463.
[51] A. Leiva, C. Saldías, C. Quezada, A. Toro-Labbé, F.J. Espinoza-Beltrán, M. Urzúa, L. Gargallo, D. Radic, Gold-copolymer nanoparticles: Poly (ε-caprolactone)/poly (N-vinyl-2-pyrrolydone) Biodegradable triblock copolymer as stabilizer and reductant, European Polymer Journal 45(11) (2009) 3035-3042.
[52] R. Singh, D. Singh, Radiation synthesis of PVP/alginate hydrogel containing nanosilver as wound dressing, Journal of Materials Science: Materials in Medicine 23(11) (2012) 2649-2658.
[53] M. Wu, B. Bao, F. Yoshii, K. Makuuchi, Irradiation of crosslinked, poly (vinyl alcohol) blended hydrogel for wound dressing, Journal of Radioanalytical and Nuclear Chemistry 250(2) (2001) 391-395.

[54] L.L. Alberto E Panerai, Mauro Ferrari, Michela Bagnasco, A new ketoprofen lysine salt formulation: 40 mg orodispersible granules, Trends in Medicine 12(4) (2012) 159-167.
[55] N. Høiby, T. Bjarnsholt, M. Givskov, S. Molin, O. Ciofu, Antibiotic resistance of bacterial biofilms, International journal of antimicrobial agents 35(4) (2010) 322-332.
[56] H. Wu, C. Moser, H.-Z. Wang, N. Høiby, Z.-J. Song, Strategies for combating bacterial biofilm infections, International journal of oral science 7(1) (2015) 1.
[57] S. Banerjee, P. Chattopadhyay, A. Ghosh, P. Datta, V. Veer, Aspect of adhesives in transdermal drug delivery systems, International Journal of Adhesion and Adhesives 50 (2014) 70-84.
[58] L.G. Ovington, Advances in wound dressings, Clinics in dermatology 25(1) (2007) 33-38.
[59] A. Athanassiou, D. Fragouli, I. Bayer, P. Netti, L. Rizzello, P.P. Pompa, Soft Matter Composites Interfacing with Biomolecules, Cells, and Tissues, Bioinspired Approaches for Human-Centric Technologies, Springer2014, pp. 29-76.
[60] J.S. Boateng, K.H. Matthews, H.N.E. Stevens, G.M. Eccleston, Wound Healing Dressings and Drug Delivery Systems: A Review, Journal of Pharmaceutical Sciences 97(8) (2008) 2892-2923.
[61] D. Simões, S.P. Miguel, M.P. Ribeiro, P. Coutinho, A.G. Mendonça, I.J. Correia, Recent advances on antimicrobial wound dressing: A review, European Journal of Pharmaceutics and Biopharmaceutics (2018).
[62] L.J. Borda, F.E. Macquhae, R.S. Kirsner, Wound Dressings: A Comprehensive Review, Current Dermatology Reports 5(4) (2016) 287-297.
[63] R.F. Pereira, C.C. Barrias, P.L. Granja, P.J. Bartolo, Advanced biofabrication strategies for skin regeneration and repair, Nanomedicine 8(4) (2013) 603-621.
[64] S. Ali, S. Koul, M. Memon, T. Pasha, S. Afghan, F. Tahir, Comparison of chlorhexidine based dressing versus simple occlusive dressing in preventing catheter related bloodstream infections at medical ICU in a resource constraint settings, Intensive care medicine experimental 3(1) (2015) A812.
[65] B. Ramesh, B. Jayalakshmi, J. Mohan, A comparative study of collagen dressing versus petrolatum gauze dressing in reducing pain at the donor area, Journal of cutaneous and aesthetic surgery 10(1) (2017) 18.
[66] I. Wright, Racecourse fracture management. Part 2: Techniques for temporary immobilisation and transport, Equine Veterinary Education 29(8) (2017) 440-451.
[67] Y. Hu, P. Yan, L. Fu, Y. Zheng, W. Kong, H. Wu, X. Yu, Polyvinyl Alcohol/Polyvinyl Pyrrolidone Crosslinked Hydrogels Induce Wound Healing Through Cell Proliferation and Migration, Journal of Biomaterials and Tissue Engineering 7(4) (2017) 310-318.
[68] A.S. Ahmed, U.K. Mandal, M. Taher, D. Susanti, J.M. Jaffri, PVA-PEG physically cross-linked hydrogel film as a wound dressing: Experimental design and optimization, Pharmaceutical Development and Technology (2017) 1-10.
[69] E.A. Kamoun, E.-R.S. Kenawy, X. Chen, A review on polymeric hydrogel membranes for wound dressing applications: PVA-based hydrogel dressings, Journal of advanced research (2017).
[70] A.J. Quarfoot, P.H. Hyla, D. Patience, Hydrogel wound dressing, Google Patents, 1990.
[71] G.D. Mogoşanu, A.M. Grumezescu, Natural and synthetic polymers for wounds and burns dressing, International journal of pharmaceutics 463(2) (2014) 127-136.
[72] B. Gupta, R. Agarwal, M.S. Alam, Textile-based smart wound dressings, Indian J. Fibre Text. Tes. 35(2) (2010) 174-187.
[73] W. Paul, C.P. Sharma, Chitosan and alginate wound dressings: a short review, Trends Biomater Artif Organs 18(1) (2004) 18-23.
[74] C.J. Doillon, F.H. Silver, Collagen-based wound dressing: Effects of hyaluronic acid and firponectin on wound healing, Biomaterials 7(1) (1986) 3-8.

[75] J. Fraser, T. Laurent, U. Laurent, Hyaluronan: its nature, distribution, functions and turnover, Journal of internal medicine 242(1) (1997) 27-33.
[76] Y. Matsumoto, Y. Kuroyanagi, Development of a wound dressing composed of hyaluronic acid sponge containing arginine and epidermal growth factor, Journal of Biomaterials Science, Polymer Edition 21(6-7) (2010) 715-726.
[77] R. Jayakumar, M. Prabaharan, P.S. Kumar, S. Nair, H. Tamura, Biomaterials based on chitin and chitosan in wound dressing applications, Biotechnology advances 29(3) (2011) 322-337.
[78] S.-Y. Ong, J. Wu, S.M. Moochhala, M.-H. Tan, J. Lu, Development of a chitosan-based wound dressing with improved hemostatic and antimicrobial properties, Biomaterials 29(32) (2008) 4323-4332.
[79] B.-M. Min, G. Lee, S.H. Kim, Y.S. Nam, T.S. Lee, W.H. Park, Electrospinning of silk fibroin nanofibers and its effect on the adhesion and spreading of normal human keratinocytes and fibroblasts in vitro, Biomaterials 25(7) (2004) 1289-1297.
[80] A. Vasconcelos, A.C. Gomes, A. Cavaco-Paulo, Novel silk fibroin/elastin wound dressings, Acta biomaterialia 8(8) (2012) 3049-3060.
[81] G. Navarra, C. Peres, M. Contardi, P. Picone, P.L. San Biagio, M. Di Carlo, D. Giacomazza, V. Militello, Heat-and pH-induced BSA conformational changes, hydrogel formation and application as 3D cell scaffold, Archives of biochemistry and biophysics 606 (2016) 134-142.
[82] P. Picone, G. Navarra, C. Peres, M. Contardi, P.L. San Biagio, M. Di Carlo, D. Giacomazza, V. Militello, Data concerning the proteolytic resistance and oxidative stress in LAN5 cells after treatment with BSA hydrogels, Data in brief 9 (2016) 324-327.
[83] H. Hajiali, M. Summa, D. Russo, A. Armirotti, V. Brunetti, R. Bertorelli, A. Athanassiou, E. Mele, Alginate–lavender nanofibers with antibacterial and anti-inflammatory activity to effectively promote burn healing, Journal of Materials Chemistry B 4(9) (2016) 1686-1695.
[84] D. Kaiser, J. Hafner, D. Mayer, L.E. French, S. Läuchli, Alginate dressing and polyurethane film versus paraffin gauze in the treatment of split-thickness skin graft donor sites: a randomized controlled pilot study, Advances in skin & wound care 26(2) (2013) 67-73.
[85] F.S. Palumbo, S. Agnello, C. Fiorica, G. Pitarresi, R. Puleio, G.R. Loria, G. Giammona, Spray dried hyaluronic acid microparticles for adhesion controlled aggregation and potential stimulation of stem cells, International journal of pharmaceutics 519(1) (2017) 332-342.
[86] S. Thinda, H.V. Wright, L.A. Mawn, Integra bilayer matrix wound dressing closure of large periorbital traumatic wound, Archives of Ophthalmology 130(2) (2012) 217-219.
[87] I.S. Whitaker, S. Prowse, T.S. Potokar, A critical evaluation of the use of Biobrane as a biologic skin substitute: a versatile tool for the plastic and reconstructive surgeon, Annals of plastic surgery 60(3) (2008) 333-337.
[88] H. Amani, W.R. Dougherty, S. Blome-Eberwein, Use of Transcyte® and dermabrasion to treat burns reduces length of stay in burns of all size and etiology, Burns 32(7) (2006) 828-832.
[89] S.J. Mohd Yussof, A.S. Halim, A.Z. Mat Saad, H. Jaafar, Evaluation of the biocompatibility of a bilayer chitosan skin regenerating template, human skin allograft, and integra implants in rats, ISRN Materials Science 2011 (2011).
[90] S. Zhong, Y. Zhang, C. Lim, Tissue scaffolds for skin wound healing and dermal reconstruction, Wiley Interdisciplinary Reviews: Nanomedicine and Nanobiotechnology 2(5) (2010) 510-525.
[91] S. Dhivya, V.V. Padma, E. Santhini, Wound dressings–a review, BioMedicine 5(4) (2015).
[92] L.I. Moura, A.M. Dias, E. Carvalho, H.C. de Sousa, Recent advances on the development of wound dressings for diabetic foot ulcer treatment—a review, Acta biomaterialia 9(7) (2013) 7093-7114.

[93] S.F. Badylak, D.O. Freytes, T.W. Gilbert, Extracellular matrix as a biological scaffold material: structure and function, Acta biomaterialia 5(1) (2009) 1-13.
[94] P.X. Ma, Biomimetic materials for tissue engineering, Advanced drug delivery reviews 60(2) (2008) 184-198.
[95] T.K. Dash, V.B. Konkimalla, Poly-ϵ-caprolactone based formulations for drug delivery and tissue engineering: A review, Journal of Controlled Release 158(1) (2012) 15-33.
[96] S. Ramakrishna, K. Fujihara, W.-E. Teo, T. Yong, Z. Ma, R. Ramaseshan, Electrospun nanofibers: solving global issues, Materials today 9(3) (2006) 40-50.
[97] A.L. Yarin, S. Koombhongse, D.H. Reneker, Taylor cone and jetting from liquid droplets in electrospinning of nanofibers, Journal of applied physics 90(9) (2001) 4836-4846.
[98] G.C. Rutledge, S.V. Fridrikh, Formation of fibers by electrospinning, Advanced Drug Delivery Reviews 59(14) (2007) 1384-1391.
[99] R. Xu, H. Xia, W. He, Z. Li, J. Zhao, B. Liu, Y. Wang, Q. Lei, Y. Kong, Y. Bai, Controlled water vapor transmission rate promotes wound-healing via wound re-epithelialization and contraction enhancement, Scientific reports 6 (2016) 24596.
[100] K.A. Rieger, N.P. Birch, J.D. Schiffman, Designing electrospun nanofiber mats to promote wound healing–a review, Journal of Materials Chemistry B 1(36) (2013) 4531-4541.
[101] J.H. Jeong, C.Y. Lee, D.K. Chung, Probiotic lactic acid bacteria and skin health, Critical reviews in food science and nutrition 56(14) (2016) 2331-2337.
[102] V. Nizet, T. Ohtake, X. Lauth, J. Trowbridge, J. Rudisill, R.A. Dorschner, V. Pestonjamasp, J. Piraino, K. Huttner, R.L. Gallo, Innate antimicrobial peptide protects the skin from invasive bacterial infection, Nature 414(6862) (2001) 454.
[103] J. Wiesner, A. Vilcinskas, Antimicrobial peptides: the ancient arm of the human immune system, Virulence 1(5) (2010) 440-464.
[104] R. Clark, A. Singer, Wound repair: basic biology to tissue engineering, Principles of tissue engineering 2 (2000) 855-78.
[105] R.A.F. Clark, Chapter 76 - Wound Repair: Basic Biology to Tissue Engineering A2 - Lanza, Robert, in: R. Langer, J. Vacanti (Eds.), Principles of Tissue Engineering (Fourth Edition), Academic Press, Boston, 2014, pp. 1595-1617.
[106] N.X. Landén, D. Li, M. Ståhle, Transition from inflammation to proliferation: a critical step during wound healing, Cellular and Molecular Life Sciences 73(20) (2016) 3861-3885.
[107] G.C. Gurtner, S. Werner, Y. Barrandon, M.T. Longaker, Wound repair and regeneration, Nature 453(7193) (2008) 314-321.
[108] R.A. Clark, The molecular and cellular biology of wound repair, Springer Science & Business Media2013.
[109] R. Grose, S. Werner, Wound-healing studies in transgenic and knockout mice, Molecular biotechnology 28(2) (2004) 147.
[110] R. Goldman, Growth factors and chronic wound healing: past, present, and future, Advances in skin & wound care 17(1) (2004) 24-35.
[111] M. Xue, C.J. Jackson, Extracellular matrix reorganization during wound healing and its impact on abnormal scarring, Advances in wound care 4(3) (2015) 119-136.
[112] R. Clark, M.G. Tonnesen, J. Gailit, D.A. Cheresh, Transient functional expression of alphaVbeta 3 on vascular cells during wound repair, The American journal of pathology 148(5) (1996) 1407.
[113] P. Martin, S.J. Leibovich, Inflammatory cells during wound repair: the good, the bad and the ugly, Trends in cell biology 15(11) (2005) 599-607.

[114] G.S. Ashcroft, X. Yang, A.B. Glick, M. Weinstein, J.J. Letterio, D.E. Mizel, M. Anzano, T. Greenwell-Wild, S.M. Wahl, C. Deng, Mice lacking Smad3 show accelerated wound healing and an impaired local inflammatory response, Nature cell biology 1(5) (1999) 260.
[115] P. Martin, D. D'Souza, J. Martin, R. Grose, L. Cooper, R. Maki, S.R. McKercher, Wound healing in the PU. 1 null mouse—tissue repair is not dependent on inflammatory cells, Current Biology 13(13) (2003) 1122-1128.
[116] M.G. Tonnesen, X. Feng, R.A. Clark, Angiogenesis in wound healing, Journal of Investigative Dermatology Symposium Proceedings, Elsevier, 2000, pp. 40-46.
[117] S. Werner, R. Grose, Regulation of wound healing by growth factors and cytokines, Physiological reviews 83(3) (2003) 835-870.
[118] S. Werner, T. Krieg, H. Smola, Keratinocyte–fibroblast interactions in wound healing, Journal of Investigative Dermatology 127(5) (2007) 998-1008.
[119] H.N. Lovvorn Iii, D.T. Cheung, M.E. Nimni, N. Perelman, J.M. Estes, N.S. Adzick, Relative distribution and crosslinking of collagen distinguish fetal from adult sheep wound repair, Journal of pediatric surgery 34(1) (1999) 218-223.
[120] S. Levenson, E. Geever, L. Crowley, J. Oates III, C. Berard, H. Rosen, Healing of rat skin wounds, Annals of surgery 161(2) (1965) 293.
[121] S. Schreml, R.-M. Szeimies, L. Prantl, M. Landthaler, P. Babilas, Wound healing in the 21st century, Journal of the American Academy of Dermatology 63(5) (2010) 866-881.
[122] M.B. Dreifke, A.A. Jayasuriya, A.C. Jayasuriya, Current wound healing procedures and potential care, Materials Science and Engineering: C 48 (2015) 651-662.
[123] K. Vowden, P. Vowden, Understanding exudate management and the role of exudate in the healing process, British journal of community nursing (2003).
[124] R.F. Diegelmann, M.C. Evans, Wound healing: an overview of acute, fibrotic and delayed healing, Front Biosci 9(1) (2004) 283-289.
[125] I. Negut, V. Grumezescu, A. Grumezescu, Treatment Strategies for Infected Wounds, Molecules 23(9) (2018) 2392.
[126] C.J. de Haas, K.E. Veldkamp, A. Peschel, F. Weerkamp, W.J. Van Wamel, E.C. Heezius, M.J. Poppelier, K.P. Van Kessel, J.A. van Strijp, Chemotaxis inhibitory protein of Staphylococcus aureus, a bacterial antiinflammatory agent, Journal of Experimental Medicine 199(5) (2004) 687-695.
[127] B. Postma, M.J. Poppelier, J.C. Van Galen, E.R. Prossnitz, J.A. Van Strijp, C.J. De Haas, K.P. Van Kessel, Chemotaxis inhibitory protein of Staphylococcus aureus binds specifically to the C5a and formylated peptide receptor, The Journal of Immunology 172(11) (2004) 6994-7001.
[128] B. Diener, L. Carrick, R.S. Berk, In vivo studies with collagenase from Pseudomonas aeruginosa, Infection and immunity 7(2) (1973) 212-217.
[129] A.D. Olivas, B.D. Shogan, V. Valuckaite, A. Zaborin, N. Belogortseva, M. Musch, F. Meyer, W.L. Trimble, G. An, J. Gilbert, Intestinal tissues induce an SNP mutation in Pseudomonas aeruginosa that enhances its virulence: possible role in anastomotic leak, PloS one 7(8) (2012) e44326.
[130] C. Schaudinn, C. Dittmann, J. Jurisch, M. Laue, N. Günday-Türeli, U. Blume-Peytavi, A. Vogt, F. Rancan, Development, standardization and testing of a bacterial wound infection model based on ex vivo human skin, PloS one 12(11) (2017) e0186946.
[131] S.L. Percival, S.M. McCarty, B. Lipsky, Biofilms and wounds: an overview of the evidence, Advances in wound care 4(7) (2015) 373-381.
[132] J.F. Guest, N. Ayoub, T. McIlwraith, I. Uchegbu, A. Gerrish, D. Weidlich, K. Vowden, P. Vowden, Health economic burden that different wound types impose on the UK's National Health Service, International wound journal 14(2) (2017) 322-330.

[133] R.G. Sibbald, J.A. Elliott, L. Verma, A. Brandon, R. Persaud, E.A. Ayello, Update: Topical Antimicrobial Agents for Chronic Wounds, Advances in skin & wound care 30(10) (2017) 438-450.
[134] T. Fabo, A. Svensby, Transparent film dressing, Google Patents, 2008.
[135] P. Appelbaum, P. Hunter, The fluoroquinolone antibacterials: past, present and future perspectives, International journal of antimicrobial agents 16(1) (2000) 5-15.
[136] R. Davis, A. Markham, J.A. Balfour, Ciprofloxacin, Drugs 51(6) (1996) 1019-1074.
[137] K. Drlica, X. Zhao, DNA gyrase, topoisomerase IV, and the 4-quinolones, Microbiology and Molecular Biology Reviews 61(3) (1997) 377-92.
[138] D.C. Hooper, Mechanisms of Action of Antimicrobials: Focus on Fluoroquinolones, Clinical Infectious Diseases 32(Supplement 1) (2001) S9-S15.
[139] D.L. Ross, C.M. Riley, Aqueous solubilities of some variously substituted quinolone antimicrobials, International Journal of Pharmaceutics 63(3) (1990) 237-250.
[140] L. Mafra, S.r.M. Santos, R.e. Siegel, I.s. Alves, F.A. Almeida Paz, D. Dudenko, H.W. Spiess, Packing interactions in hydrated and anhydrous forms of the antibiotic ciprofloxacin: A solid-state NMR, X-ray diffraction, and computer simulation study, Journal of the American Chemical Society 134(1) (2011) 71-74.
[141] S. Mahapatra, K.N. Venugopala, T.N. Guru Row, A Device to Crystallize Organic Solids: Structure of Ciprofloxacin, Midazolam, and Ofloxacin as Targets, Crystal Growth & Design 10(4) (2010) 1866-1870.
[142] X. Li, Y. Hu, Y. Gao, G. Zhang, R. Henry, A methanol hemisolvate of ciprofloxacin, Acta Crystallographica Section E: Structure Reports Online 62(12) (2006) o5803-o5805.
[143] I. Aranaz, M.C. Gutierrez, L. Yuste, F. Rojo, M.L. Ferrer, F. del Monte, Controlled formation of the anhydrous polymorph of ciprofloxacin crystals embedded within chitosan scaffolds: study of the kinetic release dependence on crystal size, Journal of Materials Chemistry 19(11) (2009) 1576-1582.
[144] A.O. Surov, A.N. Manin, A.P. Voronin, K.V. Drozd, A.A. Simagina, A.V. Churakov, G.L. Perlovich, Pharmaceutical salts of ciprofloxacin with dicarboxylic acids, European Journal of Pharmaceutical Sciences 77 (2015) 112-121.
[145] I. Turel, P. Bukovec, M. Quirós, Crystal structure of ciprofloxacin hexahydrate and its characterization, International Journal of Pharmaceutics 152(1) (1997) 59-65.
[146] I. Turel, A. Golobic, Crystal structure of ciprofloxacin hydrochloride 1.34-hydrate, Analytical sciences : the international journal of the Japan Society for Analytical Chemistry 19(2) (2003) 329-30.
[147] M.A. Fonder, G.S. Lazarus, D.A. Cowan, B. Aronson-Cook, A.R. Kohli, A.J. Mamelak, Treating the chronic wound: a practical approach to the care of nonhealing wounds and wound care dressings, Journal of the American Academy of Dermatology 58(2) (2008) 185-206.
[148] C. Weller, G. Sussman, Wound dressings update, Journal of pharmacy practice and research 36(4) (2006) 318-324.
[149] H. Ryssel, O. Kloeters, G. Germann, T. Schäfer, G. Wiedemann, M. Oehlbauer, The antimicrobial effect of acetic acid—an alternative to common local antiseptics?, Burns 35(5) (2009) 695-700.
[150] J. Sloss, N. Cumberland, S. Milner, Acetic acid used for the elimination of Pseudomonas aeruginosa from burn and soft tissue wounds, Journal of the Royal Army Medical Corps 139(2) (1993) 49-51.
[151] I.N. Hirshfield, S. Terzulli, C. O'Byrne, Weak organic acids: a panoply of effects on bacteria, Science progress 86(4) (2003) 245-269.
[152] A. Walter, J. Gutknecht, Monocarboxylic acid permeation through lipid bilayer membranes, The Journal of membrane biology 77(3) (1984) 255-264.

[153] F.D. Halstead, M. Rauf, N.S. Moiemen, A. Bamford, C.M. Wearn, A.P. Fraise, P.A. Lund, B.A. Oppenheim, M.A. Webber, The Antibacterial Activity of Acetic Acid against Biofilm-Producing Pathogens of Relevance to Burns Patients, PloS one 10(9) (2015) e0136190.
[154] A. McManus, A. Mason Jr, W. McManus, B. Pruitt Jr, Twenty-five year review ofPseudomonas aeruginosa bacteremia in a burn center, European journal of clinical microbiology 4(2) (1985) 219-223.
[155] T. Akasaka, M. Tanaka, A. Yamaguchi, K. Sato, Type II topoisomerase mutations in fluoroquinolone-resistant clinical strains of Pseudomonas aeruginosa isolated in 1998 and 1999: role of target enzyme in mechanism of fluoroquinolone resistance, Antimicrobial agents and chemotherapy 45(8) (2001) 2263-2268.
[156] S. Jalal, O. Ciofu, N. Høiby, N. Gotoh, B. Wretlind, Molecular mechanisms of fluoroquinolone resistance in Pseudomonas aeruginosa isolates from cystic fibrosis patients, Antimicrobial Agents and Chemotherapy 44(3) (2000) 710-712.
[157] P.S. Wu, G. Otting, Rapid pulse length determination in high-resolution NMR, Journal of Magnetic Resonance 176(1) (2005) 115-119.
[158] R. Spanò, A. Muraglia, M.R. Todeschi, M. Nardini, P. Strada, R. Cancedda, M. Mastrogiacomo, Platelet Rich Plasma-based Bioactive Membrane as a New Advanced Wound Care Tool, Journal of Tissue Engineering and Regenerative Medicine (2016).
[159] F. Babaeijandaghi, I. Shabani, E. Seyedjafari, Z.S. Naraghi, M. Vasei, V. Haddadi-Asl, K.K. Hesari, M. Soleimani, Accelerated epidermal regeneration and improved dermal reconstruction achieved by polyethersulfone nanofibers, Tissue Engineering Part A 16(11) (2010) 3527-3536.
[160] R. Seoudi, A. Fouda, D. Elmenshawy, Synthesis, characterization and vibrational spectroscopic studies of different particle size of gold nanoparticle capped with polyvinylpyrrolidone, Physica B: Condensed Matter 405(3) (2010) 906-911.
[161] Q. Xu, B. Han, H. Yan, Equilibrium constant and enthalpy for the hydrogen bonding of acetic acid with tetrahydrofuran in supercritical CO2, The Journal of Physical Chemistry A 103(27) (1999) 5240-5245.
[162] L.J. Bellamy, The Infrared Spectra of Complex Molecules, 2 ed., Springer, London, 1980.
[163] G. Wider, L. Dreier, Measuring protein concentrations by NMR spectroscopy, Journal of the American Chemical Society 128(8) (2006) 2571-2576.
[164] L. Goldoni, T. Beringhelli, W. Rocchia, N. Realini, D. Piomelli, A simple and accurate protocol for absolute polar metabolite quantification in cell cultures using quantitative nuclear magnetic resonance, Analytical biochemistry 501 (2016) 26-34.
[165] Y.E. Kirsh, N. Yanul, K. Kalninsh, Structural transformations and water associate interactions in poly-N-vinylcaprolactam–water system, European polymer journal 35(2) (1999) 305-316.
[166] J.-Y. Le Questel, C. Laurence, A. Lachkar, M. Helbert, M. Berthelot, Hydrogen-bond basicity of secondary and tertiary amides, carbamates, ureas and lactams, Journal of the Chemical Society, Perkin Transactions 2 (12) (1992) 2091-2094.
[167] J. Ma, M. Yang, F. Yu, J. Zheng, Water-enhanced removal of ciprofloxacin from water by porous graphene hydrogel, Scientific reports 5 (2015).
[168] S. Bhattacharya, D.K. Sharma, S. Saurabh, S. De, A. Sain, A. Nandi, A. Chowdhury, Plasticization of poly (vinylpyrrolidone) thin films under ambient humidity: Insight from single-molecule tracer diffusion dynamics, The Journal of Physical Chemistry B 117(25) (2013) 7771-7782.
[169] J. Siepmann, N. Peppas, Modeling of drug release from delivery systems based on hydroxypropyl methylcellulose (HPMC), Advanced drug delivery reviews 48(2) (2001) 139-157.
[170] T.A. Gaidenko, C.W. Price, General stress transcription factor ςB and sporulation transcription factor ςH each contribute to survival of Bacillus subtilis under extreme growth conditions, Journal of bacteriology 180(14) (1998) 3730-3733.

[171] I. Romano, F. Ayadi, L. Rizzello, M. Summa, R. Bertorelli, P.P. Pompa, F. Brandi, I.S. Bayer, A. Athanassiou, Controlled antiseptic/eosin release from chitosan-based hydrogel modified fibrous substrates, Carbohydrate polymers 131 (2015) 306-314.
[172] J. Patterson, M.M. Martino, J.A. Hubbell, Biomimetic materials in tissue engineering, Materials today 13(1) (2010) 14-22.
[173] K.J. Rambhia, P.X. Ma, Controlled drug release for tissue engineering, Journal of Controlled Release 219 (2015) 119-128.
[174] Q. Wang, Z. Dong, Y. Du, J.F. Kennedy, Controlled release of ciprofloxacin hydrochloride from chitosan/polyethylene glycol blend films, Carbohydrate polymers 69(2) (2007) 336-343.
[175] Q. Xu, H. Liu, Z. Ye, K. Nan, S. Lin, H. Chen, B. Wang, Antimicrobial efficiency of PAA/(PVP/CHI) erodible polysaccharide multilayer through loading and controlled release of antibiotics, Carbohydrate Polymers 161 (2017) 53-62.
[176] J.J. Richardson, M. Björnmalm, F. Caruso, Technology-driven layer-by-layer assembly of nanofilms, Science 348(6233) (2015) aaa2491.
[177] C. Vilela, A.R. Figueiredo, A.J. Silvestre, C.S. Freire, Multilayered materials based on biopolymers as drug delivery systems, Expert opinion on drug delivery 14(2) (2017) 189-200.
[178] I. Yannas, J.F. Burke, Design of an artificial skin. I. Basic design principles, Journal of Biomedical Materials Research Part A 14(1) (1980) 65-81.
[179] I. Yannas, J. Burke, P. Gordon, C. Huang, R. Rubenstein, Design of an artificial skin. II. Control of chemical composition, Journal of Biomedical Materials Research Part A 14(2) (1980) 107-132.
[180] N. Dagalakis, J. Flink, P. Stasikelis, J. Burke, I. Yannas, Design of an artificial skin. Part III. Control of pore structure, Journal of Biomedical Materials Research Part A 14(4) (1980) 511-528.
[181] F.L. Mi, Y.B. Wu, S.S. Shyu, J.Y. Schoung, Y.B. Huang, Y.H. Tsai, J.Y. Hao, Control of wound infections using a bilayer chitosan wound dressing with sustainable antibiotic delivery, Journal of Biomedical Materials Research Part A 59(3) (2002) 438-449.
[182] F. Reyes-Ortega, A. Cifuentes, G. Rodríguez, M.R. Aguilar, Á. González-Gómez, R. Solis, N. García-Honduvilla, J. Buján, J. García-Sanmartin, A. Martínez, Bioactive bilayered dressing for compromised epidermal tissue regeneration with sequential activity of complementary agents, Acta biomaterialia 23 (2015) 103-115.
[183] H.-E. Thu, S.-F. Ng, Gelatine enhances drug dispersion in alginate bilayer film via the formation of crystalline microaggregates, International journal of pharmaceutics 454(1) (2013) 99-106.
[184] H.-E. Thu, M.H. Zulfakar, S.-F. Ng, Alginate based bilayer hydrocolloid films as potential slow-release modern wound dressing, International journal of pharmaceutics 434(1) (2012) 375-383.
[185] M. Zilberman, D. Egozi, M. Shemesh, A. Keren, E. Mazor, M. Baranes-Zeevi, N. Goldstein, I. Berdicevsky, A. Gilhar, Y. Ullmann, Hybrid wound dressings with controlled release of antibiotics: Structure-release profile effects and in vivo study in a guinea pig burn model, Acta biomaterialia 22 (2015) 155-163.
[186] D. Metcalf, D. Parsons, P. Bowler, A next-generation antimicrobial wound dressing: a real-life clinical evaluation in the UK and Ireland, Journal of wound care 25(3) (2016) 132, 134-8.
[187] R.W. Care, A study of biofilm-based wound management in subjects with critical limb ischaemia, Journal of wound care 17(4) (2008) 145.
[188] K. Bertin, T. Odehouri-Koudou, M. Sounkere, J. Yaokreh, S. Tembely, K. Yapo, Techniques and results of the conservative treatment of giant omphalocele with 2% disodium aqueous eosin, Clin Mother Child Health 11 (2013) 1.
[189] W. Who, M. Policy, Model List of Essential Medicines, 2011.

[190] M. Summa, D. Russo, I. Penna, N. Margaroli, I.S. Bayer, T. Bandiera, A. Athanassiou, R. Bertorelli, A biocompatible sodium alginate/povidone iodine film enhances wound healing, European Journal of Pharmaceutics and Biopharmaceutics 122 (2018) 17-24.
[191] P. Picone, L.A. Ditta, M.A. Sabatino, V. Militello, P.L. San Biagio, M.L. Di Giacinto, L. Cristaldi, D. Nuzzo, C. Dispenza, D. Giacomazza, Ionizing radiation-engineered nanogels as insulin nanocarriers for the development of a new strategy for the treatment of Alzheimer's disease, Biomaterials 80 (2016) 179-194.
[192] P. Picone, M.A. Sabatino, A. Ajovalasit, D. Giacomazza, C. Dispenza, M. Di Carlo, Biocompatibility, hemocompatibility and antimicrobial properties of xyloglucan-based hydrogel film for wound healing application, International journal of biological macromolecules 121 (2019) 784-795.
[193] CLSI, Perfomance Standards for Antimicrobial Disk Susceptibility Tests, Wayne, PA: Clinical and Laboratory Standards Institute, 2009.
[194] CLSI, Methods for Determining Bactericidal Activity of Antimicrobial Agents, Wayne, PA: Clinical Laboratory Standards Institute, 1999.
[195] F. Silva, O. Lourenço, J.A. Queiroz, F.C. Domingues, Bacteriostatic versus bactericidal activity of ciprofloxacin in Escherichia coli assessed by flow cytometry using a novel far-red dye, The Journal of antibiotics 64(4) (2011) 321.
[196] L. Macri, D. Silverstein, R.A. Clark, Growth factor binding to the pericellular matrix and its importance in tissue engineering, Advanced drug delivery reviews 59(13) (2007) 1366-1381.
[197] X. Xu, A.K. Jha, D.A. Harrington, M.C. Farach-Carson, X. Jia, Hyaluronic acid-based hydrogels: from a natural polysaccharide to complex networks, Soft matter 8(12) (2012) 3280-3294.
[198] G.M. Campo, A. Avenoso, S. Campo, A. D'Ascola, P. Traina, A. Calatroni, Differential effect of molecular size HA in mouse chondrocytes stimulated with PMA, Biochimica et Biophysica Acta (BBA)-General Subjects 1790(10) (2009) 1353-1367.
[199] G.M. Campo, A. Avenoso, S. Campo, A. D'Ascola, G. Nastasi, A. Calatroni, Molecular size hyaluronan differently modulates toll-like receptor-4 in LPS-induced inflammation in mouse chondrocytes, Biochimie 92(2) (2010) 204-215.
[200] G.M. Campo, A. Avenoso, S. Campo, P. Traina, A. D'Ascola, A. Calatroni, Glycosaminoglycans reduced inflammatory response by modulating toll-like receptor-4 in LPS-stimulated chondrocytes, Archives of biochemistry and biophysics 491(1) (2009) 7-15.
[201] G.M. Campo, A. Avenoso, G. Nastasi, A. Micali, V. Prestipino, M. Vaccaro, A. D'Ascola, A. Calatroni, S. Campo, Hyaluronan reduces inflammation in experimental arthritis by modulating TLR-2 and TLR-4 cartilage expression, Biochimica et Biophysica Acta (BBA)-Molecular Basis of Disease 1812(9) (2011) 1170-1181.
[202] K. Ghazi, U. Deng-Pichon, J.-M. Warnet, P. Rat, Hyaluronan fragments improve wound healing on in vitro cutaneous model through P2X7 purinoreceptor basal activation: role of molecular weight, PloS one 7(11) (2012) e48351.
[203] M. Contardi, J.A. Heredia-Guerrero, G. Perotto, P. Valentini, P.P. Pompa, R. Spanò, L. Goldoni, R. Bertorelli, A. Athanassiou, I.S. Bayer, Transparent ciprofloxacin-povidone antibiotic films and nanofiber mats as potential skin and wound care dressings, European Journal of Pharmaceutical Sciences 104 (2017) 133-144.
[204] A.M. Asiri, M.S. Al-Amoudi, S.A. Bazaid, A.A. Adam, K.A. Alamry, S. Anandan, Enhanced visible light photodegradation of water pollutants over N-, S-doped titanium dioxide and n-titanium dioxide in the presence of inorganic anions, Journal of Saudi Chemical Society 18(2) (2014) 155-163.
[205] K. Haxaire, Y. Marechal, M. Milas, M. Rinaudo, Hydration of polysaccharide hyaluronan observed by IR spectrometry. I. Preliminary experiments and band assignments, Biopolymers 72(1) (2003) 10-20.

[206] A. Karwoski, R. Plaut, Experiments on peeling adhesive tapes from human forearms, Skin Research and Technology 10(4) (2004) 271-277.
[207] D. Maillard-Salin, P. Bécourt, G. Couarraze, Physical evaluation of a new patch made of a progestomimetic in a silicone matrix, International journal of pharmaceutics 199(1) (2000) 29-38.
[208] A. Nussinovitch, A. Gal, C. Padula, P. Santi, Physical characterization of a new skin bioadhesive film, AAPS PharmSciTech 9(2) (2008) 458-463.
[209] A. Gal, A. Nussinovitch, Plasticizers in the manufacture of novel skin-bioadhesive patches, International journal of pharmaceutics 370(1-2) (2009) 103-109.
[210] S. Diridollou, F. Patat, F. Gens, L. Vaillant, D. Black, J. Lagarde, Y. Gall, M. Berson, In vivo model of the mechanical properties of the human skin under suction, Skin Research and technology 6(4) (2000) 214-221.
[211] H.U. Zaman, J. Islam, M.A. Khan, R.A. Khan, Physico-mechanical properties of wound dressing material and its biomedical application, Journal of the mechanical behavior of biomedical materials 4(7) (2011) 1369-1375.
[212] W.-C. Lin, C.-C. Lien, H.-J. Yeh, C.-M. Yu, S.-h. Hsu, Bacterial cellulose and bacterial cellulose–chitosan membranes for wound dressing applications, Carbohydrate polymers 94(1) (2013) 603-611.
[213] R. Gupta, B. Mukherjee, Development and in vitro evaluation of diltiazem hydrochloride transdermal patches based on povidone–ethylcellulose matrices, Drug development and industrial pharmacy 29(1) (2003) 1-7.
[214] Y.S. Choi, S. Lee, S.R. Hong, Y. Lee, K. Song, M. Park, Studies on gelatin-based sponges. Part III: a comparative study of cross-linked gelatin/alginate, gelatin/hyaluronate and chitosan/hyaluronate sponges and their application as a wound dressing in full-thickness skin defect of rat, Journal of Materials Science: Materials in Medicine 12(1) (2001) 67-73.
[215] S. Rossi, M. Marciello, G. Sandri, F. Ferrari, M.C. Bonferoni, A. Papetti, C. Caramella, C. Dacarro, P. Grisoli, Wound dressings based on chitosans and hyaluronic acid for the release of chlorhexidine diacetate in skin ulcer therapy, Pharmaceutical development and technology 12(4) (2007) 415-422.
[216] G. Pawelec, Age and immunity: What is "immunosenescence"?, Experimental gerontology (2017).
[217] M. Malone, T. Bjarnsholt, A.J. McBain, G.A. James, P. Stoodley, D. Leaper, M. Tachi, G. Schultz, T. Swanson, R.D. Wolcott, The prevalence of biofilms in chronic wounds: a systematic review and meta-analysis of published data, Journal of wound care 26(1) (2017) 20-25.
[218] S.L. Percival, K.E. Hill, D.W. Williams, S.J. Hooper, D.W. Thomas, J.W. Costerton, A review of the scientific evidence for biofilms in wounds, Wound repair and regeneration 20(5) (2012) 647-657.
[219] P. Szweda, G. Gorczyca, R. Tylingo, Comparison of antimicrobial activity of selected, commercially available wound dressing materials, Journal of wound care 27(5) (2018) 320-326.
[220] G.E. Flaten, Z. Palac, A. Engesland, J. Filipović-Grčić, Ž. Vanić, N. Škalko-Basnet, In vitro skin models as a tool in optimization of drug formulation, European Journal of Pharmaceutical Sciences 75 (2015) 10-24.
[221] G. Maboni, R. Davenport, K. Sessford, K. Baiker, T.K. Jensen, A.M. Blanchard, S. Wattegedera, G. Entrican, S. Tötemeyer, A novel 3D skin explant model to study anaerobic bacterial infection, Frontiers in cellular and infection microbiology 7 (2017) 404.
[222] L. Steinstraesser, M. Sorkin, A. Niederbichler, M. Becerikli, J. Stupka, A. Daigeler, M. Kesting, I. Stricker, F. Jacobsen, M. Schulte, A novel human skin chamber model to study wound infection ex vivo, Archives of dermatological research 302(5) (2010) 357-365.

[223] P.L. Phillips, Q. Yang, S. Davis, E.M. Sampson, J.I. Azeke, A. Hamad, G.S. Schultz, Antimicrobial dressing efficacy against mature Pseudomonas aeruginosa biofilm on porcine skin explants, International wound journal 12(4) (2015) 469-483.
[224] Q. Yang, C. Larose, A.C. Della Porta, G.S. Schultz, D.J. Gibson, A surfactant-based wound dressing can reduce bacterial biofilms in a porcine skin explant model, International wound journal 14(2) (2017) 408-413.
[225] H.A. Ramirez, I. Pastar, I. Jozic, O. Stojadinovic, R.C. Stone, N. Ojeh, J. Gil, S.C. Davis, R.S. Kirsner, M. Tomic-Canic, Staphylococcus aureus Triggers Induction of miR-15B-5P to Diminish DNA Repair and Deregulate Inflammatory Response in Diabetic Foot Ulcers, Journal of Investigative Dermatology 138(5) (2018) 1187-1196.
[226] M.E. Skindersoe, M. Alhede, R. Phipps, L. Yang, P.O. Jensen, T.B. Rasmussen, T. Bjarnsholt, T. Tolker-Nielsen, N. Høiby, M. Givskov, Effects of antibiotics on quorum sensing in Pseudomonas aeruginosa, Antimicrobial agents and chemotherapy 52(10) (2008) 3648-3663.
[227] H.A. Ravin, A.M. Seligman, J. Fine, Polyvinyl pyrrolidone as a plasma expander: Studies on its excretion, distribution and metabolism, New England Journal of Medicine 247(24) (1952) 921-929.
[228] A. Gürbay, C. Garrel, M. Osman, M. Richard, A. Favier, F. Hincal, Cytotoxicity in ciprofloxacin-treated human fibroblast cells and protection by vitamin E, Human & experimental toxicology 21(12) (2002) 635-641.
[229] F. Kautzky, A. Hartinger, L.D. Köhler, H.J. Vogt, In vitro cytotoxicity of antimicrobial agents to human keratinocytes, Journal of the European Academy of Dermatology and Venereology 6(2) (1996) 159-166.
[230] J. Marchant, When antibiotics turn toxic, Nature 555(7697) (2018) 431-433.
[231] A. Schmidtchen, E. Holst, H. Tapper, L. Björck, Elastase-producing Pseudomonas aeruginosa degrade plasma proteins and extracellular products of human skin and fibroblasts, and inhibit fibroblast growth, Microbial pathogenesis 34(1) (2003) 47-55.
[232] M. Werthen, M. Davoudi, A. Sonesson, D. Nitsche, M. Mörgelin, K. Blom, A. Schmidtchen, Pseudomonas aeruginosa-induced infection and degradation of human wound fluid and skin proteins ex vivo are eradicated by a synthetic cationic polymer, Journal of Antimicrobial Chemotherapy 54(4) (2004) 772-779.
[233] A. Vieira, Y. Silva, A. Cunha, N. Gomes, H.-W. Ackermann, A. Almeida, Phage therapy to control multidrug-resistant Pseudomonas aeruginosa skin infections: in vitro and ex vivo experiments, European journal of clinical microbiology & infectious diseases 31(11) (2012) 3241-3249.
[234] C. Björn, M. Mahlapuu, I. Mattsby-Baltzer, J. Håkansson, Anti-infective efficacy of the lactoferrin-derived antimicrobial peptide HLR1r, Peptides 81 (2016) 21-28.
[235] D.C. Roy, S. Tomblyn, D.M. Burmeister, N.L. Wrice, S.C. Becerra, L.R. Burnett, J.M. Saul, R.J. Christy, Ciprofloxacin-loaded keratin hydrogels prevent Pseudomonas aeruginosa infection and support healing in a porcine full-thickness excisional wound, Advances in wound care 4(8) (2015) 457-468.
[236] D.A. Dias, S. Urban, U. Roessner, A historical overview of natural products in drug discovery, Metabolites 2(2) (2012) 303-336.
[237] I. Liakos, L. Rizzello, H. Hajiali, V. Brunetti, R. Carzino, P. Pompa, A. Athanassiou, E. Mele, Fibrous wound dressings encapsulating essential oils as natural antimicrobial agents, Journal of Materials Chemistry B 3(8) (2015) 1583-1589.
[238] I. Liakos, L. Rizzello, D.J. Scurr, P.P. Pompa, I.S. Bayer, A. Athanassiou, All-natural composite wound dressing films of essential oils encapsulated in sodium alginate with antimicrobial properties, International journal of pharmaceutics 463(2) (2014) 137-145.

[239] R. Silva-Carvalho, F. Baltazar, C. Almeida-Aguiar, Propolis: a complex natural product with a plethora of biological activities that can be explored for drug development, Evidence-Based Complementary and Alternative Medicine 2015 (2015).
[240] C. Manach, A. Scalbert, C. Morand, C. Rémésy, L. Jiménez, Polyphenols: food sources and bioavailability, The American journal of clinical nutrition 79(5) (2004) 727-747.
[241] T.F. Bachiega, C.L. Orsatti, A.C. Pagliarone, J.M. Sforcin, The effects of propolis and its isolated compounds on cytokine production by murine macrophages, Phytotherapy Research 26(9) (2012) 1308-1313.
[242] J.S. Jurenka, Anti-inflammatory properties of curcumin, a major constituent of Curcuma longa: a review of preclinical and clinical research, Alternative medicine review 14(2) (2009).
[243] B. Janicke, C. Hegardt, M. Krogh, G. Önning, B. Åkesson, H.M. Cirenajwis, S.M. Oredsson, The antiproliferative effect of dietary fiber phenolic compounds ferulic acid and p-coumaric acid on the cell cycle of Caco-2 cells, Nutrition and cancer 63(4) (2011) 611-622.
[244] N.N. Bouzaiene, S.K. Jaziri, H. Kovacic, L. Chekir-Ghedira, K. Ghedira, J. Luis, The effects of caffeic, coumaric and ferulic acids on proliferation, superoxide production, adhesion and migration of human tumor cells in vitro, European journal of pharmacology 766 (2015) 99-105.
[245] B.B. Aggarwal, A. Kumar, A.C. Bharti, Anticancer potential of curcumin: preclinical and clinical studies, Anticancer research 23(1/A) (2003) 363-398.
[246] R.A. Chmielowski, D.S. Abdelhamid, J.J. Faig, L.K. Petersen, C.R. Gardner, K.E. Uhrich, L.B. Joseph, P.V. Moghe, Athero-inflammatory nanotherapeutics: Ferulic acid-based poly (anhydride-ester) nanoparticles attenuate foam cell formation by regulating macrophage lipogenesis and reactive oxygen species generation, Acta biomaterialia 57 (2017) 85-94.
[247] C.-M. Lin, J.-H. Chiu, I.-H. Wu, B.-W. Wang, C.-M. Pan, Y.-H. Chen, Ferulic acid augments angiogenesis via VEGF, PDGF and HIF-1α, The Journal of nutritional biochemistry 21(7) (2010) 627-633.
[248] C. Morgan, Y. Nigam, Naturally derived factors and their role in the promotion of angiogenesis for the healing of chronic wounds, Angiogenesis 16(3) (2013) 493-502.
[249] M.R. Ahn, K. Kunimasa, S. Kumazawa, T. Nakayama, K. Kaji, Y. Uto, H. Hori, H. Nagasawa, T. Ohta, Correlation between antiangiogenic activity and antioxidant activity of various components from propolis, Molecular nutrition & food research 53(5) (2009) 643-651.
[250] P. Picone, M.L. Bondi, P. Picone, M.L. Bondi, G. Montana, A. Bruno, G. Pitarresi, G. Giammona, M. Di Carlo, Ferulic acid inhibits oxidative stress and cell death induced by Ab oligomers: improved delivery by solid lipid nanoparticles, Free radical research 43(11) (2009) 1133-1145.
[251] A. Battisti, A.P. Piccionello, A. Sgarbossa, S. Vilasi, C. Ricci, F. Ghetti, F. Spinozzi, A.M. Gammazza, V. Giacalone, A. Martorana, Curcumin-like compounds designed to modify amyloid beta peptide aggregation patterns, RSC Advances 7(50) (2017) 31714-31724.
[252] M. Abdel-Wahab, M.A. El-Mahdy, M.F. Abd-Ellah, G. Helal, F. Khalifa, F. Hamada, Influence of p-coumaric acid on doxorubicin-induced oxidative stress in rat's heart, Pharmacological Research 48(5) (2003) 461-465.
[253] L.R. Ferguson, S.t. Zhu, P.J. Harris, Antioxidant and antigenotoxic effects of plant cell wall hydroxycinnamic acids in cultured HT-29 cells, Molecular nutrition & food research 49(6) (2005) 585-593.
[254] Z. Lou, H. Wang, S. Rao, J. Sun, C. Ma, J. Li, p-Coumaric acid kills bacteria through dual damage mechanisms, Food Control 25(2) (2012) 550-554.
[255] G.S. Nyanhongo, C. Sygmund, R. Ludwig, E.N. Prasetyo, G.M. Guebitz, An antioxidant regenerating system for continuous quenching of free radicals in chronic wounds, European Journal of Pharmaceutics and Biopharmaceutics 83(3) (2013) 396-404.

[256] M.M. Ghaisas, S.B. Kshirsagar, R.S. Sahane, Evaluation of wound healing activity of ferulic acid in diabetic rats, International wound journal 11(5) (2014) 523-532.
[257] M. Lodovici, S. Caldini, L. Morbidelli, V. Akpan, M. Ziche, P. Dolara, Protective effect of 4-coumaric acid from UVB ray damage in the rabbit eye, Toxicology 255(1-2) (2009) 1-5.
[258] M. Lodovici, L. Raimondi, F. Guglielmi, S. Gemignani, P. Dolara, Protection against ultraviolet B-induced oxidative DNA damage in rabbit corneal-derived cells (SIRC) by 4-coumaric acid, Toxicology 184(2-3) (2003) 141-147.
[259] J.A. Nichols, S.K. Katiyar, Skin photoprotection by natural polyphenols: anti-inflammatory, antioxidant and DNA repair mechanisms, Archives of dermatological research 302(2) (2010) 71-83.
[260] M. Larrosa, M. Lodovici, L. Morbidelli, P. Dolara, Hydrocaffeic and p-coumaric acids, natural phenolic compounds, inhibit UV-B damage in WKD human conjunctival cells in vitro and rabbit eye in vivo, Free radical research 42(10) (2008) 903-910.
[261] F. Guglielmi, C. Luceri, L. Giovannelli, P. Dolara, M. Lodovici, Effect of 4-coumaric and 3, 4-dihydroxybenzoic acid on oxidative DNA damage in rat colonic mucosa, British Journal of Nutrition 89(5) (2003) 581-587.
[262] C.-T. Yeh, L.-C. Ching, G.-C. Yen, Inducing gene expression of cardiac antioxidant enzymes by dietary phenolic acids in rats, The Journal of nutritional biochemistry 20(3) (2009) 163-171.
[263] C.-T. Yeh, G.-C. Yen, Induction of hepatic antioxidant enzymes by phenolic acids in rats is accompanied by increased levels of multidrug resistance–associated protein 3 mRNA expression, The Journal of nutrition 136(1) (2006) 11-15.
[264] S.J. Vicente, E.Y. Ishimoto, E.A. Torres, Coffee modulates transcription factor Nrf2 and highly increases the activity of antioxidant enzymes in rats, Journal of agricultural and food chemistry 62(1) (2013) 116-122.
[265] S. Guzman-Puyol, D. Russo, I. Penna, L. Ceseracciu, F. Palazon, A. Scarpellini, R. Cingolani, R. Bertorelli, I.S. Bayer, J.A. Heredia-Guerrero, Facile production of seaweed-based biomaterials with antioxidant and anti-inflammatory activities, Algal Research 27 (2017) 1-11.
[266] M. Teodorescu, M. Bercea, Poly (vinylpyrrolidone)–a versatile polymer for biomedical and beyond medical applications, Polymer-Plastics Technology and Engineering 54(9) (2015) 923-943.
[267] H. Skaltsa, E. Verykokidou, C. Harvala, G. Karabourniotis, Y. Manetasi, UV-B protective potential and flavonoid content of leaf hairs of Quercus ilex, Phytochemistry 37(4) (1994) 987-990.
[268] V. Tantishaiyakul, N. Kaewnopparat, S. Ingkatawornwong, Properties of solid dispersions of piroxicam in polyvinylpyrrolidone, International Journal of Pharmaceutics 181(2) (1999) 143-151.
[269] N. Kumar, V. Pruthi, N. Goel, Structural, thermal and quantum chemical studies of p-coumaric and caffeic acids, Journal of Molecular Structure 1085 (2015) 242-248.
[270] R. Swislocka, M. Kowczyk-Sadowy, M. Kalinowska, W. Lewandowski, Spectroscopic (FT-IR, FT-Raman, 1H and 13C NMR) and theoretical studies of p-coumaric acid and alkali metal p-coumarates, Journal of Spectroscopy 27(1) (2012) 35-48.
[271] N. Bloembergen, E.M. Purcell, R.V. Pound, Relaxation effects in nuclear magnetic resonance absorption, Resonances, World Scientific1990, pp. 411-444.
[272] H.Y. Carr, E.M. Purcell, Effects of diffusion on free precession in nuclear magnetic resonance experiments, Physical review 94(3) (1954) 630.
[273] M. Sathish, G. Meenakshi, S. Xavier, S. Sebastian, Conformational Stability, TGA, and Molecular Docking Investigations of p-Coumaric Acid with Special Relevance to Anti-Cancer and Antibacterial Activity, Acta Physica Polonica, A. 131(6) (2017).
[274] Y. Du, P. Yang, Z. Mou, N. Hua, L. Jiang, Thermal decomposition behaviors of PVP coated on platinum nanoparticles, Journal of applied polymer science 99(1) (2006) 23-26.

[275] P. Mousavioun, W.O. Doherty, G. George, Thermal stability and miscibility of poly (hydroxybutyrate) and soda lignin blends, Industrial Crops and Products 32(3) (2010) 656-661.
[276] J. Zhu, D. Zhang, H. Tang, G. Zhao, Structure relationship of non–covalent interactions between phenolic acids and arabinan–rich pectic polysaccharides from rapeseed meal, International Journal of Biological Macromolecules (2018).
[277] A. Giacometti, O. Cirioni, A. Schimizzi, M. Del Prete, F. Barchiesi, M. D'errico, E. Petrelli, G. Scalise, Epidemiology and microbiology of surgical wound infections, Journal of clinical microbiology 38(2) (2000) 918-922.
[278] J. Reilly, S. Twaddle, J. McIntosh, L. Kean, An economic analysis of surgical wound infection, Journal of Hospital Infection 49(4) (2001) 245-249.
[279] N. Graves, Economics and preventing hospital-acquired infection, Emerging infectious diseases 10(4) (2004) 561.
[280] R. Visse, H. Nagase, Matrix metalloproteinases and tissue inhibitors of metalloproteinases: structure, function, and biochemistry, Circulation research 92(8) (2003) 827-839.
[281] D.G. Armstrong, E.B. Jude, The role of matrix metalloproteinases in wound healing, Journal of the American Podiatric Medical Association 92(1) (2002) 12-18.
[282] A.B. Wysocki, L. Staiano-Coico, F. Grinnell, Wound fluid from chronic leg ulcers contains elevated levels of metalloproteinases MMP-2 and MMP-9, Journal of Investigative Dermatology 101(1) (1993) 64-68.
[283] F. Sabino, U. Auf dem Keller, Matrix metalloproteinases in impaired wound healing, Metalloproteinases In Medicine 2 (2015) 1-8.
[284] M.J. Reiss, Y.-P. Han, E. Garcia, M. Goldberg, H. Yu, W.L. Garner, Matrix metalloproteinase-9 delays wound healing in a murine wound model, Surgery 147(2) (2010) 295-302.
[285] M.P. Caley, V.L. Martins, E.A. O'Toole, Metalloproteinases and wound healing, Advances in wound care 4(4) (2015) 225-234.